

Test measurements with an operational microstructure-turbulence profiler: Detection limit of dissipation rates

Hartmut Prandke^{1,*} and Adolf Stips²

¹ ME Meerestechnik-Elektronik GmbH, Iserstrasse 6, D-24610 Trappenkamp, Germany

² Joint Research Centre, European Commission, Space Applications Institute, Marine Environment, TP 272, I-21020 Ispra (Varese), Italy

Key words: Dissipation rate, detection limit, shear measurement, turbulence, mixing.

ABSTRACT

The MST (Microstructure-Turbulence) Profiler is a newly developed operational microstructure measuring system, specially designed for marine and limnic turbulence measurements. The profiler can be used for sinking and uprising measurements and is equipped with a new type of current shear sensor. We have tested the MST Profiler in several field measuring campaigns in deep Alpine lakes. The investigations were focused on the internal vibration level of the profiler and its lower detection limit for dissipation rate estimates (pseudo dissipation). The upper detection limit was estimated based on the geometry of the shear sensor. The test measurements gave no indication of pronounced internal profiler vibrations interfering with dissipation measurements. The pseudo dissipation level (noise) of the profiler was found to be as low as $5 \cdot 10^{-12}$ W/kg under quiet conditions at sinking velocities below 0.4 m/s. At 0.8 m/s sinking velocity, a pseudo dissipation of $4 \cdot 10^{-11}$ W/kg was obtained. At rising measurements with additional sources of profiler vibrations due to influence of the cable the pseudo dissipation is about twice that for sinking measurements. For the upper detection limit which can be measured without correction for unresolved variance of the shear spectrum, a value of 10^{-4} W/kg was estimated.

1 Introduction

Small scale turbulence causes vertical fluxes of mass and energy, of dissolved and suspended material in stratified waters. These fluxes directly influence larger scale physical, chemical, and biological processes in the aquatic environment. The dissipation rate of kinetic energy is a key parameter to quantify the level of turbulence and the resulting mixing processes in natural waters. Based on dissipation rate measurements, vertical diffusion coefficients and flux rates as well as friction velocities can be determined (Osborn, 1980, Dewey and Crawford, 1988).

* Present affiliation: ISW In Situ Wassermesstechnik, Lenzer Strasse 5, D-17213 Petersdorf, Germany.

Dissipation rates of turbulent kinetic energy in natural waters range from below 10^{-11} to about 10^{-4} W/kg. Only in extreme situations such as in strong tidal currents (Wesson and Gregg, 1994), can higher dissipation rates be obtained. At low levels of dissipation, shear measurement-based dissipation estimates can be problematic due to the noise caused by internal vibration of the profiling instrument. The profiler vibrations are detected by the shear probe and produce a “pseudo-dissipation” rate (profiler noise level). This pseudo-dissipation rate is the low end detection limit of the dissipation rate which can be measured by a microstructure profiler. The knowledge of the lower detection limit is important for the interpretation of dissipation measurements, especially in low turbulence regions like the ocean interior or enclosed basins and lakes. Moum and Lueck (1985) have analysed low dissipation measurements in the ocean. They showed, that the measured lowest dissipation level of about 10^{-10} W/kg was a reflection of the pseudo dissipation rate of their profiler. Measured dissipation rates near the detection limit may therefore not represent the natural level of kinetic energy dissipation, which may be much smaller.

The upper dissipation rate detection limit is set by the spatial resolution of the shear probe. With increasing dissipation level the cut-off wavenumber (Kolmogoroff wavenumber)

$$k_c = 1/(2\pi) \cdot (\varepsilon/\nu^3)^{1/4} \quad (1)$$

(ν is the kinematic viscosity of water, ε is the dissipation rate of turbulent kinetic energy) of the turbulence spectrum is shifted to higher values. At a dissipation rate of 10^{-4} W/kg (the upper level in natural waters under normal conditions) $k_c/2$ corresponds to about 185 cpm. Consequently, shear probes should have a spatial resolution of at least $2/k_c \cong 5$ mm to resolve this wavenumber range.

The wide range of dissipation rates requires special instrumentation and efforts in data evaluation to determine energy dissipation in water. Especially in the low and high dissipation range the resolution of known microstructure profiler and current shear sensors is not sufficient to resolve the natural range of dissipation in lakes and in the sea. Furthermore, a more extensive integration of microstructure and turbulence measurements in marine and limnic research requires microstructure profilers qualified for use by “non specialists” in microstructure investigations. The development of the MST Profiler* aimed into this direction. It is designed as a measuring system which can be easily handled by not specially trained personnel. The profiler is qualified to determine the dissipation rate covering as far as possible the range of turbulence occurring in natural waters.

The Space Applications Institute, Joint Research Centre of the European Commission, Ispra/Italy, uses the MST Profiler in several international marine and limnic research programmes. In preparation of these applications, the profiler has been tested in several field measuring campaigns in deep Alpine lakes. The investigations were focused on the internal vibration level of the probe and its lower detection limit for dissipation rate estimates. The upper detection limit was estimated based on the geometry of the shear sensor.

* The MST Profiler was developed in the framework of the international EUREKA project (EUOMAR-MICSOS, EU 1246) by ME Meerestechnik-Elektronik GmbH, Trappenkamp (Germany) in cooperation with Space Applications Institute, Joint Research Centre, Ispra (Italy).

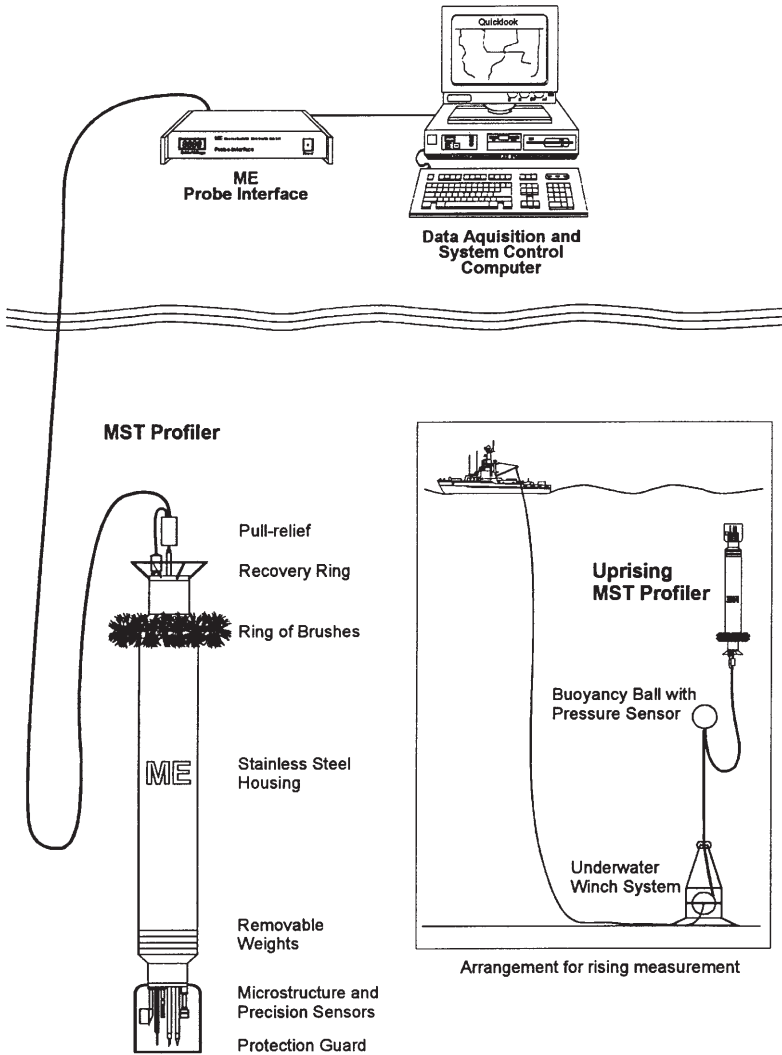


Figure 1. General system layout of the MST (Micro-Structure-Turbulence) Profiler. The measuring system is produced by Meerestechnik-Elektronik GmbH (ME). The profiler can be balanced for sinking as well as rising operations

2 Construction of MST Profiler

The construction of the MST Profiler is described by Prandke and Stips (1996) (referred later on as PS96). In this paper we give a brief description of the MST Profiler. For more details we refer to PS96.

In Fig. 1 the basic system configuration is shown. The MST Profiler is an instrument for simultaneous microstructure and precision measurements of physical

parameters in marine and limnic waters. It is designed for vertical profiling within the upper 100 m. The data are transmitted via electrical cable to an on board unit and further to a data acquisition PC. The profiler can be used for sinking operations, as well as for rising measurements. These two modes of operation allow coverage of the entire depth range from the surface down to the maximum operation depth.

The main housing of the profiler consists of a cylindrical stainless steel tube with a length of 700 mm and a diameter of 155 mm. Both ends of the central part have caps with a reduced diameter of 108 mm. This gives a total length of the housing of about 1000 mm. The housing is pressure tight to 1 MPa (~ 100 m). With additional stiffening rings inside the housing, its pressure resistance can be increased to several MPa. A ring of brushes is placed at the upper end of the probe (cable end) to give it drag and righting-torque. Adjusting weights can be fixed at both ends of the housing. This allows to give the profiler different buoyancy.

For vertical sinking measurements, the profiler is balanced with a slightly negative buoyancy which gives it a sinking velocity between about 0.4 and 0.75 m/s (recommended by the manufacturer of the profiler). The profiler is manually handled and recovered. Effects caused by cable tension (vibrations) and the ship's movement are excluded by a cable slack.

For rising measurements, the MST Profiler is given a positive buoyancy. It is operated via a remote controlled underwater winch. To guaranty free movement of the profiler, an additional buoyancy body near to the profiler carries the weight of the cable and produces a cable slack just below the rising instrument. Uprising measurements near the shore line or in narrow limnic waters have been carried out having the winch on land. In this case, a guide pulley was placed on the bottom at the investigation site.

The MST Profiler is equipped with microstructure sensors, standard CTD sensors for precision measurements, and a vibration control sensor (see Table 1). The sampling rate for all sensors is 1000 samples per second, the resolution 16 bit. The sensors are mounted at the lower end of the probe (sensor end, Fig. 1). The microstructure sensors are placed at the tip of a slim shaft, about 120 mm in front of the CTD sensors.

3 Shear measurements

For measurements of velocity microstructure, the MST Profiler is equipped with an airfoil shear probe PNS 93. The general behaviour and the construction principles of an airfoil sensor have been described in detail by Osborn and Crawford (1977 and 1980). The Osborn type of shear probe is an axially symmetric airfoil of revolution mounted at the end of a cylindrical shaft. The length and diameter of the airfoil are 9 mm and 4.8 mm, respectively. A slightly larger probe with a length of 13.5 mm and a diameter of 6 mm was designed by Oakey (1977). The mean velocity due to the profiling speed of the probe is aligned with the axis of revolution. While the probe is not sensitive to axial forces, the cross-stream (transverse) components of turbulent velocity produce a lifting force at the airfoil. A piezoceramic beam embedded within the airfoil made of rubber material senses the lift force. The output of the

Table 1. Sensor equipment of the MST Profiler (standard version)

Parameter	Principle	Sensing element	Length of sensor tip	Time constant	
<i>Microstructure sensors</i>					
Current shear	lift force measurement at airfoil nose	piezoceramic bending beam	3.5 mm	approx. 3 ms	
Temperature	resistance measurement	glass rod micro-thermistor FP 07	approx. 0.3 mm	approx. 10 ms	
Temperature (alternatively)	thermocouple voltage measurement	NiCr-Ni thermocouple inside a steel tube \varnothing 0.25 mm	approx. 0.5 mm	approx. 6 ms	
<i>Precision CTD sensors</i>					
Parameter	Principle	Range	Accuracy	Resolution	Time constant
Pressure	piezo-resistive	user-definable	+/- 0.1 % of full scale	0.002 % of full scale	40 ms
Temperature	Pt 100	- 2 ... + 38°C	+/- 0.01°C	0.001 °C	160 ms
Conductivity	7-Pole-cell	0 ... 60 mS/cm	+/- 0.01 mS/cm	0.001 mS/cm	100 ms
<i>Control sensor</i>					
Parameter	Principle	Sensing element	Time constant		
Horizontal profiler acceleration	lift force measurement at pendulum mass	piezoceramic bending beam	approx. 3 ms		

piezoceramic element is a voltage proportional to the instantaneous cross-stream component of the velocity field.

The PNS 93 shear probe is designed for a higher spatial resolution compared to that of the Osborn/Oakey shear probes (Prandke, 1994). Its principal function is the same as described above. However, the overall construction differs from that of the Osborn/Oakey probe. As shown in Figure 2, the airfoil and the piezoceramic beam are separated by a cantilever. At its free end the cantilever carries an axially symmetric airfoil. The length and diameter of the airfoil are only 3.5 mm and 3 mm, respectively. The piezoceramic beam senses the dynamic lifting force caused by one cross-stream component of the turbulent velocity field. The cantilever construction acts as a lever increasing the bending force at the position of the beam. The piezoceramic beam as well as the cantilever are protected by a cone-shaped metallic cap. Only the airfoil stands out from the cap. The narrow gap between cantilever and cap prevents damage to the beam by strong bending. During in situ operations, the interior of the cap is water filled. Side-holes at the upper end of the cap prevent air being trapped inside the cap. The output voltage of the piezoceramic beam is fed into two sequential circuits that amplify and high-pass the signal. The high-pass with a slope of 6 dB/octave (20 dB/decade) and a time

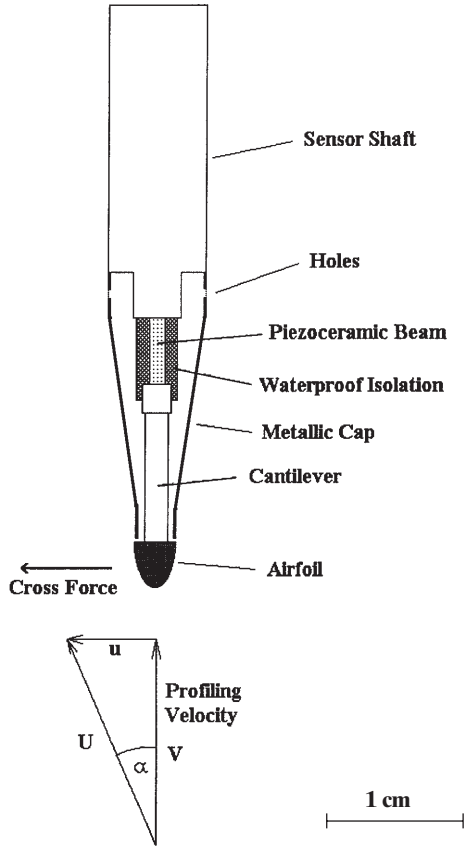


Figure 2. Construction and flow geometry of PNS 93 shear probe

constant of 1 s acts as a differentiator for the sensor signal. Finally, a 500 Hz low-pass acts as an anti-aliasing filter.

Following Allen and Perkins (1952), for an axially symmetric airfoil in an inviscid flow of speed U and an angle of attack α (see Fig. 2), the cross force f_p per unit length due to the potential flow can be expressed as

$$f_p = 1/2 \cdot \rho U^2 \cdot dA/dx \cdot \sin 2\alpha \tag{2}$$

ρ is the density of the fluid and dA/dx is the rate of change in the airfoil cross section area in axial direction. Investigations by Osborn and Crawford (1977) have shown, that this equation is valid for angles of attack up to about 10 degrees. At larger angles the theory slightly underestimates the forces. To get the total cross force F , equation (2) can be integrated along the axis from the tip to the position where dA/dx is 0:

$$F = 1/2 \cdot \rho U^2 A \cdot \sin 2\alpha \tag{3}$$

Using the double angle relation $\sin 2\alpha = 2\sin\alpha \cos\alpha$, equation (3) can be written as

$$F = \rho AVu \tag{4}$$

V is the axial component and u is the cross-stream component of the flow speed U , respectively. For the calibration of PNS 93 shear probes in the laboratory of ME Meerestechnik-Elektronik a well proven arrangement to carry out shear probe calibrations is used (see Osborn and Crawford, 1977 and Box, 1992). The probe rotates about its axis of symmetry at 1 Hz under an angle of attack α in a water jet of a velocity U . As the probe rotates in the jet, the total cross-force on the probe remains constant but the force on the piezoceramic beam varies sinusoidally. At a constant jet velocity U , the rms voltage output of the probe E_{rms} is measured at different angles of attack between 0 and 10 degree. The probe sensitivity S is the slope of the regression (best fit of a cubic approximation) of $E_{rms}/(\rho U^2)$ versus $\sin 2\alpha$ at $\alpha = 0$ degree.

An individual calibration procedure give a probe sensitivity with an accuracy of about 10%. Calibrations of a PNS 93 shear probe at 4 different jet velocities between 0.36 and 0.81 m/s gave sensitivities varying within this error band (PS96). This result shows, that the potential flow theory (equation 2) is valid even for the small airfoil of the PNS 93 shear probe.

4 Dissipation rate calculation

To calculate dissipation rates from current shear measured by PNS 93 shear probe, the procedure as described in PS96 was used. Here we give a brief summary of the steps of computation, for details we refer to PS96.

After validation of raw data (transmission error check, despiking), physical values of the current shear are calculated from shear probe voltage output. Within this procedure, the data are transferred from frequency domain into wavenumber domain (cyclic wavenumber). The starting point for the dissipation rate calculation is the isotropic formula (Batchelor, 1953):

$$\varepsilon = 7.5 \nu [(\partial u/\partial z)^2] \tag{5}$$

Here, $\partial u/\partial z$ is the vertical gradient of the horizontal current shear fluctuation. To suppress high and low frequency disturbances, the raw shear profile is filtered using a non-recursive digital bandpass filter (Walraven, 1984) in the wavenumber range from $k = 2$ cpm to $k_c/2$. About 86% of the variance is obtained if the turbulence spectrum is integrated up to $k_c/2$. For the calculation of the variance, we use the summation method. To correct for the unresolved 14% of the variance, the computed dissipation is multiplied by 1.16.

A comparison between dissipation rates calculated from MST Profiler shear measurements following the procedure described above and dissipation rates determined from temperature microstructure measurements as described e.g. by Oakey (1982) and Gloor et al. (1995) have been made by Kocsis et al. (1997). The inter-comparison is based on an 11 day measuring campaign in Lake Neuchâtel (Switzer-

land) in March 1996. Two profilers horizontally separated by 35 m, were simultaneously operated every 15 minutes. The 3 hour mean dissipation rates for 1 m depth intervals agreed within a factor of two in the dissipation range between approx. 10^{-10} and $5 \cdot 10^{-8}$ W/kg, which is probably the best achievable agreement in dissipation measurements by different profilers (Moum et al., 1995).

To calculate the pseudo-dissipation rate of the MST Profiler, we used a method described by Moum and Lueck (1985). The horizontal acceleration of a sinking profiler is related to the shear signal measured by the shear probe by

$$du/dz = a/V, \quad (6)$$

where a is the horizontal acceleration of the profiler and V is its sinking velocity. The acceleration is measured by the vibration control sensor which is calibrated in terms of horizontal acceleration. The pseudo-dissipation then, can be written as

$$\epsilon_p = 7.5\nu \overline{(a/V)^2}. \quad (7)$$

5 Upper dissipation rate detection limit

The upper dissipation rate detection limit of the PNS 93 shear probe was estimated based on its vertical and temporal resolution. The vertical resolution is determined by the length of the airfoil, while the temporal resolution is determined by the resonance frequency of the probe. If the airfoil-cantilever construction of the shear sensor comes into resonance, the velocity fluctuation signal is covered by the resonant airfoil oscillations.

The application of the Allen and Perkins (1952) theory for airfoil shear probe measurements is based on the assumption, that there is no dependence of the sensor output on the frequency of the cross-stream component of the velocity field. This assumption is valid as long as the frequency of the excitation force (cross-stream velocity component) is small compared to the resonance frequency of the shear probe. Measurements of the frequency response curve of the PNS 93 shear probe (Prandke, 1994) show a well pronounced narrow-band resonance peak at about 315 Hz, see Fig. 3. In the frequency range below the resonance peak (below about 270 Hz) no systematic frequency dependent sensor output could be detected.

The frequency of the excitation force at the tip of the shear probe f_{ex} depends on the vertical scale of the cross-stream component of the turbulent velocity field L_v and the sinking or rising velocity V of the profiler:

$$f_{ex} = V/L_v \quad (8)$$

The smallest vertical wavelength of the cross-stream component of the turbulent velocity field (cut off wavelength), which produces the highest frequency, depends on the dissipation rate of kinetic energy. However, vertical structures smaller than its spatial response length cannot be sensed by the airfoil. As shown by Ninnis (1984), the -3 dB point of the spatial transfer function of the Osborn/Oakey shear probes corresponds to a length scale of 14.4 and 17.9 mm, respectively. The airfoils

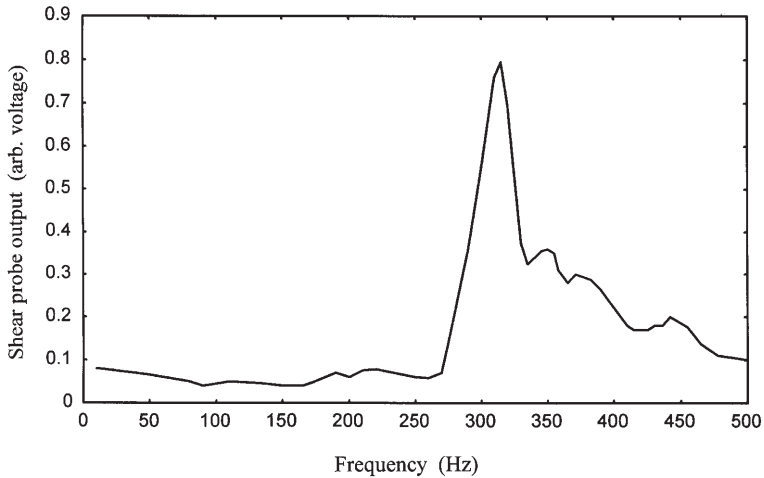


Figure 3. Frequency response of PNS 93 shear probe. The probe was held in water and was excited by sideward metallic shocks (broad band excitation) at the shaft of the sensor. The output voltage was measured electronically by a spectrum analyser. The spectrum plotted by the analyser is based on 32 measured individual spectra. Each spectrum covers several bangs

of the Osborn/Oakey and the PNS shear probes have a similar shape. This allows one to adapt the results of the investigations of Ninnis (1984) to the PNS 93 shear probes, which give a spatial resolution of 5.25 mm. Assuming 5.25 mm as the smallest L_v value and a profiling velocity of 0.75 m/s, equation (8) gives an excitation frequency of about 143 Hz. This is well below the critical resonance frequency of the PNS 93 shear probe (Fig. 3).

Following the procedure of dissipation rate computation from shear measurements as described above, this spatial resolution enables the detection of dissipation rates up to about 10^{-4} W/kg (corresponding to $k_c/2 \approx 185$ cpm, see equation 1). This is an upper value for most conditions in natural waters. Thus, no correction of the transfer function is necessary for PNS 93 probes. This, however, usually has to be done for probes of the Osborn/Oakey type (see e.g. Moum et al., 1995).

In situations of extremely high dissipation rates exceeding 10^{-4} W/kg, a correction for the spatial response of the PNS 93 shear probe at wavenumbers exceeding 185 cpm is recommended. Figure 4 shows these correction factors for the PNS 93 shear probe, which have been derived from the Nasmyth turbulence spectrum (Nasmyth, 1970).

6 Profiler vibrations

To investigate the level and the frequency range of profiler vibrations due to vortex shedding caused by surficial features on the hull of the profiler and structural resonance of the hull, the sensor mounts and internal components, we performed a special series of test measurements. With respect to a low level of turbulence, a calm

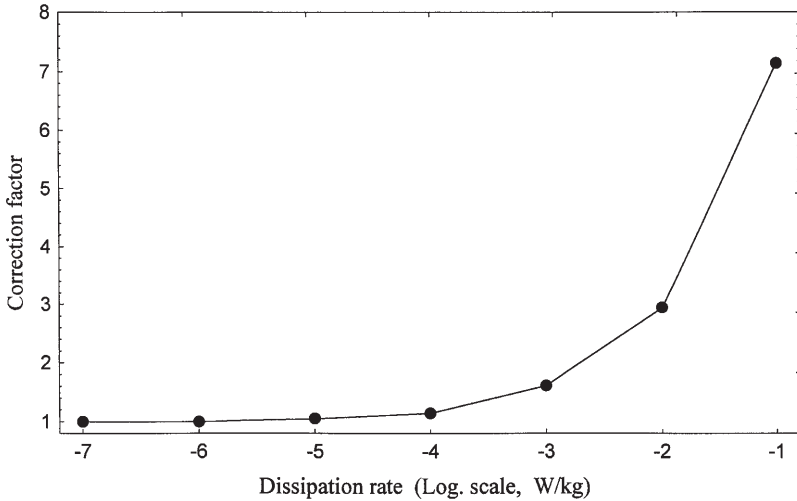


Figure 4. Correction factor for the PNS 93 shear probe at wavenumbers greater than 200 cpm as derived from Nasmyth's universal turbulence spectrum (Nasmyth, 1970). To correct for unresolved variance due to limited spatial resolution, the calculated dissipation rates have to be multiplied by the correction factor

period on December 7 1995 in Lago Maggiore (Italy) was selected. The measurements were carried out from a small boat drifting on the lake. The water at the site of the measurements was nearly stagnant (drift of the boat about 300 m in 4 hours). The water depth was about 140 m.

In a first experiment the resonance frequency of the hull itself was determined. For this purpose the profiler housing was attacked with short sideward strokes (broad band vibration excitation) while hanging from the cable in the near surface water. The spectrum of the internal vibration of the profiler (see Fig. 5) shows a pronounced peak at 150 Hz. This dominant peak is the expected value for the profiler housing resonance oscillations. For comparison, the improved Advanced Microstructure Profiler (AMP) of APL, Seattle/USA which has dimensions similar to the MST Profiler, has a hull resonance frequency of 166 Hz (Miller et al., 1989). The peak at 150 Hz is well above the dissipation frequency range. At sinking velocities of the profiler below 0.75 m/s (as recommended for the MST Profiler), the 150 Hz resonance frequency corresponds to wavenumbers above 200 cpm.

To investigate in detail the occurrence of profiler vibrations in the frequency range below 150 Hz, 14 profiles were taken at different sinking velocities ranging from 0.36 to 1.28 m/s. The depth range of the measurements was approximately 5 m to 25 m. In the frequency range below 150 Hz three separated peaks in the current shear spectra could be identified, referred to P1, P2, and P3, respectively, which simultaneously occurred in the spectra of the vibration sensor. P1 occurred in all spectra, while the less pronounced peaks P2 and P3 could not be detected in all 14 profiles. Figure 6 shows an example of the spectra of the measured current shear values and internal profiler vibrations as calculated for each of the 14 profiles. The frequency of the P1 peak, ranging from 10 to 40 Hz, was found to increase with the

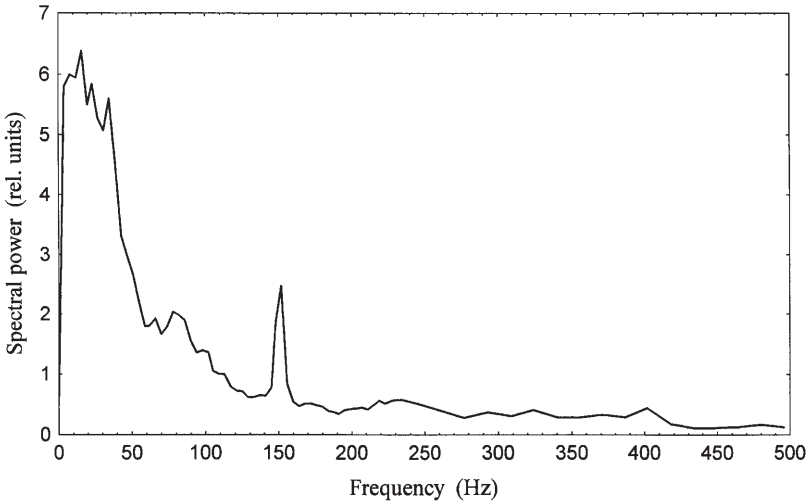


Figure 5. Underwater resonance spectrum of the MST Profiler, measured by the internal vibration sensor. The profiler was hanging in water and was excited by sideward strokes at its housing

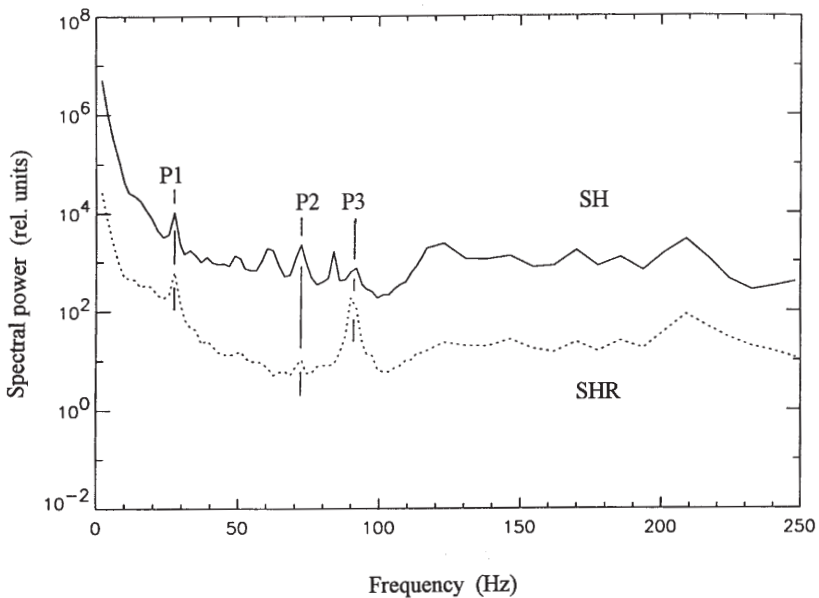


Figure 6. Energy spectra of current shear (SH) and internal vibration (SHR) raw data of a test profile in Lago Maggiore. Depth range: 5 to 25 m, sinking velocity about: 0.8 m/s. In the frequency range below 150 Hz three peaks simultaneously occur in the current shear and internal profiler vibration at ≈ 30 Hz (P1), ≈ 72 Hz (P2), and ≈ 90 Hz (P3), respectively

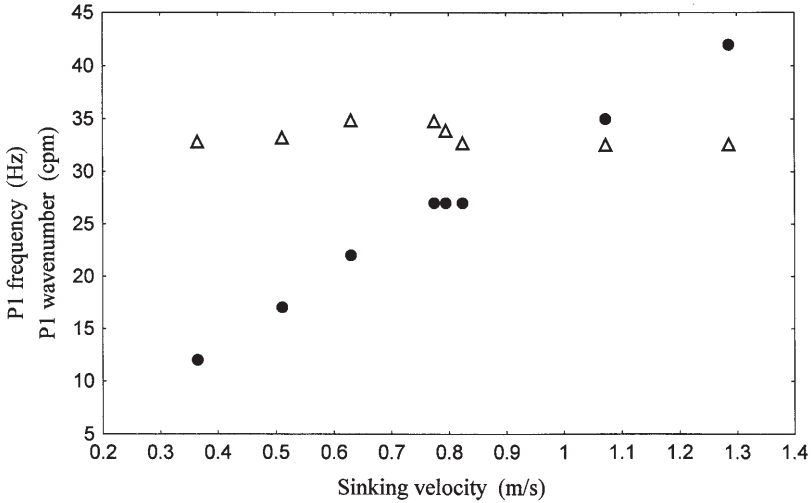


Figure 7. Frequency (filled circles) and wavenumber (open triangles) of peak P1 in the current shear and internal vibration spectra as a function of the sinking velocity of MST Profiler

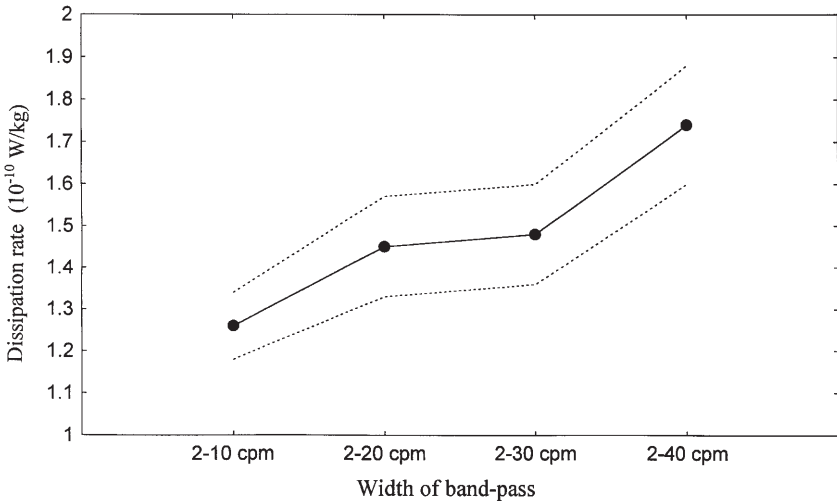


Figure 8. Dissipation rates dependent on the width of the pass band of the filter applied to the shear profiles. Mean dissipation from 6 profiles with the lowest turbulence level from the test measurements on December 7 1995. Broken lines: confidential interval

sinking velocity, while its corresponding wavenumber showed a constant value of about 33 cpm for all profiles (see Fig. 7). This behaviour of P1 leads to the assumption that this peak is caused by vortex shedding, probably at the sensor arrangement. The size of such eddies depends on the geometry of the place of generation, independent of the sinking velocity. Consequently, in the wavenumber domain

they occur at a fixed point while in the frequency domain they change with the sinking velocity. The P2 and P3 peaks exhibited quite different behaviour. The frequencies at which the peaks were observed, 72 and 90 Hz, respectively, were independent of the sinking velocity. Because of their constant frequencies, the peaks P2 and P3 were probably related to vibrations of internal components of the profiler.

The P1 peak is more critical with respect to dissipation measurements than the P2 and P3 peaks. To investigate the influence of the P1 peak we calculated mean dissipation rates for different widths of the band-pass for the 6 profiles with the lowest turbulence levels (profiles No. 7 to 12). The mean dissipation rate of these profiles was about $1.5 \cdot 10^{-10}$ W/kg, which corresponds to a Kolmogoroff wavenumber of 15 cpm. The width of the band-pass filter was chosen to be 2 to 10 cpm, 2 to 20 cpm, 2 to 30 cpm, and 2 to 40 cpm, respectively. As shown in Fig. 8, the calculated dissipation rates are almost constant if the upper bound of the band-pass exceeds the Kolmogoroff wavenumber. The increase of ϵ of about $2.5 \cdot 10^{-11}$ W/kg from 2–30 cpm to 2–40 cpm is due to the contribution of the P1 peak. The wavenumber range above 30 cpm, however, is relevant for ϵ values larger than $5 \cdot 10^{-9}$ W/kg only. At this dissipation level the relative error caused by the P1 peak is negligible. Due to their higher frequencies, the influence of the P2 and P3 peaks is even smaller than that of P1.

7 Lower limit of dissipation rate estimates

The lower limit of dissipation rate estimates can be estimated in two different ways: By data sampling at sites with very low levels of natural turbulence or by calculation of the pseudo-dissipation rate produced by the internal vibrations of the profiler. The first method is based on the assumption, that under specific conditions the natural level of dissipation can be below the noise of the profiler. The latter method requires the measurement of the horizontal profiler acceleration during the profiling process. We used both methods and compared the results.

Generally, if the profiling velocity of an in situ instrument is increased, an increase of the pseudo-dissipation rate can be expected due to more intense vortex shedding or the excitation of profiler vibrations. To investigate this behaviour for the MST Profiler, pseudo-dissipation rates using equation 7 were calculated for the profiles performed on December 7 1995 (see previous chapter) at different sinking velocities. As shown in Fig. 9, the expected increase of ϵ_p was found in the low velocity range. ϵ_p varied from about $5 \cdot 10^{-12}$ W/kg at 0.4 m/s to about $4 \cdot 10^{-11}$ W/kg at 0.8 m/s sinking velocity. At velocities above 0.8 m/s, however, ϵ_p was constant at about $4 \cdot 10^{-11}$ W/kg. We have no fully satisfying explanation for this behaviour of the pseudo-dissipation. Once excited, we assume a constant level of internal component's (e.g. electronic boards) resonant vibrations.

To compare the limit of dissipation of the MST profiler based on acceleration estimates with turbulence measurements, we used a turbulence set of data collected in Lago Maggiore. The data set consists of 291 uprising profiles from about 30 m depth to the surface, taken in 15 minute intervals between December 18 and 21 1995. Concerning the dissipation level, three main regions in the two dimensional depth-time plot of the data could be identified (see Fig. 10): A near surface layer

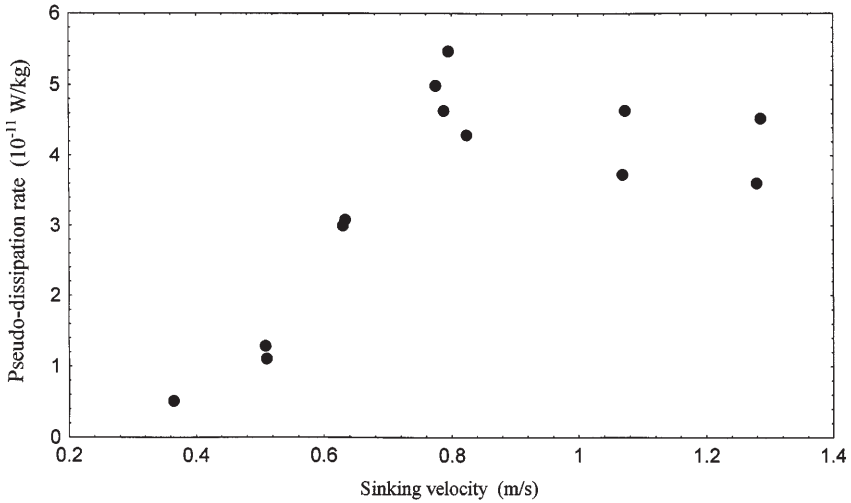


Figure 9. Dependency of pseudo-dissipation rate ε_p on the sinking velocity of the MST Profiler for the test measurements in Lago Maggiore, December 7 1995

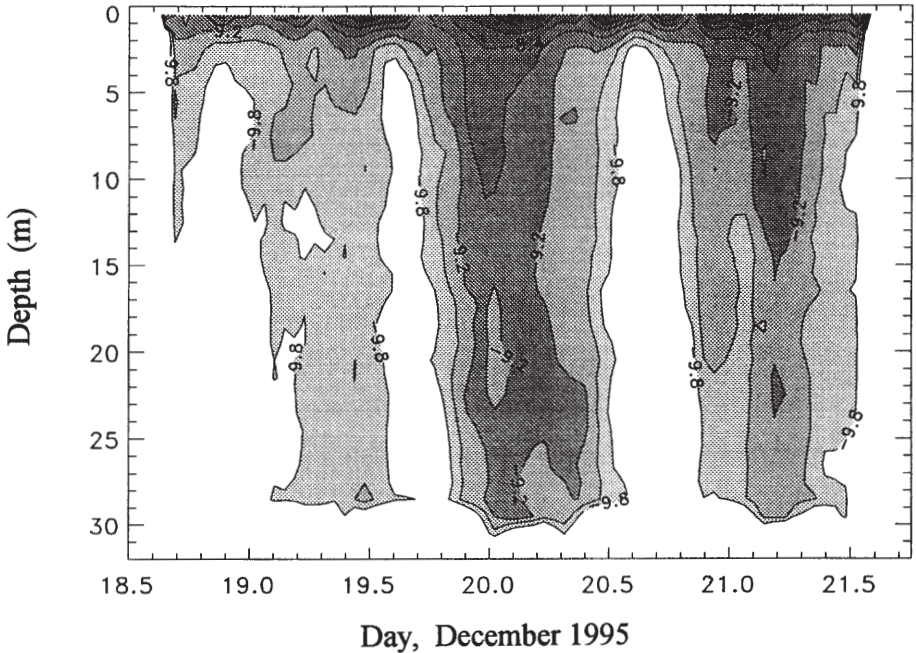


Figure 10. Dissipation rates during a measuring campaign from December 18 to 21 1995 in Lago Maggiore. The MST Profiler was used in rising mode. The periods of increased turbulence from day 20 to 20.5 and 21 to 21.5 are related to wind events (max. wind speed 5 m/s) combined with thermal convection. The contours of \log_{10} of dissipation ε [W/kg] refer to: -9.8, -9.5, -9.2, -8.8, -8.4, -8.0, -7.5, -7.0, -6.5

Table 2. Dissipation rates for different regions and pseudo dissipation for the measuring campaign December 18 to 21 1995 in Lago Maggiore

Region or type of dissipation	Mean dissipation rate (arithmetic mean) (10^{-10} W/kg)	Peak of distribution (10^{-10} W/kg)	Population mean of distribution (mean of logarithmic-normal distribution) (10^{-10} W/kg)
Near surface layer	9.6	4.9	23.0
Wind periods	6.0	5.3	8.5
Calm periods	1.1	0.88	1.6
Pseudo dissipation	0.66	0.7	0.72

between 0 and 3 m depth showed variable and mostly higher dissipation values compared to those measured in greater depth. In the depth range below 3 m a rather low and fairly homogeneous “background” dissipation level occurred during calm periods. Higher turbulence intensities in that depth range were recorded during two periods which were related to events of increased wind speeds and thermal convection. For these three main regions of turbulence intensity, the distributions of ϵ values as well as the distribution of ϵ_p values were calculated (depth interval 0.6 m). Table 2 gives the parameters of the distributions.

The distributions of dissipation rate obtained in near surface layer, wind periods and calm periods are roughly log-normal, while the distribution of the pseudo dissipation roughly fits a normal distribution.

The population means of dissipation rates during wind periods and in the near surface layer are more than one order of magnitude above the pseudo dissipation rate. The dissipation during calm periods, however, is about twice the pseudo dissipation only. To distinguish between profiler noise and natural turbulence, the mean nondimensional shear spectrum for this period was computed and compared with the Nasmyth spectrum. As shown in Fig. 11a, the shear spectrum during the calm periods fits well with the Nasmyth spectrum. The slope between 0.2 and 1.0 in the nondimensional wavenumber range nearly perfectly agrees with that of the universal turbulence spectrum. At a nondimensional wavenumber of 0.1 the Nasmyth spectrum is underestimated by about 50%. Compared with the spectrum from calm periods, the mean spectrum of pseudo dissipation shows less agreement with the Nasmyth spectrum (Fig. 11b). Here, the universal turbulence spectrum is underestimated in the nondimensional wavenumber range between 0.1 and 0.3 up to 80%, while the slope in the nondimensional wavenumber range between 0.4 and 1 is overestimated. Furthermore, at the nondimensional wavenumber 0.75 a significant peak occurs which is not present in the calm periods shear spectrum.

This result leads to the conclusion, that the observed background dissipation level does not reflect the profiler generated pseudo-dissipation. Consequently, the measured dissipation rates during calm periods present the natural turbulence level.

The measurements from December 18 to 21 1995 were carried out with an up-rising speed of about 0.7 m/s. According to Fig. 9, this velocity corresponds to a mean pseudo dissipation rate of about $3.5 \cdot 10^{-11}$ W/kg. However, a mean pseudo-

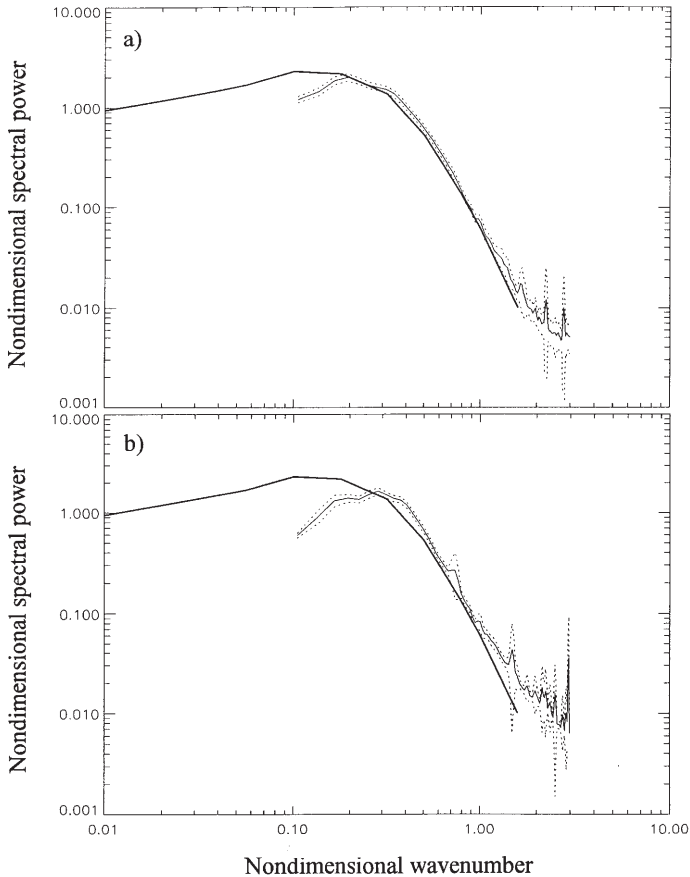


Figure 11. Nondimensional mean shear spectrum of calm periods (a), and nondimensional mean pseudo dissipation spectrum (b) during the measuring campaign from December 18 to 21 1995 in Lago Maggiore (thin lines). Bold lines: nondimensional universal shear spectrum after Nasmyth (1970) (taken from Oakey, 1982). The nondimensional shear spectrum $G_2(k/k_c)$ has been calculated from Tab. A.1 in Oakey (1982). Cyclic wavenumber notation has strictly been used (i.e. the calculation of the Kolmogoroff wavenumber followed eq. 1)

dissipation rate of $7.2 \cdot 10^{-11}$ W/kg was observed. This higher value can be explained by additional sources of profiler vibrations at the uprising mode of operation compared to free sinking measurements: The short cable (some metres) between profiler and buoyancy body, hanging below the profiler, can generate vibrations. Furthermore, the short cable can transmit a small part of the pronounced vibrations of the buoyancy body to the profiler. Consequently, during uprising measurements the pseudo dissipation level increased approximately by a factor of 2 compared to sinking measurements. This difference should be taken into account.

Summary and conclusions

We have investigated the properties of the MST Profiler microstructure measuring system with respect to the determination of dissipation rates. The focus was on the profiler's internal vibration level and its lower detection limit for dissipation rate estimates. The upper detection limit was estimated based on the geometry and size of the current shear sensor.

Test measurement in Lago Maggiore under quiet conditions gave no indication of pronounced internal profiler vibrations interfering with dissipation measurements. Pseudo dissipation rates of the MST Profiler based on profiler vibration measurements were found to be strongly dependent on the profiler velocity. At sinking measurements with different profiler velocities, pseudo dissipation rates between $5 \cdot 10^{-12}$ W/kg at 0.4 m/s and $4 \cdot 10^{-11}$ W/kg at 0.8 m/s, respectively, were determined.

During three days of measurements in Lago Maggiore the mean dissipation level in calm periods was found to be about $1.6 \cdot 10^{-10}$ W/kg. This is about twice the mean pseudo dissipation level under the specific conditions of the measurements (rising MST Profiler, profiler velocity about 0.7 m/s). The satisfactory fit of the mean non-dimensional shear spectrum with the universal turbulence spectrum, and the lack of a good fit between mean nondimensional pseudo dissipation spectrum and the shape of the turbulence spectrum give rise to the conclusion that the measured shear in calm periods presents the natural level of turbulence. Furthermore, it can be concluded that the measured mean pseudo dissipation of $7.2 \cdot 10^{-11}$ W/kg is a realistic estimate for the lower detection limit of the MST profiler under the conditions of the data collection.

The results of the investigations of the lower limit of dissipation rate estimates can be summarised as follows:

1. The mean pseudo dissipation determined from horizontal vibrations of the MST Profiler presents the lower limit of dissipation rates estimates under the specific measurement condition.
2. At sinking measurements with low profiler velocities (0.4 m/s) and quiet conditions (calm, nearly stagnant water), the pseudo dissipation of the MST Profiler can be as low as $5 \cdot 10^{-12}$ W/kg.
3. During sinking measurements with a more practical profiler velocity of 0.7 m/s (as recommended for the MST Profiler) during quiet conditions the pseudo dissipation is about $3.5 \cdot 10^{-11}$ W/kg.
4. During rising measurements with additional sources of profiler vibration (cable hanging below the profiler), pseudo dissipation rates are higher by a factor of about 2 compared to sinking measurements with the same profiling speed.
5. Under normal environmental conditions (e. g., wind waves, current shear at pycnoclines) additional sources of profiler vibrations have to be taken into account. Consequently, an increase of the pseudo dissipation of the MST Profiler dependent on the specific conditions has to be considered.

In the high dissipation range the detection limit is set by the spatial response of the shear probe. For the PNS 93 shear probe of the MST Profiler an upper detection

limit of 10^{-4} W/kg was estimated. Dissipation rates up to this level can be measured without corrections for unresolved variance of the shear spectrum.

Rating the results of our investigations, we conclude that the MST Profiler is well optimised for measuring marine and limnic turbulence. With its range of the dissipation rate of turbulent kinetic energy from about 10^{-11} W/kg (dependent on measuring conditions) to about 10^{-4} W/kg it covers the dissipation rates occurring in most natural waters. Thus, the MST Profiler is a useful instrument for making marine and limnic turbulence measurements.

ACKNOWLEDGEMENT

The development of the MST Profiler was funded by the German Federal Ministry for Education, Research and Technology under contract no. FKZ 03F0136A.

Useful comments for this paper were provided by anonymous referees.

REFERENCES

- Allen, H.J. and E.W. Perkins, 1952. A study of effects of flow over slender inclined bodies of revolution. Report No. 1048, U.S. National Advisory Committee for Aeronautics.
- Batchelor, G.K., 1953. The theory of homogeneous turbulence. Cambridge University press, Cambridge, 197 pp.
- Box, J., 1992. A comparison of shear probe calibration facilities at the Universities of Victoria and Washington. Ocean Turbulence Laboratory Report No. 92-01, University of Victoria, Centre for Earth and Ocean Research, Victoria B.C.
- Dewey, R.K. and W.R. Crawford, 1988. Bottom stress estimates from vertical dissipation rate profiles on the continental shelf. *J. of Physical Oceanography*, 18: 1167–1152.
- Gloor, E.U., O. Kocsis, M. Omlin, M. Schurter and A. Wüest, 1995. Temperaturmikrostrukturen, eine Methode zur Bestimmung der Mischungsintensität in geschichteten Gewässern. *Gas Wasser Abwasser*, 75: 1087–1096.
- Kocsis, O., H. Prandke, A. Simon, A. Stips, and A. Wüest, 1997. Comparison of dissipation of turbulent kinetic energy determined by shear and temperature microstructure. Submitted to *J. of Marine Systems*.
- Miller, J.B., M.C. Gregg, V.W. Miller and G.L. Welsh, 1989. Vibration of tethered microstructure profilers. *J. of Atmospheric and Oceanic Technology* 6: 980–984.
- Moum, J.N., M.C. Gregg, R.C. Lien and M.E. Carr, 1995. Comparison of turbulence kinetic energy dissipation rates estimates from two ocean microstructure profilers. *J. of Atmospheric and Oceanic Technology* 12: 346–366.
- Moum, J.N. and R.G. Lueck, 1985. Causes and implications of noise in oceanic dissipation measurements. *Deep-Sea Research* 32: 379–390.
- Nasmyth, P.W., 1970. Oceanic turbulence. Ph.D. dissertation, University of British Columbia, Vancouver, 1970.
- Ninnis, R., 1984. The effect of spatial averaging of airfoil probe measurements of oceanic velocity microstructure. Thesis, University of British Columbia, October 1984.
- Oakey, N.S., 1977. An instrument to measure oceanic turbulence and microstructure. Bedford Institute of Oceanography, Report, Ser. B1-R-77.
- Oakey, N.S., 1982. Determination of the rate of dissipation of turbulent energy from simultaneous temperature and velocity shear microstructure measurements. *J. of Physical Oceanography* 12: 256–271.
- Osborn, T.R., 1980. Estimates of the local rate of vertical diffusion from dissipation measurements. *J. of Physical Oceanography* 10: 83–89.
- Osborn, T.R. and W.R. Crawford, 1977. Turbulent velocity measurement with an airfoil probe. IOUBC Manuscript Report No. 31.

- Osborn, T.R. and W.R. Crawford, 1980. An airfoil probe for measuring turbulent velocity fluctuations in water. Ch. 19 in *Air-Sea Interaction: Instruments and methods*. F. Dobson, L. Hasse and R. David (editors), Plenum Press, New York, 369–386.
- Prandke, H., 1994. Tests and intercalibrations of an improved airfoil shear probe. ME Meerestechnik-Elektronik GmbH, Trappenkamp, Technical Report, April 1994.
- Prandke, H. and A. Stips, 1996. Investigation of microstructure and turbulence in marine and limnic waters using the MST Profiler. Technical Note No. I.96.87, European Commission, Joint Research Centre, Space Applications Institute, Ispra/Italy.
- Walraven R., 1984. Digital filters. Proceedings of Digital Equipment User's Society, Fall, 1984, Department of Applied Sciences, University of California, Davies, CA.
- Wesson, J.C. and M.C. Gregg, 1994. Mixing at Carmarinal Sill in the Strait of Gibraltar. *J. of Geophysical Research* 99: 9847–9878.

Received 7 March 1997;

revised manuscript accepted 31 March 1998

Investigation of turbulent mixing in shallow lakes using temperature microstructure measurements

Andreas Lorke

Institute of Freshwater Ecology and Inland Fisheries, Mueggelseedamm 260, D-12587 Berlin, Germany

Key words: Lake, mixing, mixed layer, temperature microstructure.

ABSTRACT

A microstructure profiler was designed especially for the investigation of the diurnal dynamics of turbulent mixing in shallow lakes. 7 hours observation of these dynamics in a shallow, polymictic lake shows a multitude of different mixing processes acting together on very short time-scales. Estimated turbulent diffusivities for the surface mixed layer, using the Cox number method, are lognormally distributed with a mean of $K_z \approx 10^{-5} \text{ m}^2 \text{ s}^{-1}$. The results are discussed within the context of their relevance for modelling the effect of turbulent mixing on phytoplankton primary production.

Introduction

Physical forcing is becoming increasingly recognised as an important factor in the functioning and dynamics of aquatic ecosystems. This is, among other factors, the result of an increase in the amount of data available on turbulent mixing in the natural environment. Microstructure profilers, which are able to resolve the vertical distribution of temperature and current shear down to the smallest scales, can be used to investigate the extent and intensity of active turbulent mixing in direct relation to the meteorological forcing. The smallest scales involved are the Kolmogorov scale $L_K = (\nu^3/\epsilon)^{1/4}$ (Tennekes and Lumley, 1973) and the Batchelor scale $L_B = (D^2\nu/\epsilon)^{1/4}$ (Batchelor, 1959). L_K is the scale of the smallest velocity fluctuations which may persist at a given dissipation rate of mechanical energy ϵ before they are damped out by the kinematic viscosity ν . L_B is the scale of the smallest temperature fluctuations which may persist before they are damped out by the molecular diffusivity of heat D . A typical dissipation rate for stratified waters of $\epsilon \approx 10^{-8} \text{ W kg}^{-1}$ results in a Kolmogorov scale of $L_K \approx 4 \text{ mm}$ and a Batchelor scale of $L_B \approx 1.4 \text{ mm}$.

Microstructure profilers have been used for several years in marine and lake research (Oakey, 1982; Imberger, 1985; Gregg, 1987; Pagenkopf, 1990). Different approaches to obtain information on mixing intensities from temperature microstructure profiles exist. A very vivid method is to calculate the displacement length

scales by reordering the temperature profile to the associated stable profile. The displacement length is defined as the vertical displacement of a data point with respect to its position in the stable profile. The average displacement length scales, or Thorpe scales (Thorpe, 1977), are a measure of the vertical extent of overturning eddies (Imberger and Ivey, 1991). The Cox number method (Osborn and Cox, 1972) can be used to calculate the turbulent diffusivities. The basic assumption underlying this method is the existence of an equilibrium between temperature gradient production due to turbulence and temperature gradient dissipation due to molecular diffusion.

The results of these microstructure measurements are used to identify different mixing mechanisms and to determine the general physical features of the ocean or lakes. In a next step, the physical-biological coupling can be considered. Mostly, this coupling is a result of the physical forcing of biological and biogeochemical processes, but in some cases a forcing in the reverse direction has also been observed (Wüest, 1994).

Because of the spatial proximity of different ecosystem compartments (pelagic, littoral and benthic zones) in small and shallow inland waters, the physical-biological interactions there are much stronger than in the open waters of marine or lacustrine environments. Exchange and interaction between these compartments may act on much smaller time scales and are more related to meteorological or hydrodynamical parameters. A moderate increase in wind speed, for instance, can dramatically change the chemistry of the water overlying the sediments from anaerobic to aerobic. Differential cooling or mixed-layer deepening can act as additional driving forces for advective exchange between the pelagic and littoral zones.

The dynamics of turbulent mixing and the prospects of measuring it in shallow lakes are discussed in this paper. The microstructure profiler used for these investigations is designed for taking measurements in shallow lakes and combines some features of different profilers described in the literature (Carter and Imberger, 1986; Moum et al., 1995). An example of the diurnal dynamics of mixing is used to calculate typical time and space scales of mixing and stratification as directly related to meteorological forcing.

Materials and methods

Sampling site

Measurements were performed in Müggelsee, a shallow, polymictic lake situated in NE Germany near Berlin (see Fig. 1). Müggelsee has an area of 7.3 km², a mean depth of 4.9 m, a maximum depth of 8 m and is flushed by the river Spree with a retention time of about 40 days (Driescher et al., 1993). For further details see Driescher et al. (1993).

Microstructure measurements

A special microstructure profiler was developed for use in shallow lakes. Since investigations focus on processes in the surface mixed layer a rising profiler is used.

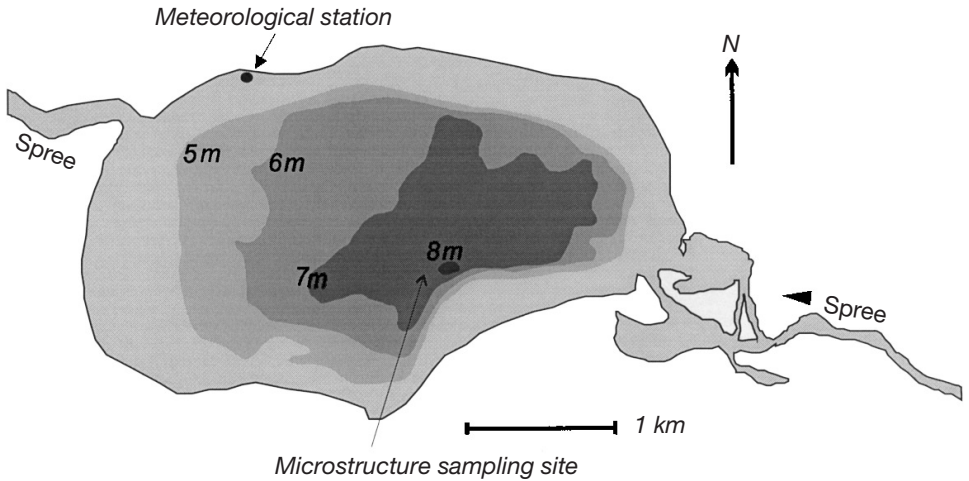


Figure 1. Characteristics of Müggelsee. The microstructure sampling site and the location of the meteorological station are indicated

It is equipped with an FP07 thermistor probe for temperature microstructure measurements. A pressure transducer and a two-axis clinometer are used to obtain information about the profiling pathway.

Following an idea of Carter and Imberger (1986), a specially designed weight is used to force the profiler to glide down at an angle of about 45° to the vertical when it is employed from a boat. The advantage of this method is that the profiler moves away from the boat and the water column above the profiler is not disturbed by its deployment. The weight can be released at a certain depth allowing the profiler to rise to the surface. The release mechanism consists of an electromagnet which can be switched off either at a predefined depth, or manually. The weight of the electromagnet at the lower end of the profiler stabilises its vertical position during its rise. Sampling can be halted either automatically or manually when the profiler reaches the surface. If the profiler is released at the bottom of the lake, measurements can be performed from about 1 m above the bottom up to the surface. Microstructure measurements are taken with a sampling frequency of up to 1000 Hz. Pressure and inclination data are collected at 10 Hz. The rising speed of the probe can be adjusted by adding or removing weights. The maximum rising speed of the probe is about 0.6 m s^{-1} .

Displacement length scales are obtained by reordering the measured temperature profile to the stable profile and by calculating the vertical displacement of each data point to its position in the stable profile (Thorpe, 1977). The average displacement length scales are an indicator for overturning eddies and thus for active mixing (Imberger and Ivey, 1991).

Turbulent diffusivities K_z were calculated using the Cox number method:

$$K_z = 3D \frac{\langle \partial T' / \partial z \rangle^2}{\langle \partial T / \partial z \rangle^2}$$

(Osborn and Cox, 1972), where $\partial T'/\partial z$ denotes the gradient of the temperature fluctuations, $\partial T/\partial z$ the mean temperature gradient and D the molecular diffusivity of heat ($\approx 1.4 \cdot 10^{-7} \text{ m}^2 \text{ s}^{-1}$). The mean gradient was calculated from the recorded, stable profile to ensure positive values, even during the convective period. Calculations were performed using 500-point ($\approx 30 \text{ cm}$) data segments. The results, obtained from individual microstructure profiles, were ensemble-averaged in groups of 3 to 8 diffusivity profiles. The Cox number method is used because it offers the advantage of fast and automatic data evaluation. If the mean temperature gradient is about zero, this method may overestimate the diffusivities due to measurement limitation of the mean gradient. An alternative approach to temperature microstructure data processing is the Batchelor (1959) method, which invokes fitting the high wavenumber range of the temperature gradient spectrum to the theoretical spectrum. The shape of the spectrum is universal and depends only on the dissipation rate of mechanical energy and on the dissipation rate of temperature fluctuations. Dillon (1982) as well as Caldwell and Paulson (1980) showed that the results of the Cox number method are comparable to those obtained by the more common Batchelor method, at least up to diffusivities of $\approx 3 \cdot 10^{-4} \text{ m}^2 \text{ s}^{-1}$. Dillon (1982) stated that discrepancies at higher diffusivities are probably due to uncertainties in the translation of dissipation rates to diffusivities. For further investigations, the dissipation rates based on current shear microstructure measurements should be a good test of the obtained results.

Results: An example of diurnal mixed-layer dynamics

On August 24, 1995, about 80 microstructure profiles were collected between 12:00 and 19:00. Microstructure measurements were carried out from a ship, located near the deepest point of the lake (Fig. 1).

Meteorological conditions

Meteorological data were measured directly at the lake (Fig. 1). The meteorological conditions in terms of the heat-budget components and the wind-energy input are shown in Figure 2. The net heat flux is calculated using the short-wave radiation from the sky, H_s , the long-wave radiation from the atmosphere, H_A , and from the lake water, H_w , and the sensible heat flux term, H_c . The heat flux components were estimated according to Imboden and Wüest (1995). The latent-heat flux could not be estimated, because humidity data were not available. The net heat flux is dominated by the diurnal cycle of the global radiation. The integrated net balance for this day is about zero ($0.48 \text{ W m}^{-2} \text{ d}^{-1}$). The wind energy input P_{10} was parameterized using $P_{10} = \rho_{\text{air}} C_{10} W_{10}^3$ (Imboden and Wüest, 1995). W_{10} is the wind speed measured at 10 m above the water, C_{10} the drag coefficient (≈ 0.001) and ρ_{air} the density of the air. The input of wind energy was characterised by an event starting at noon and lasting until 16:00. Maximum wind velocities measured at the shore station were about 6 ms^{-1} (hourly average). Towards the evening, the wind dropped and the lake began to restratify. In the early evening, convective mixing started, caused by a negative net heat flux.

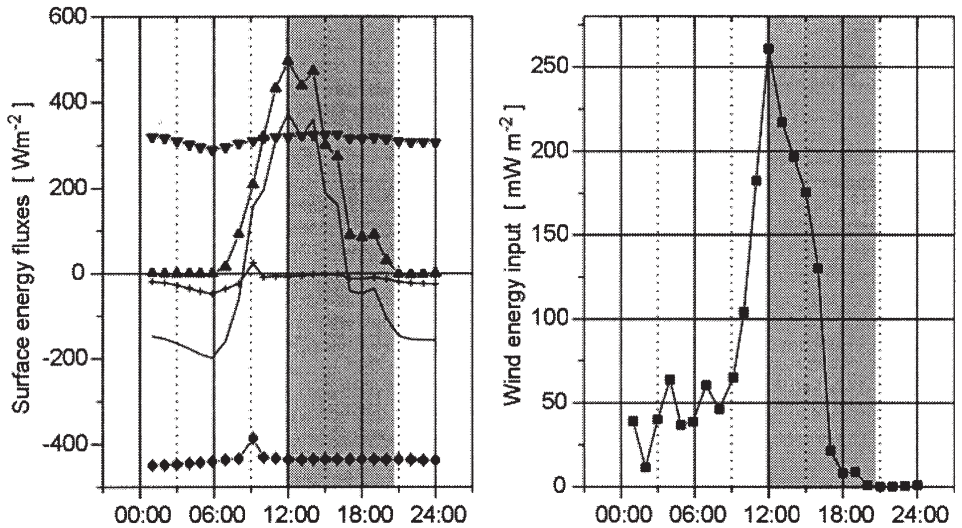


Figure 2. Thermal energy fluxes (left) and wind energy input P_{10} (right) into Müggelsee on August 24, 1995. The heat exchange components are: \blacktriangle global radiation H_S , \blacktriangledown long-wave atmospheric radiation H_A , \blacklozenge long-wave radiation emitted from the water H_W , $+$ sensible heat flux H_C . $-$ indicates the net heat exchange. The shaded region shows the period of microstructure measurements

Microstructure measurements

Figure 3 shows a series of temperature profiles. These profiles show active entrainment of the surface mixed layer from 2 to 5 m depth during the period of decreasing wind speed. After the wind dropped to zero (about 16:00), a temporary small thermocline was established between 1.5 and 2.5 m. This thermocline separated the convectively-mixed surface layer from the bulk of the former fully wind-mixed layer. Underneath this layer, a sharp, upwardly migrating thermocline developed. A line in Figure 3 indicates the prevailing depth of active mixing. This depth is estimated visually from individual displacement profiles. In the case of the entraining surface layer during the period of high wind speeds, there exists a sharp interface at the base of the mixing layer. The depth up to which overturning structures are present is clearly observable in the displacement profiles. Figure 4 shows a displacement profile where surface convection was present. The large overturning structure underneath the surface is a typical feature of thermal convection, with displacement length scales of up to the depth of the convectively-mixed layer. The turbulent patches in 2 and 4 m depth (Fig. 3) were probably produced by the current shear of the horizontal lake circulation after the wind ceased. They consist of smaller and overlapping eddy-like structures. The temperature profile in Figure 4 indicates effective mixing within these patches. These turbulent structures, and also the temperature profile underneath the convectively mixed surface layer, exhibit a high degree of temporal dynamics. This gives insight into the complex nature of the remaining horizontal currents in the lake, responding to the former wind event.

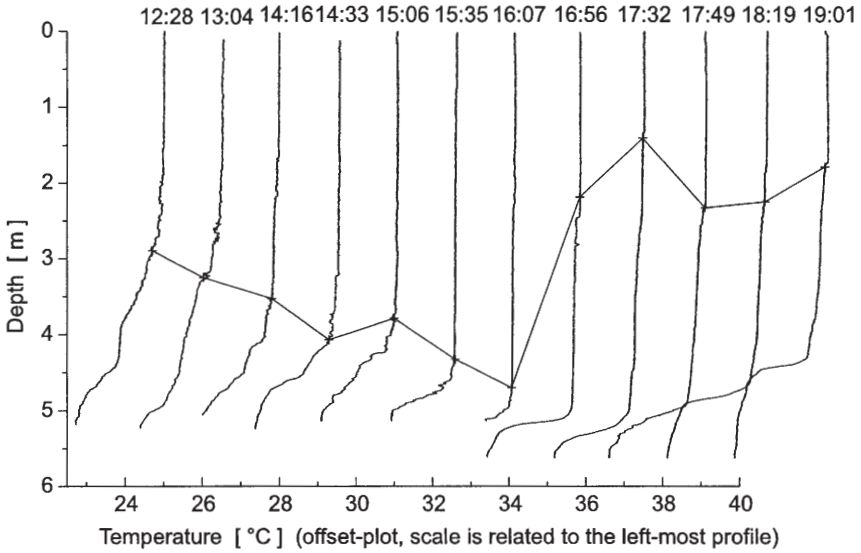


Figure 3. Temperature offset-plot of selected microstructure profiles from 24. August 1995. The sampling time is given above each profile. The line connecting the profiles indicates the prevailing depth of active mixing, as obtained from displacement profiles

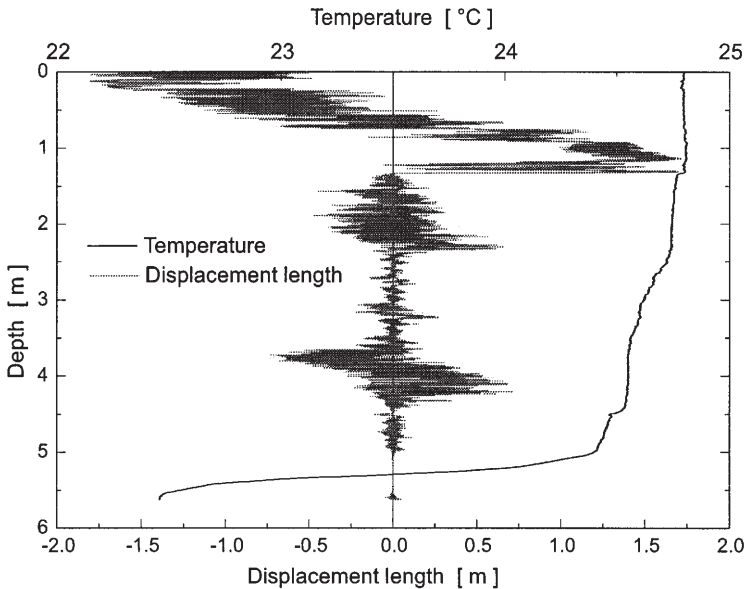


Figure 4. Temperature and displacement profile at 17:32 (see Fig. 3). The large-scale overturning structure from the surface to 1.5 m depth results from convective mixing

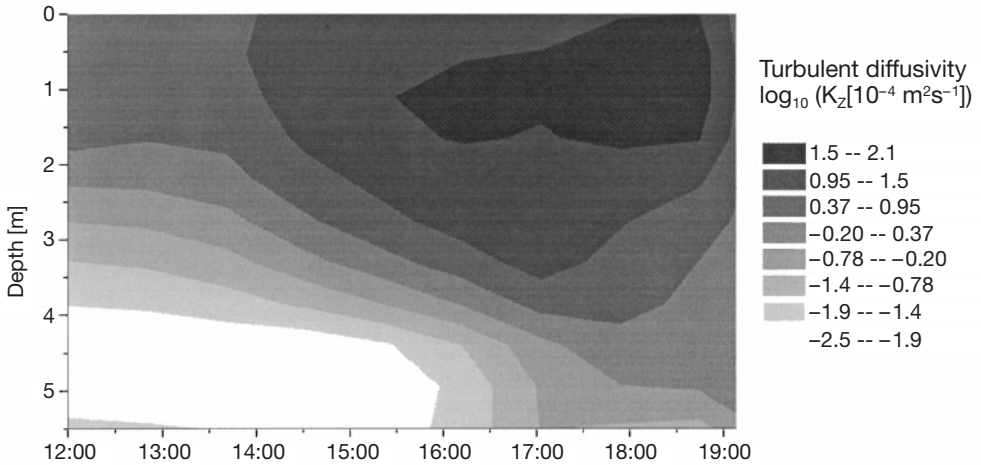


Figure 5. Time and depth distribution of turbulent diffusivities, obtained by the Cox number method

An interesting feature of the temperature profiles in Figure 3 is the upwardly migrating thermocline in 4.5 to 5 m depth which developed after the wind ceased (after 16:00). For this thermocline motion, there exists no surface-induced mechanism. However, such motion may be produced by a basin-wide circulation of the lake, responding to the wind pulse. With the onset of the wind, the water surface would tilt towards the upwind direction, producing upwelling at the upwind shore and downwelling at the downwind shore. A thermocline would tilt in an inverse manner. When the wind drops, the water masses would flow back and a seiche would be set up. At a sampling site situated downwind from the centre of the tilt, the described phenomenon appears. However, the sampling time was too short to calculate a period for this motion. Moreover, the seiche set-up was combined with active entrainment, so that the initial depth of the interface is unknown and the oscillation must be highly disturbed by the lake morphometry, because the thermocline is close to the bottom of the lake.

Figure 5 shows the turbulent diffusivities, calculated using the Cox-number method. The diffusivities follow the wind energy input with a certain delay, with maximum diffusivities and maximum depth extent of these high diffusivities at the end of the wind pulse. Thereafter the diffusivities remained high, but were increasingly confined to the near-surface layer. Maximum measured diffusivities were about $10^{-2} \text{ m}^2 \text{ s}^{-1}$.

Discussion and conclusions

The described example of the dynamics of mixing and stratification of the water column, responding to meteorological forcing, gives insight into the variety and complex nature of these processes in small water bodies. The general objective of

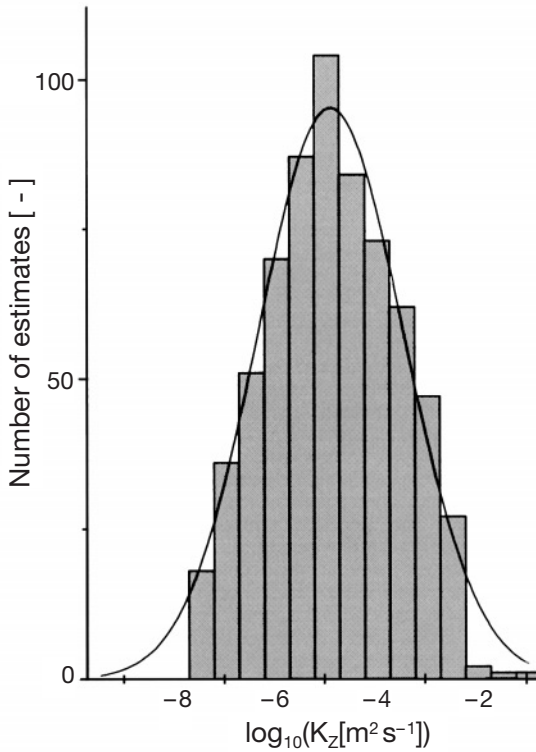


Figure 6. Frequency distribution of the logarithm of mixed-layer averaged diffusivities, measured under different meteorological conditions during summer in Müggelsee. The line shows a fit to a normal curve with a mean of $\approx 1.3 \cdot 10^{-5} \text{ cm}^2 \text{ s}^{-1}$

the microstructure investigations is to find typical time and space scales of mixing in such lakes in order to estimate the ecological relevance of these processes. Figure 6 shows the frequency distribution of observed turbulent diffusivities in the surface-mixed layer in Müggelsee. These diffusivities were obtained under different meteorological forcing conditions using the Cox number method, as described above. The distribution is nearly lognormal, as reported by Shay and Gregg (1986), Gibson (1991) and Wijesekera and Padman (1993) from oceanographic measurements. The mean of the lognormal distribution is about $10^{-5} \text{ m}^2 \text{ s}^{-1}$ and it covers five orders of magnitude, from 10^{-7} to $10^{-2} \text{ m}^2 \text{ s}^{-1}$. These values are comparable to those reported by MacIntyre (1993) from microstructure measurements, or those obtained by Powell and Richerson (1984) from tracer measurements in lakes.

Mean turbulent diffusivities, or even the diurnal dynamics of the depth and intensity of turbulent mixing, can be used to simulate the resulting fluctuating light climate of phytoplankton. Relevant models are described by various authors (Yamazaki and Kamykowski, 1991; Barkmann and Woods, 1996). The physical input to such a model can be the depth- and time-distribution of the turbulent diffusivities, as shown in Figure 5. On the other hand, the biological response of phyto-

plankton to fluctuating light is still a topic of ongoing research (Lande and Lewis, 1989; Livansky, 1995; Baumert, 1996). Phytoplankton productivity estimates incorporating simulated turbulent mixing in Müggelsee resulted in a 10% to 30% higher depth-integrated primary productivity than in the common, static, in-situ incubation of phytoplankton samples (Gervais et al., 1997). Even higher productivity enhancements were found during similar experiments (up to 328% by Nixdorf et al., 1992 or up to 87% by Marra, 1978 in the marine environment). Various empirical (Pahl-Wostl and Imboden, 1990; Franks and Marra, 1994) or physiological (Lande and Lewis, 1989) models exist for the dynamic underwater photosynthesis in fluctuating light regimes, which may be coupled to the physical model of turbulent mixed phytoplankton communities.

ACKNOWLEDGEMENTS

This work was financially supported by a German Research Foundation (DFG) grant to H. Behrendt.

REFERENCES

- Barkmann, W. and J.D. Woods, 1996. On using a Lagrangian model to calibrate primary production determined from in vitro incubation measurements. *J. Plankton Res.* 18:767–788.
- Batchelor, G. K., 1959. Small-scale variation of convected quantities like temperature in turbulent fluid. *Phil. Trans. Roy. Soc. London, A.* 5:113–133.
- Baumert, H., 1996. On the theory of photosynthesis and growth of phytoplankton. Part I: Light limitation and constant temperature. *Int. Revue. ges. Hydrobiol.* 81:109–139.
- Caldwell, D.R. and C.A. Paulson, 1980. The scaling of vertical temperature gradient spectra. *J. Geophys. Res.* 85:1917–1924.
- Carter G.D. and J. Imberger, 1986. Vertically rising microstructure profiler. *J. Atmos. Ocean. Technol.* 3:462–471.
- Dillon, T.M., 1982. Vertical overturns: A comparison of Thorpe and Ozmidov length scales. *J. Geophys. Res.* 87:9601–9613.
- Drietscher, E., H. Behrendt, G. Schellenberger and R. Stellmacher, 1993. Lake Müggelsee and its environment – Natural conditions and anthropogenic impacts. *Int. Revue. ges. Hydrobiol.* 78:327–343.
- Franks, J.S. and J. Marra, 1994. A simple new formulation for phytoplankton photoresponse and an application in a wind-driven mixed-layer model. *Mar. Ecol. Prog. Ser.* 111:143–153.
- Gervais, F., D. Opitz and H. Behrendt, 1997. Influence of small scale turbulence and large scale mixing on phytoplankton primary production. *Hydrobiologia* in press.
- Gibson, C.H., 1991. Turbulence, mixing and heat flux in the ocean main thermocline. *J. Geophys. Res.* 96:20,403–20,420.
- Gregg, M.C., 1987. Diapycnal mixing in the thermocline: A review. *J. Geophys. Res.* 92:5249–5286.
- Imberger, J., 1985. The diurnal mixed layer. *Limnol. Oceanogr.* 30:737–770.
- Imberger, J. and G.N. Ivey, 1991. On the Nature of Turbulence in a Stratified Fluid. Part II: Application to Lakes. *J. Phys. Oceanogr.* 21:659–680.
- Imboden, D. and A. Wüest, 1995. Mixing mechanisms in lakes. In: Lerman, A., D. Imboden and J. Gat (eds.), *Physics and chemistry of lakes*, Springer-Verlag, Berlin.
- Lande, R. and M.R. Lewis, 1989. Model of photoadaptation and photosynthesis by algal cells in a turbulent mixed layer. *Deep-Sea Res.* 36:1161–1175.
- Livansky, K., 1995. Influence of mixing on algal photosynthesis in turbulent flow: Modelling approach. *Algol. Stud.* 78:97–109.
- MacIntyre, S., 1993. Vertical mixing in a shallow, eutrophic lake: Possible consequences for the light climate of phytoplankton. *Limnol. Oceanogr.* 38:798–817.

- Marra, J., 1978. Phytoplankton photosynthetic response to vertical movement in a mixed layer. *Mar. Biol.* 46:203–208.
- Moum, J. N., M. C. Gregg, R. C. Lien and M. E. Carr, 1995. Comparison of turbulence kinetic energy dissipation rate estimates from two ocean microstructure profilers. *J. Atmos. Ocean. Techn.* 12:346–366.
- Nixdorf, B., H. Behrendt and W.-G. Pagenkopf, 1992. Diurnal patterns of mixing depth and its influence on primary production in a shallow lake. *Int. Revue. ges. Hydrobiol.* 77:349–360.
- Oakey, N. S., 1982. Determination of the rate of dissipation of turbulent energy from simultaneous temperature and velocity shear microstructure measurements. *J. Phys. Oceanogr.* 12:256–271.
- Osborn, T. R. and C. S. Cox, 1972. Oceanic fine structure. *Geophys. Fluid Dyn.* 3:321–345.
- Pagenkopf, W. G., 1990. Objektivierte Kriterien für die Analyse turbulenter Vertikalvermischung in nichtisothermen Wasserkörpern. *Acta Hydrophys.* 34:45–74.
- Pahl-Wostl, C. and D. M. Imboden, 1990. DYPHORA – a dynamic model für the rate of photosynthesis of algae. *J. Plankton Res.* 12:1207–1221.
- Powell, T. and P. J. Richerson, 1984. The diurnal cycle of stratification in Lake Titicaca: Eddy diffusion. *Verh. Internat. Limnol.* 22:1237–1243.
- Shay, T. J. and M. C. Gregg, 1986. Convectively driven mixing in the upper ocean. *J. Phys. Oceanogr.* 16:1777–1799.
- Tennekes, H. and J. L. Lumley, 1973. *A first course in turbulence*, MIT Press, Cambridge.
- Thorpe, S. A., 1977. Turbulence and mixing in a Scottish Loch. *Phil. Trans. Roy. Soc. London, A.* 286:125–181.
- Wijesekera, H. W. and L. Padman, 1993. Some statistics and dynamical properties of turbulence in the oceanic pycnocline. *J. Geophys. Res.* 98:22665–22679.
- Wüest, A., 1994. Interaktionen in Seen: Die Biologie als Quelle dominanter physikalischer Kräfte. *Limnologica* 24:93–104.
- Yamazaki, H. and D. Kamykowski, 1991. The vertical trajectories of motile phytoplankton in a wind-mixed water column. *Deep-Sea Res.* 38:219–241.

Received 16 December 1996;

revised manuscript accepted 27 October 1997.

Dissipation and mixing in a coastal jet: A Baltic Sea case study

Christoph Zülicke¹, Eberhard Hagen¹ and Adolf Stips²

¹ Baltic Sea Research Institute (IOW), University of Rostock, D-18119 Warnemünde, Germany, e-mail: christoph.zuelicke@io-warnemuende.de; e-mail: eberhard.hagen@io-warnemuende.de

² Space Applications Institute (SAI) at the Joint Research Center (JRC), I-21020 Ispra (VA), Italy; e-mail: adolf.stips@jrc.it

Key words: Dissipation, mixing, turbulence, coastal jet, Baltic Sea.

ABSTRACT

Vertical profiles of dissipation rate are used to study mixing properties within a shallow water region influenced by a coastal jet.

In the upper 10-m layer dissipation rates of the order of $\varepsilon \propto 10^{-6}$ W kg⁻¹ have been measured. Most dissipation results from local production of turbulent kinetic energy, caused by Reynolds-stress in the coastal jet. Some high-energetic turbulent events are not locally balanced and are most probably advected to the measurement site by the coastal jet.

Estimates of the associated eddy diffusivities for locally balanced situations are in the order of $K_p \propto 10^{-4}$ m² s⁻¹. This comparably high value is due to the high level of turbulence throughout the water column and high mixing intensity ($\gamma_{\text{mix}} \approx 0.22$). This feature is clearly related to the coastal jet in its stratified environment.

1. Introduction

Direct measurements of turbulent current fluctuations allow for the estimation of the dissipation rate of turbulent kinetic energy. Such measurements are required to verify parameterizations of diffusivities, which are commonly used in analytical and numerical circulation models within a wide range of applications (Caldwell and Moum, 1995; Gibson, 1990; Gargett, 1989; Gregg, 1987).

Measurements of dissipation rates are reported from several regions, both in the open ocean and in lakes. We mention as examples the Equatorial undercurrent (Peters et al., 1988), open ocean (Toole et al., 1994), the ocean floor (Polzin et al., 1997), tidal front systems (Simpson et al., 1996, Gargett and Moum, 1995), and lakes (Wüest et al., 1996; Imberger and Patterson, 1990). Only a few regional studies were reported for the Baltic Sea (Stips et al., 1998; Lilover and Nabatov, 1990), a semi-enclosed marginal sea, characterized by strong stratification and wind-induced circulation (Rheinheimer, 1996).

Coastal currents result from wind forcing and establish basin-scale gradients in the sea level anomaly (Huthnance, 1978). It is not well documented what happens with respect to mixing in the presence of a coastal jet in such a stratified environment. Such coastal jets transport and transform not only water masses and related thermohaline properties but also turbulence. As a consequence, measured mixing properties will be composed of two components, one locally generated and the other one advected.

This paper aims to elucidate the properties of dissipation and mixing processes in a coastal jet regime by means of observational data. It is structured as follows: The database is introduced in the next section. In section three the average forcing conditions are described, both atmospheric and aquatic. The observed dissipation rate is then discussed in the following section. After that, the eddy diffusivity is estimated and compared with different parameterizations. Finally, a summary is given and the possible direction of future research is described.

2. Database

The data were acquired during a cruise of R/V “Professor Albrecht Penck” in the frame of the Gotland Basin Experiment (GOBEX), which was carried out in the Baltic Sea during 7–17 March 1995. In addition to the standard hydrographic survey, an anchor station “R6B” was performed at the margin of the Arkona Basin for 11 hours on 16 March, 1995 (05:45 ... 16:10 UTC, $t = 74.24 \dots 74.67$ Day of Year 1995 (DOY) or $t = 0.0 \dots 11.0$ h). The station is located Northwest of Rügen Island as indicated in Fig. 1 by a black dot (location 54.40 °N, 13.10 °E; ca. 5 km offshore). The local water depth was $D = 18$ m.

Meteorological standard parameters were continuously recorded using the automatic weather station aboard the ship (DATADIS). Time series of solar radiation were available from the permanent measuring station “DS – Darß Sill”, located approximately 50 km away (indicated in Fig. 1 by a black star). Hourly averaged values of the 2π -integrating pyranometer describe the sky conditions at the station “R6B”.

For dissipation profiling, a microstructure probe (MST) was used as described by Prandke and Stips (1998). The free rising profiler was connected to a bottom mounted underwater winch for repeated profiles starting at least every 15 minutes and covering the water column between about 10 m depth and the sea surface. A total of 82 microstructure profiles was recorded during this 11-h period. The winch was moored about 100 m ahead from the anchored ship. The instrument measured the high-frequency current shear fluctuations and standard hydrographic parameters such as pressure, conductivity and temperature.

In addition, current velocity and direction were recorded by moored Aanderaa current meters (RCM-7) at four selected depths ($z = -4.5, -5.5, -10.5, -15.5$ m). The vertical axis is denoted by z (positive upwards; $z = 0$ at the sea surface).

For further analysis of mesoscale dynamics, the data were merged on a 1 meter/1 hour grid.

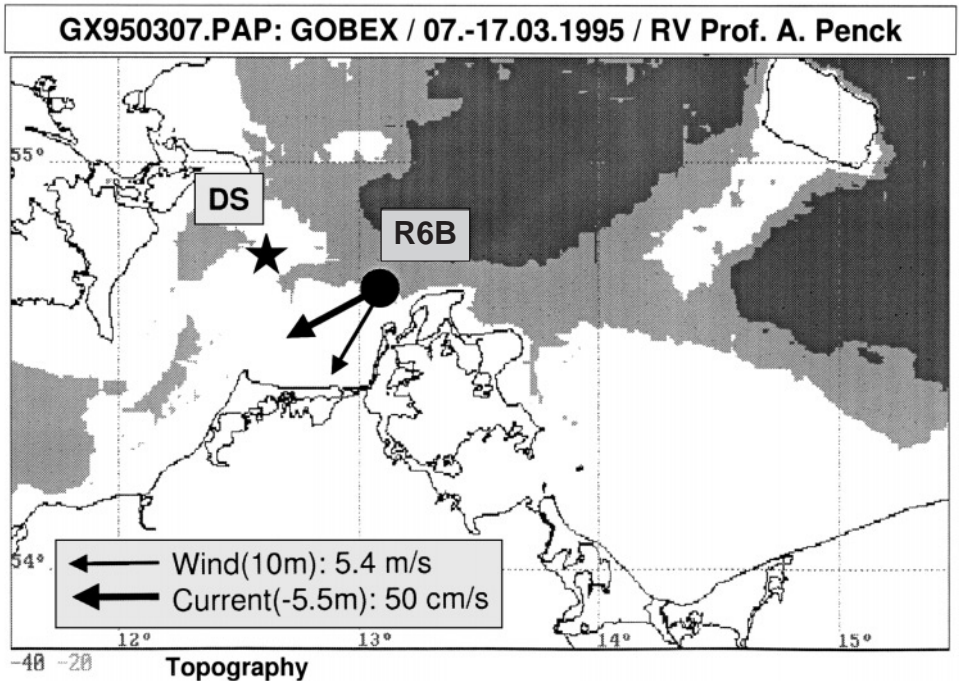


Figure 1. Station map, showing the position of the anchor station (“R6B” – black dot) with vectors of the mean wind velocity ($z = 10$ m) and mean current velocity ($z = -5.5$ m). “DS” (black star) indicates the automated measuring station at the Darß Sill. Grey colors show the 20-m and 40-m isobaths

3. Average forcing conditions

Methodical Aspects

The characteristic scales of the coastal jet are given by the width of the coastal slope region L and the inertial frequency f (Huthnance, 1978). The local Coriolis frequency is $f = 2\omega \sin(\varphi)$, with ω the angular velocity of Earth’s rotation at the latitude φ . The characteristic time scale will be $T_f = 2\pi/f = 14.7$ h, with $f = 1.19 \cdot 10^{-4} \text{ s}^{-1}$ at $\varphi = 54^\circ 24' \text{ N}$. Since the measured time series covers about 75% of T_f , our observations should be interpreted as a snapshot rather than a representative average.

The coastal jet is established by the basin-wide water balance, which is adjusted within of 2–3 days. It is topographically fixed by the shelf width L . Lass and Talpsepp (1993) estimate a typical scale of $L \approx 31.5$ km for the Arkona Basin. This is much more than the first mode baroclinic radius of deformation R_1 , which is $R_1 \approx 4.2$ km. The small stability number $(R_1/L)^2 \approx 0.02$ indicates a stratification-independent current regime. R_1 is also much larger than the distance between MST winch, RCM moorings and ship. Hence, the dissipation, current and hydrographic

measurements are considered to be taken at one location and to be representative of the central part of the coastal jet.

Heat and Salt Balance

The dry air temperature was recorded 10 m above the sea surface, its temporal mean value is $\langle T_{10}(t) \rangle_{\text{ser}} = 2.1 \pm 0.9 \text{ }^\circ\text{C}$. Henceforth the standard deviation will be indicated using the “ \pm ” sign. In the following, all means are calculated from hourly averages in order to construct comparable time series from records with different sampling intervals; the brackets with the subscript “ser” denote the average over the 11-h time series:

$$\langle \dots \rangle_{\text{ser}} = \int_{0\text{h}}^{11\text{h}} \frac{dt}{11\text{h}} \dots \quad (1)$$

Hourly values of $T_{10}(t)$ increased from $1.1 \text{ }^\circ\text{C}$ in the morning to $3.2 \text{ }^\circ\text{C}$ in the late afternoon following the solar heating. The sea surface temperature is $\langle T_0(t) \rangle_{\text{ser}} = 3.1 \pm 0.1 \text{ }^\circ\text{C}$, which showed a weak diurnal variation.

The net heat flux is composed of a surface and a volume part. Associated turbulent fluxes were estimated with bulk formulae recommended by Foken (1990), for the long-wave radiation the formulation proposed by Oberhuber (1988) was applied. We found a mean surface heat flux of $\langle Q_0(t) \rangle_{\text{ser}} = (78 \pm 13) \text{ W m}^{-2}$, directed from the warm sea surface into the cold atmospheric boundary layer. Using separate observations, the short-wave (solar) radiation flux $R_{\text{SW},0}$ was estimated. Its mean value is $\langle R_{\text{SW},0}(t) \rangle_{\text{ser}} = (-168 \pm 86) \text{ W m}^{-2}$. The resulting curves are drawn in Figure 2. In the first hours of observation (just after sunrise) heat loss from the water dominated. Later, decreasing surface heat fluxes Q_0 coincided with increasing solar radiation $R_{\text{SW},0}$, in accordance with the solar cycle. The maximum solar insolation is realized at about 14:00 UTC ($t = 74.58 \text{ DOY}$) with 270 W m^{-2} . For the net heat flux into the bulk of the water we assume that all solar radiation is absorbed in the water volume

$$Q_{\text{bulk}}(t) = Q_0(t) + R_{\text{SW},0}(t) \quad (2)$$

We find an average value of $\langle Q_{\text{bulk}}(t) \rangle_{\text{ser}} = -90 \pm 96 \text{ W m}^{-2}$. A weak net heat gain occurred in the aquatic surface layer during the observational period. This feature is quite characteristic for early spring.

Surface salinity increased slightly due to evaporation of water (no precipitation was observed); the mean was found to be $\langle S_0(t) \rangle_{\text{ser}} = 8.6 \pm 0.1 \text{ PSU}$.

The combined effect of temperature and salt on potential density ρ_p is shown in Figure 3. The overall stratification is stable due to the increasing salinity with depth. The potential density profile appears homogeneous near the surface down to a depth of 3 m. It has a relatively constant gradient between $z = -3 \text{ m}$ and -10 m .

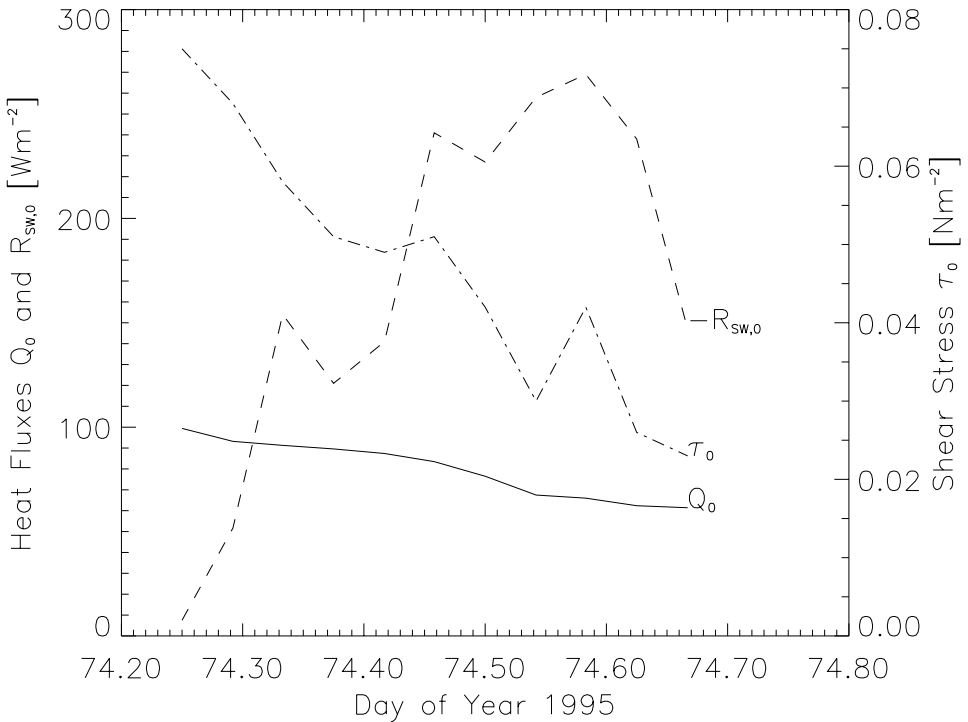


Figure 2. Time series of surface forces. The abscissa follows the time t in Days of the Year 1995 [DOY]. Curves indicate the surface heat flux (Q_0 [W m^{-2}], solid line, left axis), the short wave (solar) radiation flux ($R_{\text{sw},0}$ [W m^{-2}], dashed line, left axis) and the surface shear stress (τ_0 [N m^{-2}], dotted line, right axis)

This is a typical two layer situation: The upper mixed layer ($z = 0 \dots -3 \text{ m}$) will be referred to as “surface”

$$\langle \dots \rangle_{\text{surf}} = \int_{-3 \text{ m}}^0 \frac{dt}{3 \text{ m}} \dots \quad (3-1)$$

and the stratified layer below ($z < -3 \text{ m}$) as “interior”

$$\langle \dots \rangle_{\text{int}} = \int_{-10 \text{ m}}^{-3 \text{ m}} \frac{dz}{7 \text{ m}} \dots \quad (3-2)$$

The average over the 10-m layer ($z = 0 \dots -10 \text{ m}$) will be referred to as “bulk”

$$\langle \dots \rangle_{\text{bulk}} = \int_{-10 \text{ m}}^0 \frac{dz}{10 \text{ m}} \dots \quad (3-3)$$

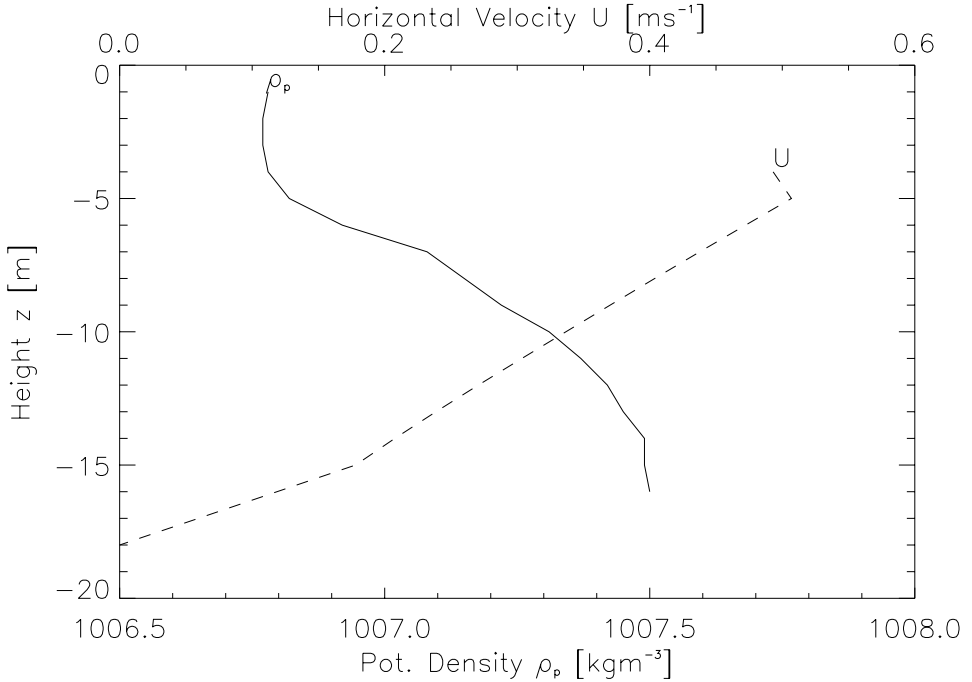


Figure 3. Mean profiles of hydrographic properties. The profiles are showing the potential density (ρ_p [kg m^{-3}], solid line, bottom axis) and the horizontal current velocity (U [m s^{-1}], dashed line, upper axis)

The Brunt-Väisälä frequency N is estimated for each hour-meter sample

$$N^2(t, z) = -\frac{g}{\rho_p} \frac{\partial \rho_p(t, z)}{\partial z} \quad (4)$$

The average over the bulk of the water reveals $\langle N^2(t, z) \rangle_{\text{ser, bulk}} = (7.7 \pm 5.0) 10^{-4} \text{ s}^{-2}$. This quantity has been determined separately for the surface $\langle N^2(t, z) \rangle_{\text{ser, surf}} = (4.3 \pm 4.9) 10^{-5} \text{ s}^{-2}$ and interior layer $\langle N^2(t, z) \rangle_{\text{ser, int}} = (8.9 \pm 4.5) 10^{-4} \text{ s}^{-2}$. The latter is more stratified.

Momentum Balance

Wind data were recorded 10 m above the sea surface. There was a North-North-East wind with a mean speed of $\langle U(t, 10 \text{ m}) \rangle_{\text{ser}} = (5.4 \pm 1.0) \text{ m s}^{-1}$. Its mean vector is plotted in Fig. 1. During the observations the wind speed gradually decreased. The corresponding surface wind-stress (see Fig. 2) is estimated from aerodynamic bulk formulae

$$\tau_0(t) = \rho U_{*0}^2(t) \quad (5)$$

The mean of $\langle \tau_0(t) \rangle_{\text{ser}} = (4.7 \pm 1.6) 10^{-2} \text{ N m}^{-2}$ is associated with a surface friction velocity of $\langle U_{*,0}(t) \rangle_{\text{ser}} = (6.7 \pm 1.2) 10^{-3} \text{ m s}^{-1}$.

According to Lass and Talpsepp (1993), the East component of the wind with a duration of several days causes a coastal jet in the region of the anchor station “R6B”. This current roughly follows the bottom contours of the southern Arkona Basin from East to West (see Fig. 1). In its core region it dominates the whole water column above the shelf-slope zone. The current decreases towards the bottom and is stationary in time.

In order to estimate the local momentum and energy balance, the current profile must be reconstructed from the 4 measurement levels. The current velocity at the bottom is assumed to be zero. Lacking observations of surface drift and wave properties, we reserve special investigation of the surface layer to future studies. The linearly interpolated profile of the flow is shown in Figure 3. The current velocity shows a characteristic decreasing profile – the average value over the water interior is $\langle U(t, z) \rangle_{\text{ser,int}} = 36 \pm 12 \text{ cm s}^{-1}$. The estimated current shear is $\langle (\partial U / \partial z)(t, z) \rangle_{\text{ser,int}} = (3.8 \pm 0.7) 10^{-2} \text{ s}^{-1}$.

Using the linearly interpolated current profile, the bottom shear stress 1 m above the bottom is estimated. With a bottom drag coefficient of $C_{D,\text{bott}}(1.0 \text{ m}) = 2.5 10^{-3}$ (Soulsby, 1983) we find from

$$\tau_{-D}(t) = C_{D,\text{bott}}(1.0 \text{ m}) \rho U^2(t, -D + 1 \text{ m}) = \rho U_{*,-D}^2(t) \quad (6)$$

a bottom shear stress $\langle \tau_{-D}(t) \rangle_{\text{ser}} = (1.3 \pm 0.5) 10^{-2} \text{ N m}^{-2}$ and the corresponding friction velocity $\langle U_{*,-D}(t) \rangle_{\text{ser}} = (3.6 \pm 4.2) 10^{-3} \text{ m s}^{-1}$. The bottom shear stress is 1/4 of the surface value. It is also responsible for the almost permanent current shear through the water column.

Dimensionless characteristics

For the gradient Richardson number

$$\text{Ri}(t, z) = \frac{N^2(t, z)}{(\partial U / \partial z)^2(t, z)} \quad (7)$$

we find $\langle \text{Ri}(t, z) \rangle_{\text{ser,int}} = 0.68 \pm 0.53$. Although the shear is high, it is counterbalanced by strong stratification. The gradient Richardson number Ri is variable – the samples range from 0.07 to 3.11. The measurements covered situations for the onset of shear instabilities. Figure 4 shows the following dynamics of Ri: In the morning the values observed are generally lower than in the afternoon. The uppermost 2–3 meters are almost permanently weakly stratified ($\text{Ri} < 1.0$), possibly due to mixing by winds and waves. After $t = 74.45 \text{ DOY}$ a diurnal thermocline is developing at a depth of about 4–5 meters, associated with larger values of $\text{Ri} > 1.0$.

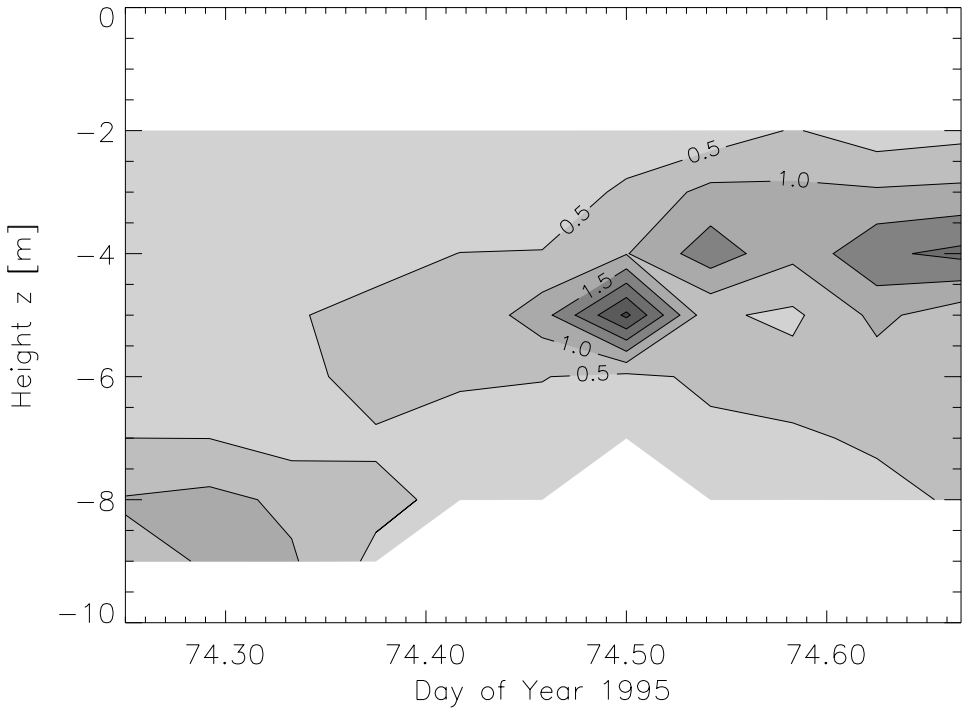


Figure 4. Contour plot of gradient Richardson number (Ri). The contour levels are [0.0, 0.5, 1.0, ...]

4. Dissipation rate

Mean values

Hourly dissipation rates $\epsilon(t, z)$ were measured between $5.6 \cdot 10^{-7}$ and $3.3 \cdot 10^{-5} \text{ W kg}^{-1}$ (or $\text{m}^2 \text{ s}^{-3}$). This range extends over two orders of magnitude. The mean dissipation rates are presented in Table 1.

Intense dissipation rates were observed during two periods within the bulk layer, see Figure 5 for the contour plot. The first period occurred during the first two hours and extends down to 7 m depth with intensities above $10^{-5} \text{ W kg}^{-1}$. It extends over regions where the gradient Richardson number Ri was below 0.5 (compare contour

Table 1. Dissipation rates (ϵ_{bulk} , ϵ_{surf} , ϵ_{int}) of three layers (bulk: $z = 0 \dots -10 \text{ m}$, surface: $z = 0 \dots -3 \text{ m}$ and interior: $z = -3 \dots -10 \text{ m}$) for different observational periods (series: $t = 0 \dots 11 \text{ h}$, stationary: $t = 2 \dots 7 \text{ h}$). The cells contain means with standard deviations.

T [h]	$\epsilon_{\text{bulk}} [10^{-6} \text{ W kg}^{-1}]$	$\epsilon_{\text{surf}} [10^{-6} \text{ W kg}^{-1}]$	$\epsilon_{\text{int}} [10^{-6} \text{ W kg}^{-1}]$
11 (ser)	(3.8 ± 5.9)	(5.4 ± 6.2)	(3.0 ± 5.5)
7 (stat)	(1.4 ± 0.8)	(1.8 ± 1.0)	(1.2 ± 0.6)

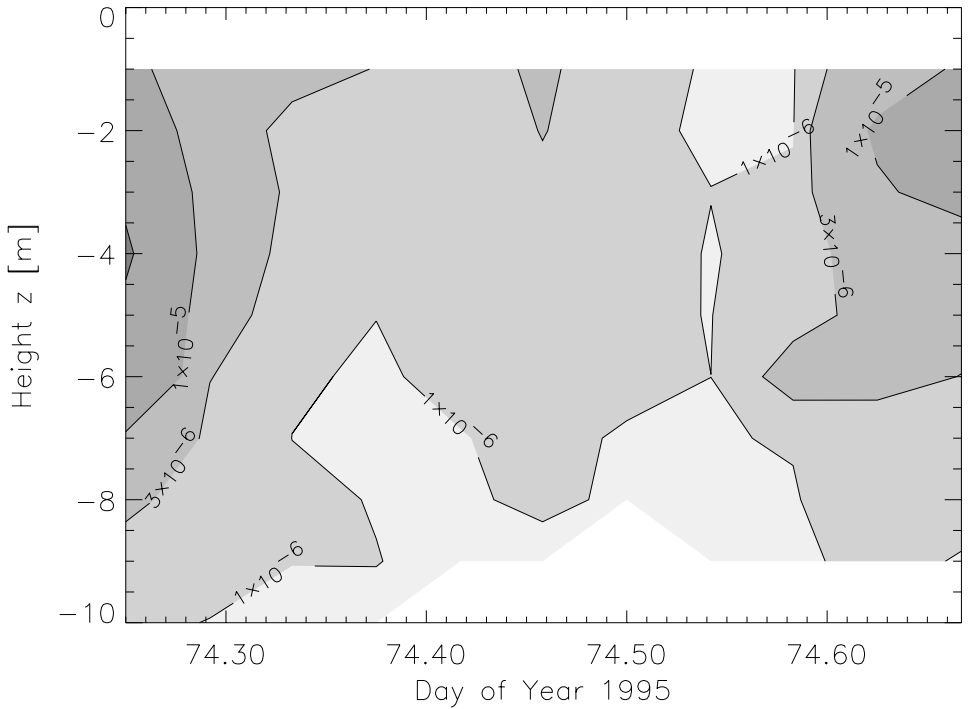


Figure 5. Contour plot of dissipation rate ϵ [W kg^{-1}]. The contour levels are $[0.0, 1.0 \cdot 10^{-6}, 3.0 \cdot 10^{-6}, 1.0 \cdot 10^{-5}, \dots]$ W kg^{-1}

plot of Fig. 4). A less intense event of lower dissipation (about $2.0 \cdot 10^{-6} \text{ W kg}^{-1}$) appeared at about $t = 74.45$ DOY and extended over some meters depth. It is possibly related to a slight increase in wind speed (Fig. 2). Then, increasing stratification suppressed turbulent activities. Later, at $t = 74.55$ DOY the dissipation rate became higher again, with highest values (above $1.0 \cdot 10^{-5} \text{ W kg}^{-1}$ above 3 m depth) located well above the thermocline. Preceding, a slight increase in wind speed was registered.

The observed variance of the dissipation rate is large (see second row of Table 1). Using a t-test for the complete series ($T = 11$ h, effective degree of freedom $N_{\text{eff}}(11 \text{ h}, 10 \text{ m}) = 20$, see Taubenheim (1969)), the 95% confidence range covers $\pm 2.8 \cdot 10^{-6} \text{ W kg}^{-1}$. Thus, the mean value is significantly different from zero, but the precision of the estimate is poor (3/4 of the mean). Hence, it seems to be critical to characterize a mean situation by the values in Table 1. A less variable scene is found in the time period from 74.32 to 74.60 DOY ($T = 7$ h). Related values are given in the third row of Tab. 1; they are denoted with the index “stat” according to

$$\langle \dots \rangle_{\text{stat}} = \int_{2\text{h}}^{9\text{h}} \frac{dt}{7\text{h}} \dots \quad (8)$$

During this phase, the average is reliable with about 1/3 precision on a 95 % significance level ($N_{\text{eff}}(7 \text{ h}, 10 \text{ m}) = 12$). Consequently, this relatively undisturbed period will be referred to as the “stationary phase” of the time series. The mean value for the selected period is about three times less than the energy-rich events at the beginning and at the end of the time series.

The surface value ϵ_{surf} (for $z = 0 \dots -3 \text{ m}$) is slightly larger than the interior value of ϵ_{int} (for $z = -3 \dots -10 \text{ m}$), roughly by a factor of two (see Table 1, third and fourth column). The driving mechanism in the interior of the water is the geostrophic balance, while the surface is additionally subject to direct wind forcing. The order of this contribution can be estimated with $\epsilon_{\text{wind}}(-1 \text{ m}) \propto U_{*,0}^3 (0.4 \cdot 1.0 \text{ m})^{-1} = 7.5 \cdot 10^{-7} \text{ W kg}^{-1}$ and approximately makes up the difference between surface and interior dissipation. More qualified discussion of the impact of winds and waves requires higher vertical resolution of the profiles and additional information on wave statistics (Craig and Banner, 1994; Anis and Moum, 1995).

For comparison with our measurements, other *in situ* observations of turbulence in the Baltic Sea are sparse. Indirect estimates of Kullenberg (1978) using dye tracer techniques were carried out in the Gulf of Bothnia ($61^\circ 13' \text{ N}, 21^\circ 12' \text{ E}$). They show similar results to this study, for a situation with high shear ($\epsilon \approx 9.0 \cdot 10^{-7} \text{ W kg}^{-1}$). Observations of dissipation rates by Lilover and Nabatov (1990) indicate lower values as well ($\epsilon \propto 10^{-9} \dots 10^{-6} \text{ W kg}^{-1}$). We interpret our measurements as indication of strong turbulent activity in the coastal jet.

Characterization of turbulence

To characterize the nature of turbulence, the scheme outlined by Ivey and Imberger (1991) is applied. A characteristic turbulent length scale is estimated from the route mean square Thorpe length L_T . From analysis of the density profiles over 10 m depth we find $\langle L_T(t) \rangle_{\text{ser, bulk}} = (0.09 \pm 0.10) \text{ m}$. The Brunt-Väisälä frequency for this domain is $\langle N \rangle_{\text{ser, bulk}} \approx 2.8 \cdot 10^{-2} \text{ s}^{-1}$, the dissipation rate is $\langle \epsilon \rangle_{\text{ser, bulk}} \approx 3.8 \cdot 10^{-6} \text{ W kg}^{-1}$. The turbulent Froude number (ratio of inertial to gravitational forces) is

$$Fr_t = \left(\frac{\epsilon}{N^3 L_T^2} \right)^{1/3} \tag{9}$$

From our mean values we estimate $\langle Fr_t \rangle_{\text{ser, bulk}} \approx 2.8$. The turbulent Reynolds number (ratio of inertial and frictional forces),

$$Re_t = \left(\frac{\epsilon L_T^4}{\nu^3} \right)^{1/3} \tag{10}$$

is calculated using the kinematic viscosity $\nu = 1.6 \cdot 10^{-6} \text{ m}^2 \text{ s}^{-1}$ – we find $\langle Re_t \rangle_{\text{ser, bulk}} \approx 390$. According to a hydrodynamic phase diagram (Ivey and Imberger, 1991), these numbers indicate active isotropic turbulence for the mean time of observations.

A separate treatment of the “stationary phase” leads to the following picture: From the Thorpe scale $\langle L_T(t) \rangle_{\text{stat, int}} = 0.13 \pm 0.11$ m, dissipation rate $\langle \varepsilon \rangle_{\text{stat, int}} \approx 1.2 \cdot 10^{-6}$ W kg⁻¹ and stability $\langle N \rangle_{\text{stat, int}} \approx 2.9 \cdot 10^{-2}$ s⁻¹ we find $\langle Fr_t \rangle_{\text{stat, int}} \approx 1.4$ and $\langle Re_t \rangle_{\text{stat, int}} \approx 440$. This is the regime of Kelvin-Helmholtz instability, when the buoyancy is important.

Energy balance

The variability of the dissipation rate will be related to that of the local sink/source terms. The observational material allows for a discussion of the interior layer only, because current velocities have not been measured in the layer above 4.5-m depth. The usual stationary local turbulent kinetic energy (TKE) equation for the horizontally homogeneous case is (Osborn, 1980; Gregg, 1987)

$$\varepsilon_{\text{th}}(t, z) = R(t, z) + B(t, z) \quad (11)$$

The dissipation of TKE into heat is balanced by the production of TKE according to mechanical work by Reynolds’ shear stresses (R) and either buoyant TKE production ($B > 0$ for upward buoyancy flux) or reduction ($B < 0$ for downward buoyancy flux).

For the calculation of the Reynolds shear production term

$$R(t, z) = -U_*^2(t, z) \frac{\partial U}{\partial z}(t, z) \quad (12)$$

the shear stress was linearly interpolated from surface (Eq. 5) down to bottom (Eq. 6).

The buoyancy flux B is estimated using the flux Richardson number Rf,

$$B(t, z) = -Rf(t, z) R(t, z) \quad (13)$$

This quantity has not been measured, that’s why we will make use of the Ivey and Imberger (1991) estimate. They introduced the “generalized flux Richardson number Rf’” (ratio of buoyancy flux to the net mechanical energy)

$$Rf' = - \frac{B}{R + \text{other mechanical energy terms}} \quad (14)$$

Only if Eq. 11 holds, the mechanical energy terms beside R are Zero, Rf’ is identical with Rf and can be used in Eq. 13. However, the agreement between theoretical and observed dissipation rate will justify this assumption *a posteriori*. The results can be found in Table 2 and in Figure 6.

Comparing mean values of Table 1 (second column) with those of Table 2 (fourth column), there is a difference of a factor of about two between the complete time

Table 2. Time averaged production R of TKE by Reynolds' stress, buoyancy production B , and corresponding dissipation rates ϵ_{th} using Eq. 11 together with 12 and 13. In the last column, the difference to the observed value $\Delta\epsilon_{th} = \epsilon - \epsilon_{th}$ is listed. $T = 11$ h corresponds to the whole observation time series, while $T = 7$ h selects the “stationary phase”

T [h]	R_{int} [$W\ kg^{-1}$]	B_{int} [$W\ kg^{-1}$]	$\epsilon_{th,int}$ [$W\ kg^{-1}$]	$\Delta\epsilon_{th,int}$ [$W\ kg^{-1}$]
11 (ser)	$(1.2 \pm 0.5) 10^{-6}$	$(0.0 \pm 0.0) 10^{-6}$	$(1.3 \pm 0.6) 10^{-6}$	$(1.6 \pm 5.3) 10^{-6}$
7 (stat)	$(1.2 \pm 0.4) 10^{-6}$	$(0.2 \pm 0.1) 10^{-9}$	$(1.4 \pm 0.4) 10^{-6}$	$(-0.3 \pm 0.6) 10^{-6}$

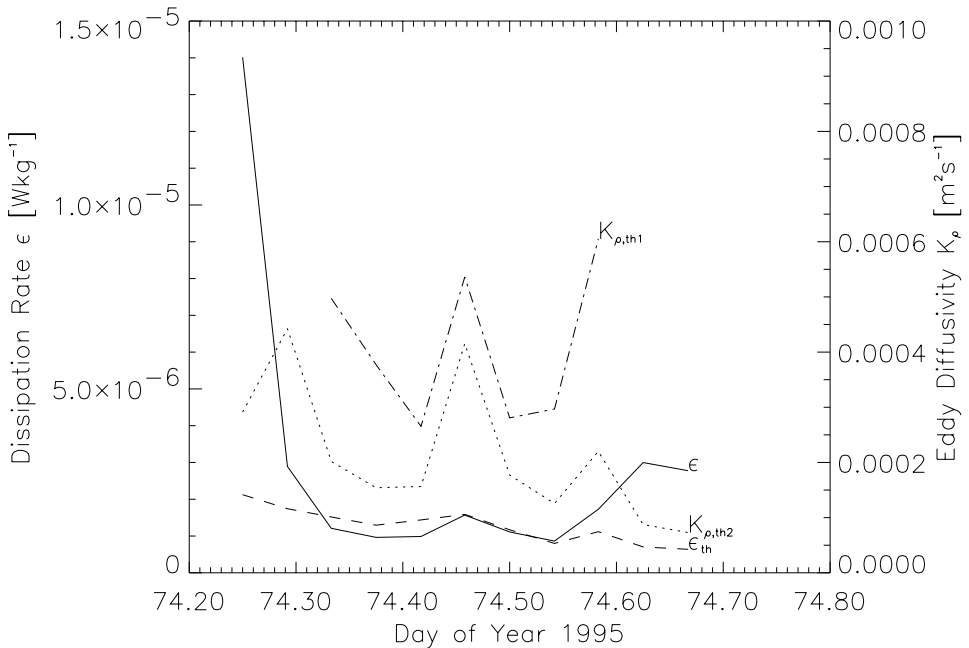


Figure 6. Time series of dissipation and diffusivities. At the left axis is the scale of the observed and theoretical dissipation rate (ϵ [$W\ kg^{-1}$], solid line and ϵ_{th} [$W\ kg^{-1}$] according to Eqs. 11, 12 and 13, dashed line). Superimposed are the estimated diffusivities based on dissipation method according to Eqs. 16 and 17 ($K_{\rho,th1}$ [$m^2\ s^{-1}$], dash-dotted line, right axis), and according to the R-parameterization of Pacanowski et al. (1981) ($K_{\rho,th2}$ [$m^2\ s^{-1}$], dotted line, right axis)

series ($T = 11$ h). From Figures 2 and 6 it could be concluded that during the first two hours the impact of the nighttime cooling is significant. However, the small buoyancy flux B in comparison with the shear contributions R does not allow the enhanced dissipation to be explained in terms of free convection (compare Anis and Moum, 1992). Another large deviation is notable at the end of the time series. Therefore the assumption of a stationary and homogeneous energy balance (Eq. 11) must be considered with some caution for the interpretation of the overall

time series. The fact that the observed dissipation rate exceeds the local TKE balance suggests an advection of turbulence.

During the “stationary phase” ($T = 7$ h) both measured and estimated dissipation rates agree well (see Fig. 6). Their mean squared deviation is much smaller than the natural scatter in the dissipation rate. Production and dissipation of TKE are locally balanced in this case, i.e. Eq. 11 is valid. Only in this situation, Ivey and Imberger’s (1991) generalized flux Richardson number Rf' can be interpreted in the conventional way as Rf (ratio of buoyancy flux to Reynolds production term, Eq. 13). The flux Richardson number turns out to be nearly critical $\langle Rf \rangle_{\text{stat, int}} \approx 0.18$, according to the upper limit suggested by Osborn (1980).

During the “stationary phase” the turbulence is fed by Reynolds shear production R , which is maintained by the coastal jet. The geostrophical forcing includes a certain integral effect in space and time, and has therefore to be distinguished from locally wind-driven regimes. Furthermore, the shallowness of the water makes the impact of bottom friction relevant for the whole water column.

5. Eddy diffusivity

The eddy diffusivity for mixing through density surfaces is defined by the density flux

$$\overline{\rho'w'}(t, z) = -K_\rho(t, z) \frac{\partial \rho}{\partial z}(t, z) \quad (15-1)$$

or equivalently in terms of the buoyancy flux

$$B(t, z) = -K_\rho(t, z) N^2(t, z) \quad (15-2)$$

Because none of the fluxes were measured directly, theoretical assumptions must be made for their estimation.

Dissipation Method

Assuming stationary and homogeneous turbulence, the eddy diffusivity can be related to dissipation rate according to Osborn (1980) as

$$K_{\rho, \text{th1}}(t, z) = \gamma_{\text{mix}}(t, z) \frac{\varepsilon(t, z)}{N^2(t, z)} \quad (16)$$

with the mixing efficiency

$$\gamma_{\text{mix}}(t, z) = \frac{Rf(t, z)}{1 - Rf(t, z)} \quad (17)$$

The dissipation method is applied to the “stationary phase” of our measurements. Making use of the Ivey and Imberger (1991) estimate for the flux Richardson number, we find a mixing efficiency of $\langle \gamma_{\text{mix}} \rangle_{\text{stat, int}} \approx 0.22$. The value of the mixing efficiency γ_{mix} is in the range of Osborn’s (1980) recommendation (see also the review of Gargett and Moun, 1995). Using eq. 16, we get a eddy diffusivity of $\langle K_{\rho, \text{th1}}(t, z) \rangle_{\text{stat, int}} = (4.1 \pm 2.6) 10^{-4} \text{ m}^2 \text{ s}^{-1}$.

Our finding for the diffusivity is now compared with other results. Kullenberg (1978) carried out dye tracer experiments near pycnoclines in the Baltic Proper. They gave values in the order of $10^{-5} \text{ m}^2 \text{ s}^{-1}$. Lilover and Nabatov (1990), quoting $10^{-5} \dots 10^{-4} \text{ m}^2 \text{ s}^{-1}$ in frontal zones, estimated higher values. An interesting investigation was performed by Goudsmit et al. (1997) in comparing mixing coefficients from different parts of Lake Alpnach (Central Switzerland). They found low mixing in the interior of the lake ($K_{\rho} \approx 2.0 \cdot 10^{-7} \text{ m}^2 \text{ s}^{-1}$) and high values near the boundaries ($K_{\rho} \approx 2.0 \cdot 10^{-5} \text{ m}^2 \text{ s}^{-1}$). Our estimate of the eddy diffusivity is larger than most of the other observations. This finding is due to the strong current shear in a stratified environment. Correspondingly, the associated high dissipation rates and buoyancy fluxes lead to high mixing efficiency and diffusivity. We interpret this situation as characteristic for the coastal jet regime, supporting the relevance of boundary mixing.

Richardson-number parameterizations

Finally, the presented eddy diffusion coefficients are discussed in conjunction with typical parameterizations used in circulation models. The parameterization proposed by Pacanowski and Philander (1981), which depends on the gradient Richardson number Ri , is widely applied. For the estimation of the order of magnitude of the eddy diffusivity we adopt their parameterization. The Richardson number dependent average eddy diffusivity $K_{\rho, \text{th2}}$ yield $\langle K_{\rho, \text{th2}}(Ri) \rangle_{\text{stat, int}} = (2.1 \pm 2.7) 10^{-4} \text{ m}^2 \text{ s}^{-1}$ – this is half of our estimate.

Peters (1988) compared diffusivities from the dissipation method in the Equatorial Undercurrent with Pacanowski et al. (1981). Straightforward application of his parameterization leads there to unrealistically high estimates for the diffusivity. The reason is the high sensitivity with respect to low gradient Richardson numbers, which actually ranged within $Ri_{\text{stat, int}} = 0.1 \dots 3.1$. In our case the mean gradient Richardson number of $\langle Ri \rangle_{\text{stat, int}} = 0.68$ would lead to a diffusivity of $1.3 \cdot 10^{-5} \text{ W m}^2 \text{ s}^{-1}$. Our estimate is larger by an order of magnitude. Actually, Peters et al. (1988) has used one average profile over 4.5 days, where the highest mixing efficiency occurred at a depth level of low dissipation rate but high stratification (compare his Figs. 2-g and 12 at $p = 1.1 \text{ MPa}$ level). This is different from our situation with a coastal jet, where we have strong dissipation throughout the water column.

6. Summary and discussion

The almost permanent presence of high dissipation rates can clearly be attributed to the coastal jet. Its powerful geostrophic forcing is an integral effect on the basin

scale, acting with some days duration. Hence, the conditions are distinctly different from local wind-driven situations. Due to the shallowness of water, bottom friction has impact on the whole water column.

The observed level of dissipation rate is relatively high $\varepsilon \propto 10^{-6} \text{ W kg}^{-1}$, compared with other regions of the Baltic Sea. According to Ivey and Imberger (1991), the turbulence is active and isotropic. The coastal jet advects not only thermohaline properties from remote source areas, but also peak values in the dissipation rate. It was possible to estimate the eddy diffusivity for a “stationary period”. With the dissipation method we found values of the order of $K_p \propto 10^{-4} \text{ m}^2 \text{ s}^{-1}$. The efficient mixing ($\gamma_{\text{mix}} \approx 0.22$) is due to the coinciding high shear stress and stratification. With respect to analytical and/or numerical circulation models running in shallow water coastal zones, we conclude that any assumption for constant rates in Richardson-parameterizations must be considered with great caution, especially at the meso-scale. That’s why turbulent quantities should be modeled locally, including production and transport.

Due to a pronounced stratification in the pycnocline and relatively homogeneous wind-stirred surface layers, the Baltic Sea is certainly a good candidate to test different hypotheses concerning vertical fluxes under various conditions. It is proposed that similar future measurements integrate a moored Acoustic Doppler Current Profiler (ADCP) in order to obtain representative values for the vertical current shear over several inertia periods. Further, Laser Doppler Anemometer (LDA) should be applied to measure the high-frequency velocity fluctuations. Such measurements would allow for the direct determination of the turbulent density and buoyancy flux.

ACKNOWLEDGEMENT

We gratefully acknowledge helpful remarks by the anonymous referees and the guest editor Alfred Wüest. A discussion with Thomas Osborn helped to improve the paper. Thanks to Hans-Ulrich Lass for useful remarks on regional oceanography. Ingo Schuffenhauer processed records of the current meters. David Larkin and Rainer Feistel provided valuable assistance with our use of the English. The grant of the “Kultusministerium des Landes Mecklenburg-Vorpommern” No. 0710, MG04, 68101-05 is acknowledged by C. Z. Part of the work was supported by the EC MAST-III project “Baltic Sea System Study (BASYS)”, contract MAS3-CT96-0058. This paper is contribution number 412 of the Baltic Sea Research Institute (IOW), Germany.

REFERENCES

- Anis, A. and J.N. Moum, 1992. A superadiabatic surface layer of the ocean during convection. *J. Phys. Oceanogr.* 22: 1221–1227.
- Anis, A. and J. N. Moum, 1995. Surface Wave – Turbulence Interactions: Scaling $\varepsilon(z)$ near the Sea Surface. *J. Phys. Oceanogr.* 25: 2025–2045.
- Caldwell, D.R. and J.N. Moum, 1995. Turbulence and mixing in the ocean. *Rev. Geophys. Suppl.* 1285–1894 (July 1995). US Nat. Rep. to Int. Union of Geodesy and Geophys. 1991–1994.
- Craig, P.D. and M.L. Banner, 1994. Modeling wave-enhanced turbulence in the ocean surface layer. *J. Phys. Oceanogr.* 24: 2546–2559.
- Foken, Th., 1990. Turbulenter Energieaustausch zwischen Atmosphäre und Unterlage. *Ber. des Dt. Wetterdienstes (Offenbach/Main)* 180 (in German).
- Gargett, A.E., 1989. Ocean turbulence. *Ann. Rev. Fluid Mech.* 21: 419–451.

- Gargett, A.E. and J.N. Moum, 1995. Mixing efficiencies in turbulent tidal fronts: results from direct and indirect measurements of density flux. *J. Phys. Oceanogr.* 25: 2583–2608.
- Gibson, C. H., 1990. Turbulence, mixing and microstructure. In: Le Mehaute and Hanas, Eds.: *The Sea*, Vol. 9, Part A (John Wiley, NY).
- Goudsmit, G.-H., F. Peeters, M. Gloor, and A. Wüest, 1997. Boundary versus internal diapycnal mixing in stratified natural waters. *J. Geophys. Res.* 102: 27, 903–27, 914.
- Gregg, M., 1987. Diapycnal mixing in the thermocline: A review. *J. Geophys. Res.*, 92: 5249–5286.
- Huthnance, J.M., 1978. On coastal trapped waves: Analysis and numerical calculation by inverse iteration. *J. Phys. Oceanogr.* 8: 74–92.
- Imberger, J. and J.C. Patterson, 1990. Physical Limnology. in: Hutchinson, J.W. and T.Y. Wu (Eds.): *Advances in Appl. Mech.* (Acad. Press) vol. 27: 303–475.
- Ivey, G.N. and J. Imberger, 1991. On the nature of turbulence in a stratified fluid. Part I: The energetics of mixing. *J. Phys. Oceanogr.* 21: 650–658.
- Kullenberg, G., 1978. Some observations of vertical mixing conditions in the surface and bottom layers of the Baltic. *Proc. 11. Conf. Baltic Oceanographers*, Rostock, 26.–27.04. 1978, 197–211.
- Lass, H.U. and L. Talpsepp, 1993. Observations of coastal jets in the Southern Baltic. *Continental Shelf Res.*, 13: 189–203.
- Lilover, M.-J. and V.N. Nabatov, 1990. On the turbulent mixing in the frontal zone of the Baltic Sea. In: *Proceedings of the 3-rd All-Union Symposium on Finestructure and Synoptic Variability of the Sea*, Tallinn, 96–97 (in Russian).
- Oberhuber, J.M., 1988. An Atlas based on the COADS data set: The budgets of heat, buoyancy and turbulent kinetic energy at the surface of the global ocean. Max Planck Inst. for Meteorology, Rep. 15.
- Osborn, T., 1980. Estimates of the local rate of vertical diffusion from dissipation measurements. *J. Phys. Oceanogr.* 10: 83–89.
- Pacanowski, R.C. and S.G.H. Philander, 1981. Parameterization of vertical mixing in numerical models of tropical oceans. *J. Phys. Oceanogr.* 11: 1443–1451.
- Peters, H., M.C. Gregg and J.M. Toole, 1988. On the parameterization of Equatorial turbulence. *J. Geophys. Res.* 93: 1199–1218.
- Polzin, K.L., J.M. Toole, J.R. Ledwell and R.W. Schmitt, 1997: Spatial variability of turbulent mixing in the abyssal ocean. *Science* 276: 98–96.
- Prandke, H. and A. Stips, 1992. A model of Baltic thermocline turbulence patches, deduced from experimental investigations. *Continental Shelf Res.* 12: 643–659.
- Prandke, H. and A. Stips, 1998. Test measurements with an operational Microstructure-Turbulence profiler: detection limit of dissipation rates. *Aquatic Sciences*, 60:3, 191–203.
- Rheinheimer, G., 1996. *Meereskunde der Ostsee* (Springer, Berlin) (in German).
- Simpson, J.H., W.R. Crawford, T.P. Rippeth, A.R. Campbell and J.V.S. Cheok, 1996: The vertical structure of turbulent dissipation in shelf seas. *J. Phys. Oceanogr.* 26: 1579–1590.
- Soulsby, R.L., 1983. The bottom boundary layer of shelf seas. in: Jones, B. (Ed.): *Phys. Oceanogr. of Coastal and Shelf Seas*. Elsevier Oceanogr. Ser. vol. 35: 189–266.
- Stips, A., H. Prandke and T. Neumann, 1998. Structure and dynamics of the bottom boundary layer in shallow sea areas without tidal influence: An experimental approach. *Prog. Oceanogr.*, in press.
- Taubenheim, J., 1969. *Statistische Auswertung geophysikalischer und meteorologischer Zeitreihen.* (Geest und Portig, Leipzig) (in German).
- Toole, J.M., K.M. Polzin and R.W. Schmitt, 1994. Estimates of diapycnal mixing in the abyssal ocean. *Science* 264: 1120–1123.
- Wüest, A., D.C. van Senden, J. Imberger, G. Piepke and M. Gloor, 1996: Comparison of diapycnal diffusivities measured by tracer and microstructure techniques. *Dyn. Atmos. Oceans* 24: 27–39.

Received 26 June 1997;

revised manuscript accepted 30 April 1998.

Enhanced mixing in narrows: A case study at the Mainau sill (Lake Constance)

Otti Kocsis, Bruno Mathis, Manuel Gloor, Michael Schurter and Alfred Wüest*

Swiss Federal Institute of Environmental Science and Technology (EAWAG) and
Swiss Federal Institute of Technology (ETH); CH-8600 Dübendorf, Switzerland

Key words: Turbulent mixing, narrows, lake basins, Lake Constance, temperature microstructure, sill, dissipation.

ABSTRACT

Previous work has identified bottom currents as a significant source of turbulence in stratified lakes. Sills may therefore be a major factor determining overall turbulent diapycnal (vertical) exchange in lakes with multi-basin hypolimnia.

In order to investigate the contribution of the Mainau sill (separating Upper Lake Constance from Lake Überlingen) to the overall diapycnal mixing in Lake Constance, a series of temperature microstructure profiles was taken at Mainau Island in October 1993. From these profiles, using Batchelor's method, the rate of dissipation of turbulent kinetic energy was determined and related in an energy balance to the turbulent kinetic energy input from the wind, the energy content of internal seiches and the energy dissipation of bottom currents at the sill. Further, the vertical diffusivities were calculated using the dissipation method.

The analysis shows that $\approx 5.5\%$ of the wind energy flux was found in to the water column (below 2 m depth) and that energy dissipation was 8 times higher in the shear zone of the thermocline ($\approx 8.4 \cdot 10^{-3} \text{ W m}^{-2}$) than in the bottom boundary layer ($\approx 1.1 \cdot 10^{-3} \text{ W m}^{-2}$). Dissipation above the Mainau sill ($\approx 9.5 \cdot 10^{-3} \text{ W m}^{-2}$) exceeded the basin-wide average dissipation of internal seiche energy ($\approx 0.3 \cdot 10^{-3} \text{ W m}^{-2}$) by a factor of 34. However, since the areal extent of the sill is small ($\approx 1\%$ of the lake area), the sill contributes only about 40% to the basin-wide dissipation. Also vertical diffusivities within the thermocline were consistently enhanced by approximately the same amount over the sill. The synthesis of the observations implies that the sill plays a disproportionately large, but not dominant, role for small-scale diapycnal mixing in the hypolimnion of Lake Constance.

Introduction

Many natural aquatic systems are topographically subdivided into different basins. The structure of the narrows connecting such basins has several implications for water exchange and mixing. One prominent phenomenon associated with narrows is locally-enhanced turbulence resulting from intensified currents and shear forces

* Corresponding Author: A. Wüest, EAWAG, 8600 Dübendorf, Switzerland (wuest@eawag.ch)

(e.g. due to tides). A classical example of this is the Strait of Gibraltar (Wesson and Gregg, 1994), where shear forces exceed oceanic background values by orders of magnitude, and where the production of turbulent kinetic energy (TKE) is several orders of magnitude higher than in the open ocean. Other examples are the Strait of Denmark (Oakey and Elliott, 1980), the Strait of Aqaba, the Bosphorus, entries to sounds (Seim and Gregg, 1994), fjords (Stigebrandt, 1989) and estuaries (Peters, 1997).

Sills play a dominant role in enhancing vertical exchange in multi-basin lakes. The most obvious case is that of baroclinic gradients between basins, driving “heavier” water into a basin of “lighter” water. In Lake Lucerne, for example, river input and differential wind forcing have been found to be responsible for inter-basin baroclinic gradients over several sills (Aeschbach-Hertig et al., 1996), leading to significant vertical water exchange between the respective deep hypolimnia (Wüest et al., 1988; Schlatter et al., 1997). In addition, internal seiche pumping (Van Senden and Imboden, 1989) and differential heating (Horsch and Stefan, 1988; Imberger and Patterson, 1989) have been identified as driving mechanisms for vertical exchange. All these processes are moderated by the structure of the sills.

Besides these large-scale displacements of water masses, narrows intensify diapycnal mixing (i.e. mixing perpendicular to density surfaces) locally due to increased internal shear (Peters et al., 1988) and bottom friction (Goudsmit et al., 1997). Sills and narrows are therefore potential sources of diapycnal mixing in stratified natural waters.

Such a situation is found in Lake Constance, at the point where the Mainau sill separates the two main basins, Upper Lake Constance and Lake Überlingen (Fig. 1 and Fig. 1 in Güting and Hutter; this issue). Diapycnal diffusivity in Lake Überlingen, determined during summer stratification at the level of maximum sill depth (≈ 100 m), indeed shows high values of K_z ($= 0.3$ to 1 $\text{cm}^2 \text{s}^{-1}$; Heinz, 1990; Heinz et al., 1990; Maiss et al., 1994). We therefore initiated a case study in order to test the hypothesis that the Mainau sill is 1) the major source of diapycnal exchange and 2) the major sink of kinetic energy. Specifically, we looked for answers to the following questions:

- What is the level of turbulence within the bottom boundary layer at the Mainau sill and how does it compare to the level of turbulence in the thermocline?
- Is the rate of dissipation of TKE within the bottom boundary layer at the sill related to the current speed, and what is the average dissipation during stratification?
- Is the sill responsible for the large background diffusivity which has been observed in the past in the lower thermocline of Lake Überlingen?

In order to answer these questions, we measured 96 temperature microstructure profiles at the sill during a period of five days in October 1993. Based on these data, we inferred TKE dissipation rates and vertical diffusivities, and analyzed wind forcing and bottom currents. After a brief summary of the dynamics at the sill and of the experiment (Section 2), the results are shown in Section 3. The locally measured dissipation is then compared to the rate of decay of the internal seiche energy and to the average annual forcing (Section 4). Finally, conclusions are drawn about the role played by the Mainau sill on the magnitude of the turbulent energy budget and vertical mixing in Lake Constance (Section 5).

Experiment

Dynamics at the Mainau sill

Lake Constance (Fig. 1a), located in Germany, Austria and Switzerland, is the source of drinking water for about 4 million people. The lake, which has a surface area of 535 km² and a volume of 47.6 km³ (water renewal time: 4.1 a), is subdivided into three basins. Whereas Lower Lake Constance is completely separated from the main water body, the sidearm Lake Überlingen (surface area \approx 65 km²) is connected to the main basin of Upper Lake Constance (surface area \approx 407 km²) above the glacial moraine of the Mainau sill (Fig. 1b). The saddle of the sill is 101 m below the lake surface. From this point, the water depth increases to a maximum depth of 147 m in Lake Überlingen and 253 m in Upper Lake Constance (Fig. 1 in Güting and Hutter, this issue).

The seasonal dynamics of the stratification shows features typical of temperate lakes. Convective mixing during the winter period reaches the deepest parts of the lake only sporadically every few years (IGKB, 1989–96). During the period of thermal (and chemical) stratification in summer (April to October), the internal dynamics of the hypolimnion is driven by wind-induced internal seiching, and diapycnal mixing is reduced to weak, small-scale turbulence.

Strong winds, blowing for several hours from one direction, and sporadic storms (occurring typically about once a month and lasting about a day) excite broad-band internal seiches with periods of 3.5 to 5.5 d (Bäuerle, 1981; Schimmele, 1993). Consistent with the first vertical first horizontal mode structure (Bäuerle, 1981 and 1994), and in agreement with the Merian Formula (Lemmin and Mortimer, 1986),

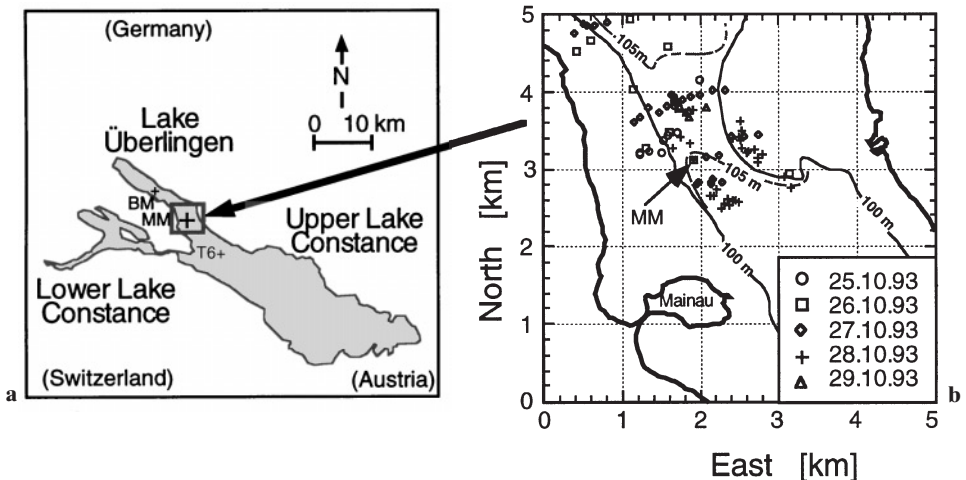


Figure 1. a Map of Lake Constance showing the locations of the moorings BM (thermistor string and wind), MM (current meter) and T6 (wind). A more detailed map is given in IGKB (1990). b The region of the Mainau sill showing the locations of mooring MM and of the microstructure profiles (marked by different symbols each day)

observed seiche periods have been found to be generally shorter during summer and longer in fall (Maiss et al., 1994). Since the wind excitation is irregular, seiching is usually forced and not free oscillations (Schimmele, 1993). Applying a linear model with stratification-dependent eigenfrequencies, Schimmele (1993) was able to reproduce the seiching motion which occurs under irregular wind forcing. The results of his study are representative insofar as the typical wind forcing was close to average (annual average $\approx 2.5 \text{ m s}^{-1}$ at mooring BM, Fig. 1).

In terms of internal seiching, the separation by the Mainau sill is not very distinct, as the sill is much deeper than the thermocline (Fig. 1 in Güting and Hutter, this issue). Consequently, the internal seiches excited in the lake as a whole (Bäuerle, 1981; Zenger, 1989) lead to horizontal currents and high exchange rates between the two basins. Tracer experiments reveal the water residence time-constant to be short; viz. only $80 \pm 10 \text{ d}$ for the entire Lake Überlingen basin (Heinz et al., 1990; Maiss et al., 1994). Due to intensification by the narrowing cross-sectional area of the sill, currents at 80 m depth (20 m above the saddle point) have been observed to show sporadic (approximately monthly) peak values of up to $\approx 20 \text{ cm s}^{-1}$ (Schimmele, 1993; Maiss et al., 1994; Hollan and Simons, 1978). In addition, non-linear internal surges with high current speeds ($> 30 \text{ cm s}^{-1}$) and abrupt changes of direction (Heinz, 1995; Schimmele, 1993) and a low damping time-constant of only $3.1 \pm 0.8 \text{ d}$ (amplitude damping: 6.25 d; Schimmele, 1993) support the working hypothesis of intense mixing at the sill.

Instrumentation

An experiment involving several research institutes was conducted to investigate the internal dynamics in the western part of Lake Constance. The experimental setup, consisting of several thermistor strings and current meters, has been described by Heinz (1995). In this contribution we focus only on the role of the Mainau sill as a sink of internal seiche energy and as a source of diapycnal mixing. In addition to temperature microstructure profiles (locations in Fig. 1 b), the investigation is based on the following mooring data, all sampled at 20 minute intervals:

- Wind speed and direction, measured 4.4 m above the lake surface using an anemometer (Aanderaa Instruments, Bergen, Norway) at moorings BM (Lake Überlingen) and T6 (Upper Lake Constance; Fig. 1a).
- Current speed and direction, measured at 80 m depth above the sill at position MM (Fig. 1a).
- Temperature profiles from 3.4 to 140.5 m depth, continuously measured by two thermistor strings (21 thermistors) moored at BM (Fig. 1a).

Temperature microstructure method

The temperature microstructure method allows profiles of the dissipation of TKE to be determined from well-resolved temperature profiles and also allows vertical diffusivity to be estimated. The method is based on the fact that small-scale temperature fluctuations are always present in natural waters. At the Mainau sill the tem-

perature fluctuations are generated by turbulence due to 1) bottom friction and 2) interior shear of the horizontal velocity of the seiching strata.

The quantitative relationship between the temperature fluctuations on the smallest length scales (mm) – where temperature differences are smoothed by thermal diffusivity κ_T – and the intensity of turbulent mixing is described by Batchelor's (1959) theory. Under isotropic and stationary conditions, the spectrum of one-dimensional temperature fluctuations is described by:

$$\phi_T(k_z) = \frac{\pi \chi \kappa_T^{1/2} q^{3/2} \nu^{3/4}}{\varepsilon^{3/4}} \left(\frac{\exp(-x^2)}{x} - \sqrt{\pi} (1 - \operatorname{erf}(x)) \right) \quad [\text{K}^2(\text{cpm})^{-1}] \quad (1)$$

where k_z [cpm] denotes the vertical wavenumber, $x = k_z \kappa_T^{1/2} \nu^{1/4} q^{1/2} \varepsilon^{-1/4}$ is the non-dimensional vertical wavenumber, ν the kinematic viscosity of water ($1.0 \cdot 10^{-6}$ to $1.5 \cdot 10^{-6} \text{ m}^2 \text{ s}^{-1}$), and $q = 3.4$ the experimentally determined turbulence constant (Dillon and Caldwell, 1980). The rate of dissipation of TKE, ε [W kg^{-1}], and temperature variance χ [$\text{K}^2 \text{ s}^{-1}$] were determined by fitting spectra of the measured temperature profiles to Batchelor's (1959) model spectrum (eq. 1). In other studies, these dissipation estimates have been compared to estimates obtained from the shear dissipation method (Oakey, 1982; Kocsis et al. 1998) and the diffusivity estimates have been compared to diffusivity estimates obtained from tracer studies (Ledwell et al., 1993; Wüest et al., 1996). In both cases agreement was to within a factor of 2.

Temperature microstructure data were measured at 96 Hz using a pair of FP07 fast-response thermistors (response time = $7 \cdot 10^{-3} \text{ s}$; relative resolution 10^{-4} K) mounted on an adapted SBE-9 profiler (SeaBird, Bellevue, Washington, USA; Fig. 2), sinking freely at about 0.1 m s^{-1} down to the lake bottom (as close as $\approx 0.1 \text{ m}$). To reduce the quantization noise of the small temperature fluctuations at small scales, preemphasis (Mudge and Lueck, 1994) was applied by linearly enhancing the microstructure signal as a function of frequency before A/D conversion (details in Gloor et al., 1995). With this arrangement it is possible to resolve dissipation values ranging from 10^{-11} to $10^{-6} \text{ W kg}^{-1}$ within a factor of 2 (see Kocsis et al., 1998 for a detailed analysis of noise levels). The spectra $\phi_T(k_z)$ were calculated from profile segments 1 m in length. Details of the data analysis have been given by Gloor (1995).

In order to obtain statistically robust and easily comparable average estimates, the dissipation profiles $\varepsilon(z)$ were subdivided into an epilimnion layer (the uppermost 20 m), a thermocline layer (20 m below the lake surface to 20 m above the lake bottom) and a bottom layer (0 to 20 m above the lake bottom). The choice of these compartments was guided by the question of the role played by bottom and internal friction in determining overall dissipation in the hypolimnion. Finally, vertical diffusivities were calculated according to the dissipation method using the following expression (Osborn, 1980):

$$K_z = \gamma_{\text{mix}} \varepsilon N^{-2} \quad [\text{m}^2 \text{ s}^{-1}] \quad (2)$$

The stability N^2 was calculated from the temperature profiles. The value $\gamma_{\text{mix}} = 0.12$ was used for the mixing efficiency (Peters and Gregg, 1987) due to the lack of a more appropriate parameterization.

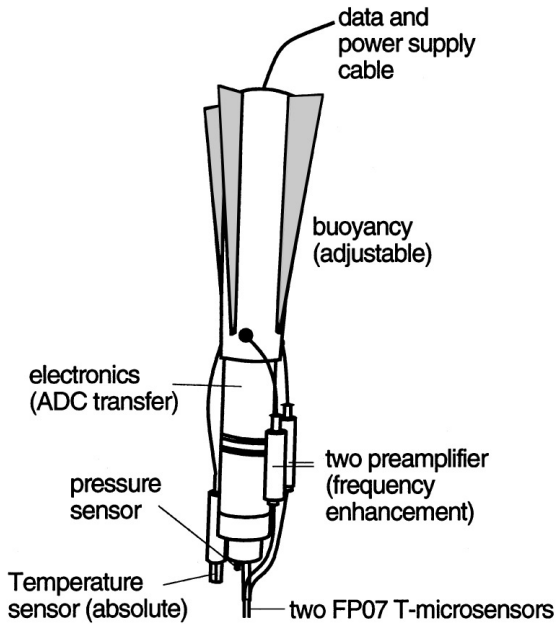


Figure 2. The adapted SeaBird Electronics microstructure profiler used in this study. The sinking speed is adjusted to 10 cm s^{-1} by the buoyancy of the profiler (see Gloor et al., 1995 for technical details)

Observations

Wind and seiching at the Mainau sill

The major overall driving force for vertical mixing during the summer stratification period is wind. Figure 3a shows the wind speed, measured 4.4 m above the lake surface at mooring BM (Fig. 1), during 12 days at the end of October 1993. Since the wind data measured at BM and T6 (Fig. 1) are highly correlated, we consider the record at BM to be representative of the lake as a whole, and calculations of the wind stress exerted on the lake surface are based on this record. At station BM, the average wind speed during the sampling period (Oct. 25 – 29) was $\langle w_{4.4\text{m}} \rangle = 2.95 \pm 0.06 \text{ m s}^{-1}$, while along the axis of the lake it diminished to $\langle w_{4.4\text{m}}(330^\circ) \rangle = 1.30 \pm 0.03 \text{ m s}^{-1}$ ($\langle \rangle$ indicates an average taken over the sampling period). The downward kinetic energy flux E_{10} from the atmosphere 10 m above the lake surface due to a wind speed $w_{10} [\text{m s}^{-1}]$ is given by:

$$E_{10} = \rho_{\text{air}} C_{10} w_{10}^3, \quad [\text{W m}^{-2}] \quad (3)$$

where $\rho_{\text{air}} [\text{kg m}^{-3}]$ denotes the density of air and $C_{10} \approx 10^{-3}$ (Amorocho and de Vries, 1980) the wind drag coefficient. During the experiment, energy input (Fig. 3b) occurred predominantly on two occasions (October 22 and 26/27) from NE winds. Since such winds blow almost perpendicular to the axis of the lake, their efficiency

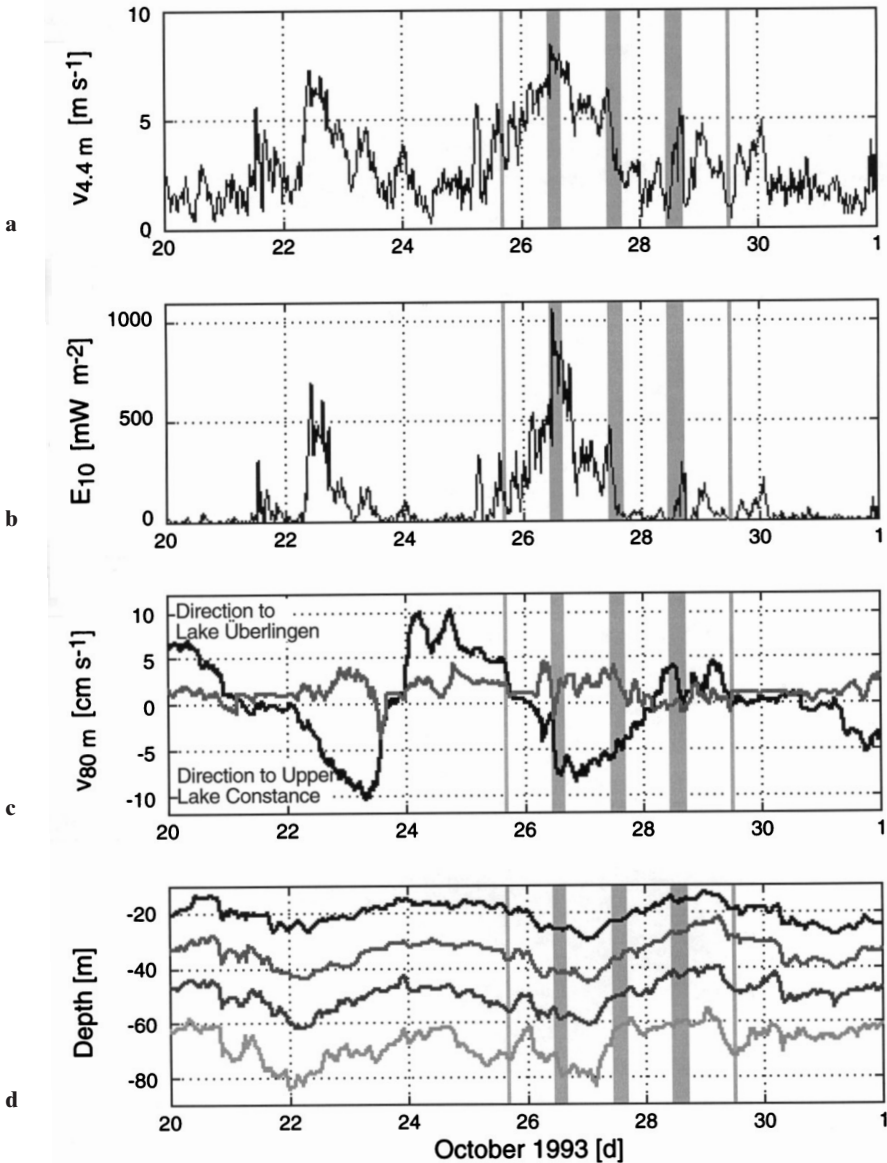


Figure 3. **a** Wind speed 4.4 m above water level at station BM (Fig. 1). The strong winds on October 22 and October 26–27 were from the NE. Microstructure measurements were conducted during the periods shaded. **b** Downward kinetic wind energy flux E_{10} 10 m above the lake surface (eq. 3). **c** Longitudinal (black) and transverse (grey) current velocities at 80 m depth at station MM with 4.6 d seiching period. Positive transverse currents flow towards the NE (60°). **d** Time series of 5°C (lowest line), 5.5°C , 7°C and 10°C (uppermost line) isotherms measured at station BM (Fig. 1)

in exciting internal seiches is likely to have been less than that of the much weaker NW winds on October 24, which blew along the axis of the lake (330°).

The wind-induced currents in 80 m depth, registered at mooring MM (with a lower detection limit of 1 cm s^{-1}), are plotted in Figure 3c. This record reveals the presence of a longitudinal deep-water current with a periodicity of about 4.6 d, in good agreement with the periodicity of the first vertical first horizontal seiche mode (see Section 2a). Two details are worth mentioning here: 1) Such currents lead to typical longitudinal pathways at the sill on the order of $\approx 5 \text{ km}$. The water masses, experiencing potentially intense mixing at the sill, are pushed back and forth over the sill for several cycles before they eventually intrude into one of the two basins. 2) Abrupt changes in the current, such as that observed during the second part of October 23, might be linked to non-linear internal surges, as reported by Heinz (1995).

The isotherm dynamics (Fig. 3d), monitored by the thermistor string at position BM (Fig. 1), supports the interpretation that the observed currents are due to a seiche of the first vertical first horizontal mode. The first mode structure in the vertical is revealed by the in-phase displacements of up to 12 m of the 5°C , 5.5°C , 7°C and 10°C isotherms shown in Figure 3d. However, as winds occur irregularly on the time scale of the seiche periods, seiching is forced (Schimmele, 1993). The lowest isotherm record (5°C), which is closest to the saddle of the sill, contains high-frequency variations, indicating sources of eddies either due to lateral oscillations or to an interaction with the bottom topography (Heinz, 1995; Hollan and Simons, 1978).

Two examples of microstructure profiles

With a view to quantifying mixing at the Mainau sill, we measured 96 microstructure profiles (Mathis, 1996) scattered over the cross-section of the narrows (Fig. 1b) from October 25 to October 29, 1993 (shaded periods in Fig. 3). Most of the data originate from the hypolimnion, especially from the bottom boundary layer, which was expected to be the most turbulent zone. In Figure 4, two examples of microstructure profiles show the characteristics of the stratification and the small-scale variability. The “active” profile was measured on October 26, 1993 during windy conditions ($w_{4.4\text{m}} = 7.7 \text{ m s}^{-1}$), while the “inactive” one was taken during quiet conditions on October 29 ($w_{4.4\text{m}} = 0.8 \text{ m s}^{-1}$). The four panels of Figure 4, showing the profiles of temperature, temperature gradient, dissipation of TKE and dissipation of temperature variance, will be discussed in the following.

The temperature profiles (Fig. 4a) are characteristic for fall, revealing a $\approx 20 \text{ m}$ thick, convectively-mixed surface layer, and a sharp transition between the epilimnion and the thermocline. The lower thermocline, reaching a minimum temperature of 4.6°C , was weakly stratified.

Profiles of the vertical microstructure temperature gradient (Fig. 4b), show strong fluctuations (exceeding 10 K m^{-1}) with a patchy structure due to the intermittent nature of the turbulence. Double-sided fluctuations in the temperature gradient, indicating active turbulence, are weaker on October 29 (low wind) than on October 26 (high wind), especially below 45 m depth. In the upper thermocline, where turbulence is an indirect effect of the wind via seiching, strong temperature fluctuations persist.

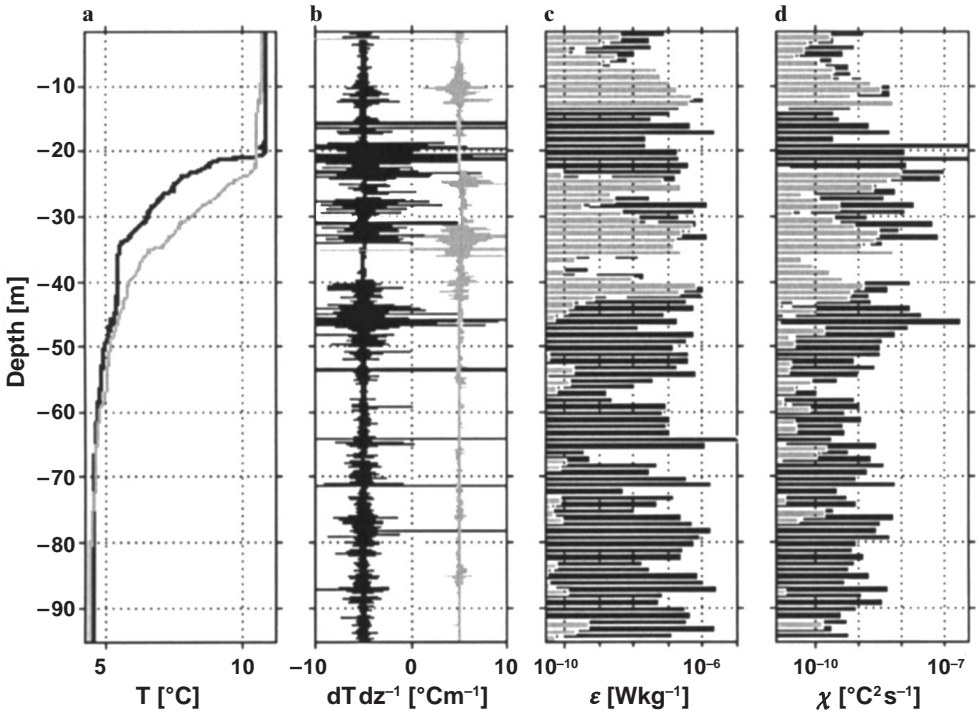


Figure 4. Two examples of microstructure profiles at the Mainau sill, measured during windy conditions (October 26, $w_{4.4m} = 7.7 \text{ m s}^{-1}$; dark) and calm conditions (October 29, $w_{4.4m} = 0.8 \text{ m s}^{-1}$; grey): Temperature **a**, temperature gradient (both profiles offset by 5°C m^{-1}) **b**, dissipation ε of TKE **c** and dissipation χ of temperature variance **d**. Double-sided temperature gradients indicate active turbulence. In zones of strong turbulence, ε and χ are correlated

The two profiles of the dissipation ε (Fig. 4c), determined in vertical bins of 1 m, support this observation quantitatively. During windy conditions, ε is high throughout the entire water column (dark shading) and sporadically reaches values of up to $\varepsilon = 10^{-6} \text{ W kg}^{-1}$. The October 29 profile (light shading) differs distinctly from this, with high dissipation only within the surface layer (the top 13 m) and within two patches of the upper thermocline, whereas the restratifying mixed layer (Brainerd and Gregg, 1995) and the rest of the thermocline are quiet. Neither of the two profiles shows a distinct increase in dissipation towards the bottom.

The profiles of the dissipation of temperature variance χ (Fig. 4d) show the same structure as those of ε : high values of χ throughout the profile on October 26 and the same three major turbulent zones on October 29. The fact that χ is generally decreasing with depth is not only due to the limited invasion of turbulence, but also due to decreasing background temperature gradients (eq. 1) at greater depth.

Due to the characteristic variability of turbulence, both ε and χ are distributed over several orders of magnitude with probability distributions similar to lognormal distributions, when forcing conditions are steady and homogeneous (Baker and

Gibson, 1987; Davis, 1996). Therefore, a large number of estimates is necessary in order to achieve robust ensemble averages. If dissipation follows a lognormal distribution exactly, the maximum likelihood estimate $\langle \varepsilon \rangle_{\text{ML}}$ provides the correct average (Baker and Gibson, 1987), where $\langle \varepsilon \rangle_{\text{ML}} = \varepsilon_0 \langle \exp(\langle \ln(\varepsilon/\varepsilon_0) \rangle + \sigma^2/2) \rangle$ [W kg^{-1}], with the intermittency factor σ^2 (a measure of the degree of intermittency) being given by $\sigma^2 = \langle (\ln(\varepsilon/\varepsilon_0) - \langle \ln(\varepsilon/\varepsilon_0) \rangle)^2 \rangle$ [-], and with the scaling factor $\varepsilon_0 = 1 \text{ W kg}^{-1}$. Especially for small ensembles, this type of average is often more robust than the arithmetic mean.

Compared to oceanic intermittency factors σ^2 , which typically range between 1 and 7 (Baker and Gibson, 1987; Shay and Gregg, 1986; Gregg and Sanford, 1988), in Lake Constance the intermittency in the epilimnion ($\sigma^2 = 4.2$) and in the thermocline ($\sigma^2 = 7.7$) was large. This finding underlines the huge spatial and temporal variability of mixing over the sill.

Energy balance and vertical mixing

To infer the role of the Mainau sill for mixing in Lake Constance we compare the measured dissipation at the sill with the dissipation in the entire lake. In a first step we relate the dissipation of the stratified water column at the sill to the energy input from the wind, to identify the main sinks of energy. In a second step, we compare dissipation at the sill with the basin-wide dissipation inferred from the decay of internal seiches.

TKE fluxes and sinks at the Mainau sill

Based on the dissipation profiles discussed in Section 3, we determined the sink of TKE in the water column at the sill by calculating the energy dissipation per unit area for the three compartments epilimnion, thermocline and bottom layer, by integrating vertically as follows:

$$P_{\text{Comp}}([a,b]) = \int_a^b \rho(z) \langle \varepsilon \rangle_{\text{ML}}(z) dz \approx \rho \int_a^b \langle \varepsilon \rangle_{\text{ML}}(z) dz, \quad [\text{W m}^{-2}] \quad (4)$$

where a, b are the lower and upper bounds of the three compartments and $\langle \varepsilon \rangle_{\text{ML}}(z)$ stands for the daily maximum likelihood estimates over the 1 m bins. While the scatter of the individual dissipation values ε is dominated by intermittency, the uncertainties in P_{Comp} are due rather to systematic errors (calibration, model assumptions, etc.) of a factor of ≈ 2 (Kocsis et al., 1998).

The integrated dissipation estimates P_{Comp} are plotted together with the wind energy flux E_{10} in Figure 5. From the daily mean P_{Comp} we determine the averages for the entire sampling period October 25 to 29 (again indicated by $\langle \rangle$). The averaged vertical wind energy flux was $\langle E_{10} \rangle = 0.22 (\pm 0.13) \text{ W m}^{-2}$. The large standard deviation (in parentheses) is the result of the high degree of variability prevailing during the sampling period and is not due to measurement errors ($< 5\%$). Dissipation in the epilimnion $\langle P_{\text{epi}} \rangle = 2.6 \cdot 10^{-3} (\pm 1.3 \cdot 10^{-3}) \text{ W m}^{-2}$, induced directly by the wind, is strongly correlated to wind and subsequently has a similar variability

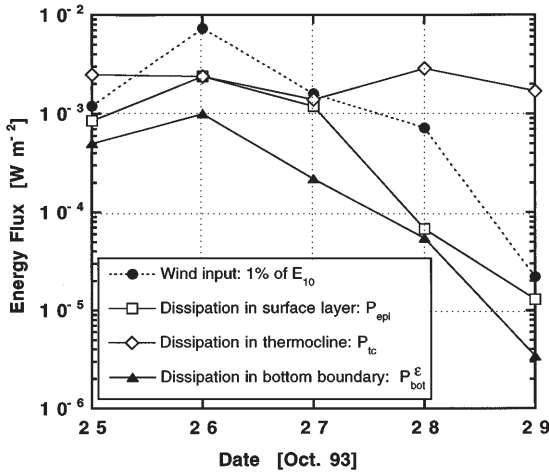


Figure 5. Daily averages of wind forcing and dissipation (eq. 4) in the epilimnion, P_{epi} (0 to 20 m depth); in the thermocline, P_{tc} (20–60 m depth) and in the bottom layer: P_{bot}^E (0 to 20 m above bottom). For presentation reasons, 1% of E_{10} (eq. 3) is plotted. While dissipation in the epilimnion and in the bottom boundary layer is strongly correlated with the wind energy flux, dissipation in the thermocline is nearly constant

ty as wind speed (Fig. 5). Interestingly, dissipation in the bottom boundary ($\langle P_{bot}^E \rangle = 1.0 \cdot 10^{-3} (\pm 0.5 \cdot 10^{-3}) W m^{-2}$) is also similarly correlated to the wind (Fig. 6), whereas dissipation within the thermocline ($\langle P_{tc} \rangle = 8.4 \cdot 10^{-3} (\pm 1.1 \cdot 10^{-3}) W m^{-2}$) is seen to be nearly constant throughout the measurement period (Fig. 5).

Relating the daily averages of the integrated dissipation to the wind energy flux E_{10} and averaging over the sampling period shows that $\approx 14\%$ of E_{10} was dissipated in the epilimnion ($\langle P_{epi} / E_{10} \rangle = 14 (\pm 3.5)\%$), whereas only 3% of E_{10} was lost within the bottom boundary layer ($\langle P_{bot}^E / E_{10} \rangle = 2.9 (\pm 0.9)\%$), but 38% of E_{10} was dissipated in the thermocline ($\langle P_{tc} \rangle / \langle E_{10} \rangle = 38 (\pm 24)\%$). All together, 5.5% of the wind energy E_{10} was dissipated below 2 m water depth at the sill, which is more than the typical energy input into naturally stratified waters (Denman and Miyake, 1973; Wüest et al., 1998 in prep.). A first comparison between thermocline and bottom boundary reveals that the volume-specific and area-specific dissipation in the interior of the thermocline were 2.7 and 8 times stronger, respectively, than within the bottom boundary layer.

For the sake of consistency, we estimate dissipation within the bottom boundary layer due to bottom friction assuming the law of the wall for the horizontal current u_{20} , measured 20 m above bottom at MM (Fig. 1a). A first order approximation for the corresponding vertical kinetic energy flux is given by:

$$P_{bot}^u = \tau_0 u_{20} = \rho_w C_{20} u_{20}^3 = 1.1 \cdot 10^{-4} (\pm 0.51 \cdot 10^{-4}), \quad [W m^{-2}] \quad (5)$$

where τ_0 indicates the stress and $C_{20} = 0.9 \cdot 10^{-3} [-]$ the drag coefficient, a value calculated from Elliott (1984) with a roughness length $z_0 = 10^{-4}$ m. A comparison of this energy loss ($\langle P_{bot}^u \rangle$) with the dissipation ($\langle P_{bot}^E \rangle$) measured using the microstructure

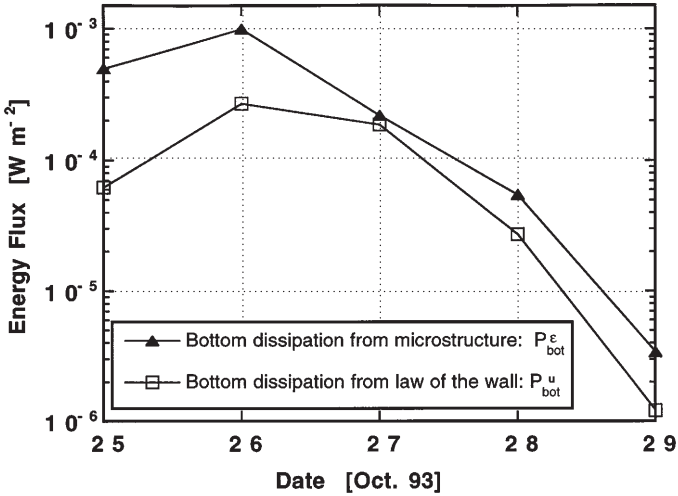


Figure 6. Comparison of the dissipation of TKE in the bottom layer P_{bot}^{ϵ} (0.1 to 20 m above bottom, eq. 4) based on microstructure data, and P_{bot}^u (0 to 20 m above bottom) calculated from current measurements (according to the law of the wall, eq. 5). About half the bottom dissipation is caused by smooth-flow bottom friction

technique (Fig. 6) shows that only about 10% of the turbulent dissipation in the bottom boundary layer was caused by smooth-flow bottom friction ($\langle P_{bot}^u / P_{bot}^{\epsilon} \rangle = 15 (\pm 10)\%$), while – other processes contribute to the production of TKE, for instance instabilities due to non-linearities in internal seiches, the breaking of internal waves (Gargett and Holloway, 1984) and the generation of eddies at topographic features. These additional sources might hide the typical $1/z$ dependence of dissipation as expected for a classical boundary layer. The comparison of P_{bot}^u with P_{bot}^{ϵ} indicates that dissipation within the 10 cm above the lake bottom which were not measured by the microstructure profiler contributes less than 5% to P_{bot}^{ϵ} (assuming a viscous sublayer 1 cm thick).

We conclude that even if dissipation within the bottom boundary layer was larger than expected by smooth-flow bottom friction alone, the bottom boundary layer at the Mainau sill was not the major sink of the local TKE. The comparison of the dissipation in the three compartments shows that the major part of the energy input of the wind into the water column was transferred to the seiching motion.

Relevance of the Mainau sill for dissipation in Lake Constance

To assess the relevance of the Mainau sill as a sink of energy for the whole lake, we relate the dissipation at the sill to the average rate of decay of energy contained in the seiching motions. Here we do not consider the epilimnion, which is directly forced by the wind and which is not significantly influenced by the underwater sill. Consequently we use $\langle \epsilon_{sill} \rangle = \langle P_{tc} \rangle + \langle P_{bot}^{\epsilon} \rangle = 9.5 \cdot 10^{-3} W m^{-2}$ as an estimate for the dissipation caused by seiching in the hypolimnion at the sill. The average rate of

decay of the seiche energy $\langle \epsilon_{IS} \rangle$ is assessed from the internal energy of the seiches, estimated as $2 \cdot \langle E_{Pot} \rangle$, i. e. twice the average potential energy of the seiche, and from the decay time scale of the internal seiches, $\tau_{IS} = 3.1 \pm 0.8$ d, as given by Schimmele (1993). The expected basin-wide dissipation due to internal seiching is then given by $\langle \epsilon_{IS} \rangle = 2 \langle E_{Pot} \rangle / \tau_{IS}$. The potential energy $\langle E_{Pot} \rangle$ is calculated from the local potential energy $E_{Pot}(\text{BM})$ by using the temperature profiles measured at mooring BM:

$$E_{Pot}(\text{BM}, t) = g \int_{\text{bottom}}^{\text{surface}} dz [\rho(z, t) - \bar{\rho}(z, t)] \delta z(z, t), \quad [\text{J m}^{-2}] \quad (6)$$

where $\delta z(z, t) = \frac{T(z, t) - \bar{T}(z, t)}{\partial \bar{T} / \partial z}$ is the vertical displacement of the water parcel from its equilibrium position and $\bar{T}(z, t)$ and $\bar{\rho}(z, t)$ are the water temperature and density (calculated from temperature), respectively, averaged over 6 d. The average potential energy at BM was $\langle E_{Pot}(\text{BM}) \rangle = 142 \pm 8 \text{ J m}^{-2}$. From this local value at BM, the basin-wide potential energy $\langle E_{Pot} \rangle$ was extrapolated by integrating over the volume V of the lake with the amplitude of the internal seiche $\delta z_{\max}(x)$ and the cross section $A(x)$ along the thalweg x (Zenger et al., 1990):

$$\langle E_{Pot} \rangle = \langle E_{Pot}(\text{BM}) \rangle \frac{1}{V} \int_{\text{thalweg}} dx \left(\frac{\delta z_{\max}(x)}{\delta z_{\max}(\text{BM})} \right)^2 A(x) = 37 \text{ J m}^{-2} \quad (7)$$

This value for the basin-wide potential energy $\langle E_{Pot} \rangle$, combined with the decay time scale of the internal seiches τ_{IS} , implies a rate of decay of seiche energy $\langle \epsilon_{IS} \rangle = 2 \langle E_{Pot} \rangle / \tau_{IS} = 0.28 \cdot 10^{-3} \text{ W m}^{-2}$ which is 34 times less than the dissipation $\langle \epsilon_{sill} \rangle$ over the sill. To infer the overall role of the Mainau sill, we compare the dissipation over its area ($A_{\text{sill}} \approx 6 \text{ km}^2$) to the internal seiche dissipation over the entire area of Lake Constance ($A_{\text{Lake}} = 472 \text{ km}^2$):

$$\frac{\langle \epsilon_{sill} \rangle \cdot A_{\text{sill}}}{\langle \epsilon_{IS} \rangle \cdot A_{\text{Lake}}} \approx 0.43 \quad [-] \quad (8)$$

This ratio has an uncertainty factor of ≈ 3 due to the dissipation rate at the sill (factor ≈ 2), the estimate of the potential energy $\langle E_{Pot} \rangle$ (factor ≈ 1.5) and the surface area of the sill A_{sill} (factor ≈ 1.5). In order to reduce this uncertainty, the average dissipation rate $\langle \epsilon_{IS} \rangle$ and the extent of the sill, especially with respect to jets (Hollan and Simons, 1978; Heinz, 1995) and hydraulic jumps, should be determined experimentally.

Vertical diffusivity

Using the temperature profiles, the stability N^2 was calculated. Combined with the dissipation profiles, the vertical diffusivity K_z was estimated by applying eq. (2) and using a mixing efficiency of $\gamma_{\text{mix}} = 0.12$. The daily averages of vertical diffusivity in the thermocline, calculated over the 20 m to 60 m depth range, were $K_z = 1.4, 49,$

2.8, 5.2 and 4.9 $\text{cm}^2 \text{s}^{-1}$ for each of the 5 days from October 25 to October 29. Average thermocline K_z over the measurement period was $\langle K_z \rangle = 13 \text{ cm}^2 \text{s}^{-1}$.

Considering turbulence within the bottom boundary layer, we can expect a comparable contribution to vertical diffusivity. Taking into account the residual stratification within the well-mixed bottom boundary layer, typically a chemical stratification with $N^2 = 7 \cdot 10^{-7} \text{ s}^{-2}$ (Maiss, pers. comm.), and using the reduced effectiveness of well-mixed layers ($\gamma_{\text{mix}} \approx 0.01$; Wüest and Gloor, 1998), a value of $\langle K_z \rangle = 7.5 \text{ cm}^2 \text{s}^{-1}$ would result.

Using SF_6 as a tracer in Lake Überlingen in fall 1990, Maiss et al. (1994) found vertical diffusivities in the same depth range (20 to 60 m) of $K_z = 0.38 \text{ cm}^2 \text{s}^{-1}$ at station BM (Fig. 1) and $K_z = 0.55 \text{ cm}^2 \text{s}^{-1}$ 2.5 km NW of the position of the micro-structure profiles. Even though the increase towards the sill (by a factor of 1.4) is not very significant, these estimates are consistent with the conclusion that both dissipation and vertical diffusivity at the sill are enhanced coherently by one order of magnitude relative to open-water estimates.

Long-term mixing

To scale our observations to basin-wide diapycnal mixing representative of the entire stratification period in Lake Constance, we compared wind and current measured at the sill to their respective averages over the entire stratification period. During the sampling period, the average wind speed $\langle w_{4.4\text{m}} \rangle = 2.95 \text{ m s}^{-1}$ was only slightly higher than the annual average ($\langle w_{4.4\text{m}} \rangle_{\text{annual}} \approx 2.5 \text{ m s}^{-1}$) and blew most of the time from the NE. Only 1/3 of the annual winds ($> 3 \text{ m s}^{-1}$) blow from $60^\circ \pm 20^\circ$ (NE) and 2/3 from WSW ($260^\circ \pm 40^\circ$), perpendicular to the axis of the lake (330° ; Schimmele, 1993). Although observed winds during the sampling period were mainly transverse, and therefore inefficient for exciting internal seiches (E. Bäuerle, pers. comm.), seiche amplitudes (Fig. 3) were of typical size ($\approx 10 \text{ m}$; Schimmele, 1993). In addition, the observed bottom currents at the sill ($\langle |u_{20}| \rangle = 3.6 \text{ cm s}^{-1}$) were slightly stronger than the mean value during the entire stratification period ($\langle |u_{20}| \rangle = 2.6 \text{ cm s}^{-1}$ (11.4–24.10.1993) and the annual average over 5 a ($\langle |u_{20}| \rangle = 2.3 \text{ cm s}^{-1}$ (J. Ilmberger, pers. comm.).

Summarizing this comparison, we can conclude that the sampling period of October 25–29, 1993, can be considered typical for the entire stratification period in terms of wind input and internal seiche excitation. Wind, internal seiche amplitudes and currents at the sill were only slightly, but coherently, enhanced during the five days of observation. Since the effect of the sill increases with the degree of internal seiche excitation, we can conclude that the contribution of the sill to the basin-wide vertical mixing rate, expressed by eq. (8), while representative for the entire stratification period, is rather an upper limit. However the role of non-linear internal surges has not been specifically considered.

Concluding summary

The effect of the Mainau sill on the diapycnal component of vertical mixing in Lake Constance was investigated during the stratification period. Based on 96 tempera-

ture microstructure profiles measured during five days in October 1993, vertical profiles of TKE dissipation were calculated by applying the Batchelor method. Long-term observations of wind, internal seiche displacements (determined from thermistor strings) and bottom currents at the sill allowed TKE budgets to be calculated for the entire hypolimnion and for the stratified part at the sill.

Of the total wind energy flux E_{10} (10 m above the lake surface), 5.5% was dissipated below 2 m depth at the sill. This rudimentary comparison indicates that turbulence at the Mainau sill was not drastically higher than that found in other natural water bodies. Dissipation was highly correlated with E_{10} in the epilimnion ($\approx 0.014 \cdot E_{10}$) and in the bottom boundary layer ($\approx 0.003 \cdot E_{10}$), but dissipation in the thermocline was not directly correlated with the wind input, reflecting rather the background excitation of the internal seiches.

The major energy sink was the thermocline ($8.4 \cdot 10^{-3} \text{ W m}^{-2}$). Dissipation there was 8 times as much as in the bottom boundary layer, which is consistent with the analysis of Zenger (1989) based on the assumptions of Spigel and Imberger (1980). The thermocline is thus a large energy sink, comparable to the ocean thermocline: Gregg and Sanford (1989), for instance, found dissipation between 10 m and 1 km depth in the North Pacific to be $4.8 \cdot 10^{-3} \text{ W m}^{-2}$.

Extrapolation of this energy balance at the Mainau sill to the entire lake reveals that damping of the internal seiche over the sill ($9.5 \cdot 10^{-3} \text{ W m}^{-2}$) was 34 times stronger than the basin-wide average ($0.28 \cdot 10^{-3} \text{ W m}^{-2}$). Diapycnal diffusivity in the thermocline above the sill was enhanced by a similar factor. Since the sill occupies less than 1.5% of the area of the lake, the sill contributed about 43% to both the dissipation of the internal seiche and to the basin-wide vertical diffusivity. The sill therefore plays a disproportionately large role for small-scale diapycnal mixing in the hypolimnion of Lake Constance.

Compared to turbulence at the sill, turbulence within the bottom boundary layer made only a minor contribution to the overall dissipation. Since the mixing effectiveness of already well-mixed water is low, we conclude that bottom boundary mixing at the sill is not responsible for the high diapycnal diffusivity found in Lake Constance. The most plausible new hypothesis – based on this analysis – is that turbulence and mixing in the entire hypolimnion of Lake Überlingen, rather than only at the Mainau sill, is responsible for the intense diapycnal mixing in Lake Constance.

ACKNOWLEDGMENTS

Special thanks go to H. Güde and H. Müller of the Institut für Seenforschung in Langenargen, Germany, for providing the research vessel FS Tinca and for making the collection of field data possible. We also thank G. Heinz, J. Imberger and D. Ollinger for permission to use the wind, current and thermistor-chain data. Useful and constructive comments for improving the manuscript were given by an anonymous reviewer, E. Bäuerle, G. Goudsmit, E. Hollan, M. Maiss and M. Schimmele. We are also in debt to D. M. Livingstone for improving the English. This study was supported by Swiss National Science Foundation grants 20-36364.92 and 20-43357-95 and by the Deutsche Forschungsgemeinschaft within the framework of the Special Collaborative Program “Cycling of matter in Lake Constance” (SFB 248).

REFERENCES

- Aeschbach-Hertig, W., R. Kipfer, M. Hofer, D.M. Imboden and H. Baur, 1996. Density-driven exchange between the basins of Lake Lucerne (Switzerland) traced using the ^3H - ^3He method. *Limnol. Oceanogr.* 41: 707–721.
- Amoroch, J. and J.J. de Vries, 1980. A new evaluation of the wind stress coefficient over water surfaces. *J. Geophys. Res.* 85: 433–442.
- Baker, M.A. and C.H. Gibson, 1987. Sampling turbulence in the stratified ocean: Statistical consequences of strong intermittency. *J. Phys. Oceanogr.* 17: 1817–1836.
- Batchelor, G.K., 1959. Small-scale variation of convected quantities like temperature in turbulent fluid. Part 1. General discussion and the case of small conductivity. *J. Fluid. Mech.* 5: 113–133.
- Bäuerle, E., 1981. Die Eigenschwingungen abgeschlossener, zweigeschichteter Wasserbecken bei variabler Bodentopographie. *Ber. Inst. Meereskunde, Kiel*, No. 85.
- Bäuerle, E., 1994. Transverse baroclinic oscillations in Lake Überlingen. *Aquat. Sci.* 56: 145–160.
- Brainerd, K.E. and M.C. Gregg, 1995. Surface mixed and mixing layer depths. *Deep-Sea Res.* 42: 1521–1543.
- Davis, R.E., 1996. Sampling turbulent dissipation. *J. Phys. Oceanogr.* 26: 341–358.
- Denman, K.L. and M. Miyake, 1973. Upper layer modification at Ocean Station Papa: observations and simulations. *J. Phys. Oceanogr.* 3: 185–196.
- Dillon, T.M. and D.R. Caldwell, 1980. The Batchelor spectrum and dissipation in the upper ocean. *J. Geophys. Res.* 85: 1910–1916.
- Elliott, A.J., 1984. Measurements of the turbulence in an abyssal boundary layer. *J. Phys. Oceanogr.* 14: 1778–1786.
- Gargett, A. and G. Holloway, 1984. Dissipation and diffusion by internal wave breaking. *J. Mar. Res.* 42: 15–27.
- Gloor, M., 1995. Methode der Temperaturmikrostrukturen und deren Anwendung auf die Bodengrenzschicht in geschichteten Wasserkörpern. Ph.D. diss. no. 11336, Swiss Fed. Inst. Technol. (ETH), 159 pp.
- Gloor, M., O. Kocsis, M. Omlin, M. Schurter and A. Wüest, 1995. Temperaturmikrostrukturen, eine Methode zur Bestimmung der Mischungsintensität in geschichteten Gewässern. *Gas Wasser Abwasser* 75: 1087–1096.
- Goudsmit, G.H., F. Peeters, M. Gloor and A. Wüest, 1997. Boundary versus internal diapycnal mixing in stratified waters. *J. Geophys. Res.* 102:27'903–27'914.
- Gregg, M.C. and T.B. Sanford, 1988. The dependence of turbulent dissipation on stratification in a diffusively stratified thermocline. *J. Geophys. Res.* 93: 12381–12392.
- Heinz, G., 1990. Mischungs- und Strömungsverhältnisse im Westteil des Bodensees. Ph.D. diss., Inst. Umweltphysik, Univ. Heidelberg, 146 pp.
- Heinz, G., J. Ilmberger and M. Schimmele, 1990. Vertical mixing in Überlingersee, western part of Lake Constance. *Aquat. Sci.* 52: 256–268.
- Heinz, G., 1995. Strömungen im Bodensee – Ergebnisse einer Messkampagne im Herbst 1993. Mitt. Versuchsanstalt für Wasserbau, Hydrologie und Glaziologie, Swiss Fed. Inst. Technol., Report No. 135.
- Hollan, E. and T.J. Simons, 1978. Wind-induced changes of temperature and currents in Lake Constance. *Arch. Met. Geoph. Biokl. Ser. A.* 27: 333–373.
- Horsch, G.M. and H.G. Stefan, 1988. Convective circulation in littoral water due to surface cooling. *Limnol. Oceanogr.* 33: 1068–1083.
- IGKB (Internationale Gewässerschutzkommission für den Bodensee), 1989–96 Limnologischer Zustand des Bodensees. *Ann. Reports.*
- IGKB (Internationale Gewässerschutzkommission für den Bodensee), 1990. Karte der internationalen Bodenseetiefenvermessung, 1:50000; E0852'–E0946'/N4750'–N4728'. Landesvermessungsamt Baden-Württemberg, Stuttgart.
- Ilmberger, J. and J.C. Patterson, 1989. Physical Limnology. In: “Advances in applied mechanics.”, Academic Press, Cambridge, pp. 303–475.
- Kocsis, O., H. Prandke, A. Stips, A. Simon and A. Wüest, 1998. Comparison of dissipation of turbulent kinetic energy determined by shear and temperature microstructure. (submitted to *J. Mar. Sys.*).
- Ledwell, J.R., A.J. Watson and C.S. Law, 1993. Evidence for slow mixing across the pycnocline from an open-ocean tracer-release experiment. *Nature* 364: 701–703.

- Lemmin, U. and C.H. Mortimer, 1986. Tests of an extension to internal seiches of Defant's procedure for determination of seiche characteristics in real lakes. *Limnol. Oceanogr.* 31: 1207–1231.
- Maiss, M., J. Ilmberger and K.O. Münnich, 1994. Vertical mixing in Überlingersee (Lake Constance) traced by SF₆ and heat. *Aquat. Sci.* 56: 329–347.
- Mathis, B., 1996. Kleinskalige turbulente Mischung an der Mainauschwelle im Bodensee. Diploma thesis, Swiss Fed. Inst. of Technol. (EAWAG/ETH), 76 pp.
- Mudge, T.D. and R.G. Lueck, 1994. Digital signal processing to enhance oceanographic observations. *J. Atmos. Oceanic. Tech.* 11: 825–836.
- Oakey, N.S. and J.A. Elliott, 1980. The variability of temperature gradient microstructure observed in the Denmark Strait. *J. Geophys. Res.* 85: 1933–1944.
- Oakey, N.S., 1982. Determination of the rate of dissipation of turbulent energy from simultaneous temperature and velocity shear microstructure measurements. *J. Phys. Oceanogr.* 12: 256–271.
- Osborn, T.R., 1980. Estimates of the local rate of vertical diffusion from dissipation measurements. *J. Phys. Oceanogr.* 10: 83–89.
- Peters, H. and M.C. Gregg, 1987. Some dynamical and statistical properties of equatorial turbulence. Proceedings of "Small-scale turbulence and mixing in the ocean", the 19th International Liège Colloquium on Ocean Hydrodynamics. J. Nihoul, ed., Elsevier, Amsterdam.
- Peters, H., M.C. Gregg and J.M. Toole, 1988. On the Parameterization of equatorial turbulence. *J. Geophys. Res.* 93: 1199–1218.
- Peters, H., 1997. Observations of stratified turbulent mixing in an estuary. Neap-to-spring variations during high river flow. *Estuarine, Coastal and Shelf Science* 45: 69–88.
- Richman, J. and C. Garrett, 1977. The transfer of energy and momentum by the wind to the surface mixed layer. *J. Phys. Oceanogr.* 7: 876–881.
- Schimmele, M., 1993. Anregung interner Seiches im Bodensee durch den Wind. Ph.D. diss., Inst. Umweltphysik, Univ. Heidelberg, 161 pp.
- Schlatter, J.W., A. Wüest and D.M. Imboden, 1997. Hypolimnetic density currents traced by sulphur hexafluoride (SF₆). *Aquat. Sci.* 59: 225–242.
- Seim, H.E. and M.C. Gregg, 1994. Detailed observations of a naturally occurring shear instability. *J. Geophys. Res.* 99: 10049–10073.
- Shay, T.J. and M.C. Gregg, 1986. Convectively driven turbulent mixing in the upper ocean. *J. Phys. Oceanogr.* 16: 1777–1798.
- Spigel, R.H. and J. Ilmberger, 1980. The classification of mixed-layer dynamics in lakes of small to medium size. *J. Phys. Oceanogr.* 10: 1104–1121.
- Stigebrandt, A., 1989. Vertical mixing in basin waters of fjords. *J. Phys. Oceanogr.* 19: 917–926.
- Van Senden, D.C. and D.M. Imboden, 1989. Internal seiche pumping between sill-separated basins. *Geophys. Astrophys. Fluid Dyn.* 48: 135–150.
- Wesson, J.C. and M.C. Gregg, 1994. Mixing at Camarinal Sill in the Strait of Gibraltar. *J. Geophys. Res.* 99: 9847–9878.
- Wüest, A., D.M. Imboden and M. Schurter, 1988. Origin and size of hypolimnetic mixing in Urnersee, the southern basin of Vierwaldstättersee (Lake Lucerne). *Schweiz. Z. Hydrol.* 50: 40–70.
- Wüest, A., D.C. Van Senden, J. Ilmberger, G. Piepke and M. Gloor, 1996. Comparison of diapycnal diffusivity measured by tracer and microstructure techniques. *Dyn. Atmos. Oceans* 24: 27–39.
- Wüest, A. and M. Gloor, 1998. Bottom boundary mixing in lakes: The role of the near sediment density stratification. In: J. Ilmberger (ed.), "Physical Limnology", Coastal and Estuarine Studies, AGU series 464–480.
- Zenger, A., 1989. Ursachen und Auswirkungen von Transport- und Mischungsprozessen im westlichen Bodensee. Ph.D. diss., Inst. Umweltphysik, Univ. Heidelberg, 137 pp.
- Zenger, A., J. Ilmberger, G. Heinz, M. Schimmele, P. Schlosser, D.M. Imboden and K.O. Münnich, 1990. Behavior of a medium-sized basin connected to a large lake. In: M.M. Tilzer and C. Serruya (eds.), "Large lakes: ecological structure and function". Springer Verlag, Berlin and Heidelberg, pp. 133–155.

Received 24 March 1997;

revised manuscript accepted 22 January 1998.

Flow regime in the Irbe Strait

Madis-Jaak Lilover¹, Urmas Lips¹, Janek Laanearu¹ and Bengt Liljebladh²

¹ Department of Marine Physics, Estonian Marine Institute, Tallinn, Estonia

² Department of Oceanography, Gothenburg University, Gothenburg, Sweden

Key words: Semi-enclosed bay, water exchange, strait flow, current fluctuations.

ABSTRACT

The current structure in a strait connecting a semi-enclosed bay and the Baltic Sea is studied on the basis of data obtained during the Gulf of Riga Project in 1993–1995. The observations comprised hydrographic snapshots and a 10-day intense campaign IRBEX-95 of CTD, current, sea-level and meteorological measurements. The baroclinic forcing due to the density difference, the barotropic forcing due to the sea-level difference, and the wind forcing are considered as factors driving the water flow through the Irbe Strait. A regular flow scheme (outflow in the northern part and inflow near the southern slope of the strait) which is related to the quasi-permanent salinity front was shown to prevail on average. Current oscillations having inertial and diurnal periods and forcing-dependent current fluctuations are frequently observed to be superimposed on the mean structure of the currents. A relatively quick response of the hydrographic fields to almost periodic (2-day) changes of the local wind and the sea level is stated. The current is preferably contra-directional to the wind stress, but well correlated with the sea level difference between the open sea and the strait. However, the described regular current scheme seems to contribute the most to the water, salt and nutrient exchange through the Irbe Strait.

Introduction

The water quality of a semi-enclosed basin depends crucially on the water, nutrients and pollutants exchange through straits connecting the basin with the open sea. Therefore, strait dynamics have continuously attracted oceanographers. The main efforts, both theoretical and observational, have been directed at describing the flow in narrow straits (ignoring the earth's rotation) like the Strait of Gibraltar (see e.g. Farmer and Armi, 1986; Armi and Farmer, 1988). The flow structure in wide channels where the earth's rotation can not be ignored has been discussed by Whitehead et al. (1974), Gill (1977), Pratt and Lundberg (1991). Several studies have shown the flow regime response to the atmospheric, buoyancy and tidal

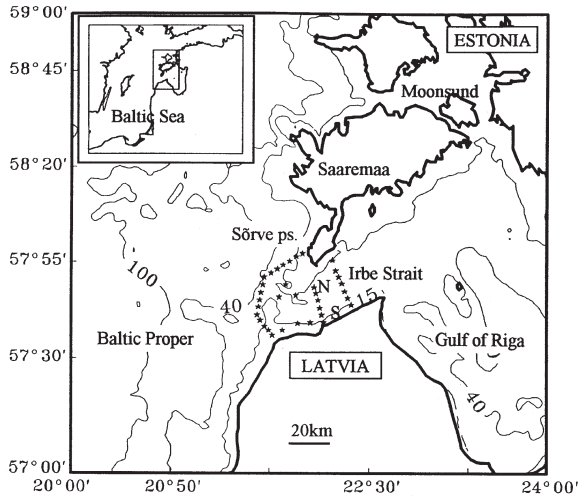


Figure 1. Map of the study area showing the topography and the locations of stations during IRBEX-95. Depths are in meters. The main transect in the Irbe Strait is marked by SN

forcing in estuary-type transition areas (Csanady, 1978; Wang, 1979; Wong and Münchow, 1995). A series of numerical experiments have been performed to study the effects of altering estuarine flow, coastal flow, coastal bathymetry and salinity gradient on the dynamics of the transition region (Valle-Levinson et al., 1996). The ability of deep estuaries connected to the open sea by a narrow strait to exhibit either an amplified or damped response to the tide have been reported (Maas, 1997).

Although the water exchange between the Gulf of Riga and the Baltic Proper through the Irbe Strait has been investigated in a few studies (Pastors, 1967; Baranov, 1970; Mardiste, 1975; Petrov, 1979) the factors determining the observed pattern of inflow/outflow have not been described satisfactorily. The connections of the Gulf of Riga (total volume of 410 km^3 and maximum depth of 60 m) with the Baltic Proper are the Irbe Strait (sill depth 25 m, cross-section area 0.4 km^2 , width about 30 km) in the west and the Moonsund area (sill depth 5 m, the narrowest cross-section area 0.04 km^2) in the north (Fig. 1). The fresh-water supply from the rivers averages to 30 km^3 per year (Yurkovskis et al., 1993). Because of the restricted water exchange through the straits the mean salinity in the gulf is about 1.5–1.7 psu lower than in the adjacent region of the Baltic Proper. This corresponds to the density difference about 1.0 kg m^{-3} . The annual volumes of the flow into the Gulf of Riga (inflow) and the flow toward the Baltic Sea (outflow) through the Moonsund area were estimated to be as much as 100 km^3 and 150 km^3 , respectively, on the basis of direct current measurements extrapolated over the whole year (Mardiste, 1975). The flow rate through the Irbe Strait in both directions has been estimated to vary over a wide range – from 150 km^3 to 690 km^3 per year – mainly due to the different estimation methods used. According to the water and salt conservation equations for the Gulf of Riga and taking into account the volume of

the gulf, mean river input, mean salinity in the gulf (5.6 psu) and mean salinity in the adjacent region of the open sea (7.2 psu) the yearly mean net water exchange between the two basins should only be about 105 km³ (inflow) and 135 km³ (outflow) per year. Thus the residence time for salt in the Gulf of Riga is about 3 years. The remarkably larger values of the water exchange obtained on the basis of direct current measurements could be explained by the circumstances that previous investigations estimated the real flow rate (back and forth) through a cross-section instead of the net water exchange between the Gulf of Riga and the Baltic Proper.

A two-layer (Pastors, 1967) fluctuating character of currents (Petrov, 1979) has been stated in the Irbe Strait. However, only the wind forcing was considered as the main driving force (acting directly or via sea level elevations) for the currents in both straits. The role of the estuarine-like circulation due to the mean horizontal pressure gradients between the basins has so far not been taken into account. The current fluctuations were supposed to have mainly tidal origin (Petrov, 1979). Almost no attention has been paid to possible amplification of eigen-oscillations of basins in the strait areas.

The main aim of the present paper is to determine the physical processes (and the related flow fields) controlling the water exchange between the Gulf of Riga and the Baltic Proper. The data of the hydrographic snapshots in the study area in 1993–1994 are used to characterise the structure of the hydrographic fields and prevailing flow scheme in the transition zone. The current response to the changes in wind and sea level is studied on the basis of data of the 10-day detailed measurement campaign IRBEX-95 in June, 1995.

Measurements

One of the main tasks of the Gulf of Riga Project (initiated by the Nordic Council of Ministers) was to estimate the water exchange between the Gulf of Riga and the Baltic Proper. In the framework of this project, detailed hydrographic measurements and current observations were carried out in the Irbe Strait area in 1993–1995. Three surveys were performed in 1993 and the study area was covered almost monthly in 1994. Several research vessels – R/V Kiir (Estonia), R/V Argos (Sweden), R/V Muikku (Finland) and R/V A.v. Humboldt (Germany) – participated in the measurement campaign. The temperature, salinity and density fields were measured using a Neil Brown Instrument Systems Mark III Conductivity-Temperature-Depth (CTD) probe. Time-series of current velocity were recorded by Aanderaa current meters (RCM-4 and RCM-7) at mooring stations. A ship-board Acoustic Doppler Current Profiler (ADCP) was used to measure currents along the transects in the Irbe Strait.

The objective of the experiment in June 6–15, 1995 (IRBEX-95) was to perform a 10-day study measuring salinity, temperature, currents and nutrients along several transects in the Irbe Strait as well as meteorological parameters and sea level at the coastal and off-shore stations. Our intention was to focus the investigations on frontal circulation and evolution in time.

Two ships – R/V Kiir (Estonia) and R/V Skagerak (Sweden) – operated simultaneously in the area. R/V Kiir carried out a meso-scale CTD-survey in the whole Irbe

Strait area in the beginning and at the end of the experiment. The detailed CTD and ADCP measurements along the selected cross-section (transect SN; see Fig. 1) in the central part of the strait were repeated by two ships totalling 16 times. Additional CTD and ADCP measurements were provided by R/V Skagerak in the sill area at several transects. Two mooring stations with two Aanderaa current meters at depths of 5 and 17 meters were deployed close to the ends of the transect SN (Fig. 1, the second asterisk from both ends marks the location of the mooring station). The meteorological parameters were measured at a coastal station in Sörve with a time interval of 3 hours and information on weather conditions was also recorded during the cruises of both research vessels. One tide gauge station at the tip of the Sörve Peninsula and three bottom-mounted versions of tide gauges (Richard Brancher Research Ltd., Canada) in the off-shore region (the first – outside, the second – in the channel and the third – in the Irbe Strait) were installed for the sea level measurements (details of data analysis are reported in Lips and Lilover (1995)). Current meters and tide gauges data were recorded with a time interval of 10 minutes.

Results and discussion

The main forcing components

Baroclinic forcing due to the density differences between the Gulf of Riga and the Baltic Proper, barotropic forcing due to the sea level differences between these basins, and wind forcing can be considered as the main factors driving the water flow through the Irbe Strait. The mean salinity difference between the Gulf of Riga water and waters in the surface layer of the adjacent region of the Baltic Sea (about 1.6 psu) results in a density difference (ΔD) of about 1 kg m^{-3} . The corresponding mean horizontal baroclinic pressure gradient (p_{x1}) at the sill depth $H=25 \text{ m}$ can then be calculated as:

$$p_{x1} = \frac{g \cdot H \cdot \Delta D}{L_1} \quad (1)$$

where g is the acceleration of gravity and L_1 – the width of the transition zone. Long-term sea level measurements at the Estonian and Latvian coastal stations indicated that the mean water level of the gulf is about 2 cm higher than in the Baltic Proper (Terziev et al., 1992). The corresponding mean horizontal pressure gradient between the basins due to the water level differences can be found as:

$$p_{x2} = \frac{g \cdot D \cdot \Delta H}{L_2} \quad (2)$$

where ΔH is the mean water level difference, D – the water density and L_2 – the base of the barotropic forcing. A comparison of the mean baroclinic and barotropic forcing, assuming $L_1 = L_2$, yields:

$$\frac{p_{x1}}{p_{x2}} = \frac{H \cdot \Delta D}{D \cdot \Delta H} \approx \text{Order (1)} \quad (3)$$

Thus the mean baroclinic and barotropic forcing have the same magnitude. This balance supports the idea that the dynamics in the Irbe Strait should be characterised on average as a typical estuarine circulation. The bottom water is forced to flow in by the pressure gradient due to the density difference between the basins and the surface water is forced to flow out by the surface pressure gradient due to the water level difference.

The wind forcing, playing an important role for the flow on time scales of several days or less, does not seem to be directly responsible for the mean current scheme in the strait as the induced flow is frequently forced to change direction back and forth. However, the long-term wind forcing can support or break up the mean flow regime for some time. The model calculations (Raudsepp and Elken, 1995) indicated that strong northerly winds support the near-bottom inflow by a compensating flow, and long term south-easterly winds lead to the inflow of the full water column because of superimposed Ekman drift.

To assess the importance of the earth's rotational effects the internal Rossby deformation radius can be estimated as:

$$R_D = \frac{1}{f} \cdot \left(\frac{g \cdot H_D \cdot \Delta D}{D} \right)^{\frac{1}{2}} \quad (4)$$

where f ($= 1.23 \cdot 10^{-4} \text{ s}^{-1}$) is the Coriolis parameter and H_D ($= 15 \text{ m}$) is the thickness of the layer. Using these values and the value of density difference given above, one get $R_D \approx 3.2 \text{ km}$. Therefore, the introduced scaling suggests that the strait is sufficiently wide to allow occurrence of rotationally dominant meso-scale features.

Observed circulation in the Irbe Strait

A quasi-permanent sharp salinity front separating the Gulf of Riga and the Baltic Proper waters was the most pronounced thermohaline structure according to the hydrographic surveys in the Irbe Strait area in 1993–1995 (Lips et al., 1995). Relying on the theoretical considerations described above and the geostrophically balanced water flow, the S-shaped frontal boundary (see Fig. 2, upper panel) indicates that the Gulf of Riga water should flow out in the northern part of the strait and the open-sea water flow in along the southern slope of the strait. This S-shaped flow structure is similar to a fluid flow responding to gravitational forces in a rotating channel (Gill, 1976). If the channel is wide compared with the internal Rossby radius of deformation, the controlled solution for large time involves the boundary layer flow with the upstream current concentrated to the left-hand wall and the downstream current to the right-hand wall of the channel (observer facing downstream). The vertical structure of the density field at the cross-section (transect SN) is similar to the latter flow scheme (Fig. 2, lower panel). The inclination of the boundary between the open sea water and the gulf water indicates that the flows in

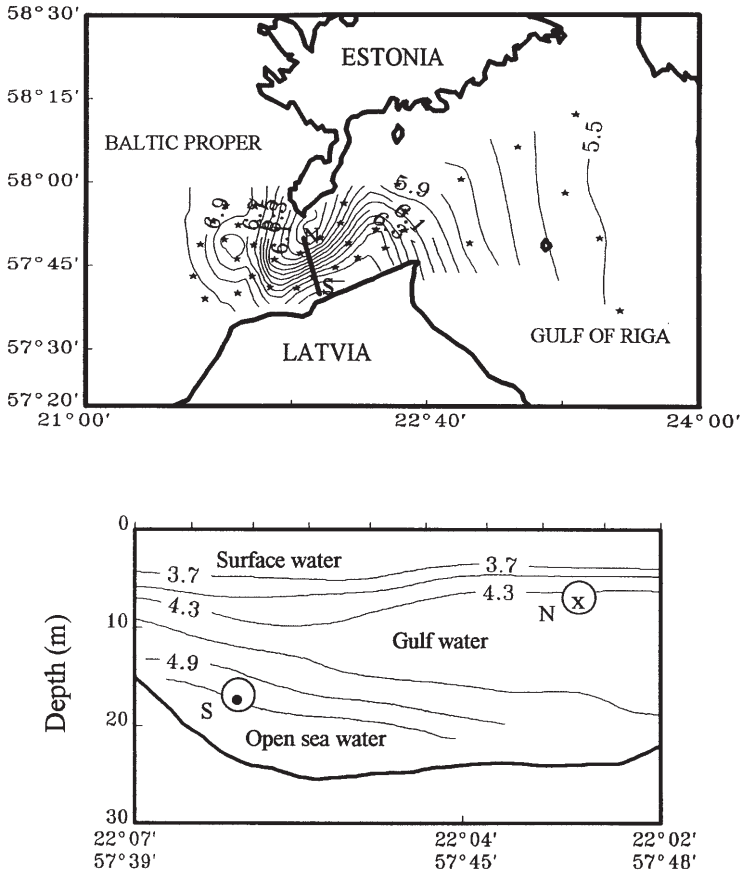


Figure 2. Map of salinity at 15 m depth in the Irbe Strait area from June 6–8, 1995 (upper panel) and vertical section of density at transect SN on June 9, 1995 (lower panel). The locations of current meters (marked by rings) and the observed prevailing flow directions during IRBEX-95 are shown (• indicates flow into the gulf, and x toward the open sea). The high density gradient in the upper layer marks the thermocline and in the lower layer, the halocline

the discussed layers must be contra-directional. The direct current measurements in the Irbe Strait by a shipboard ADCP in the layer 7–9 m depth reflect the expected current structure in the frontal area very well (Fig. 3). The contra-directional flow in the frontal area as well as the outflow near the northern coast and the inflow near the southern coast can be clearly distinguished.

Repeated ADCP surveys indicated however that the described flow scheme can switch to a unidirectional flow in case of strong barotropic forcing (R/V A. v. Humboldt measurements in August 16, 1994; data not shown). Furthermore, inertial oscillations, seiches and direct wind-induced drift currents could add a fluctuating character to the mean current scheme. It is worth noting that no significant tidal currents exist in the Baltic Sea. The two-layer, oscillating flow was observed at the

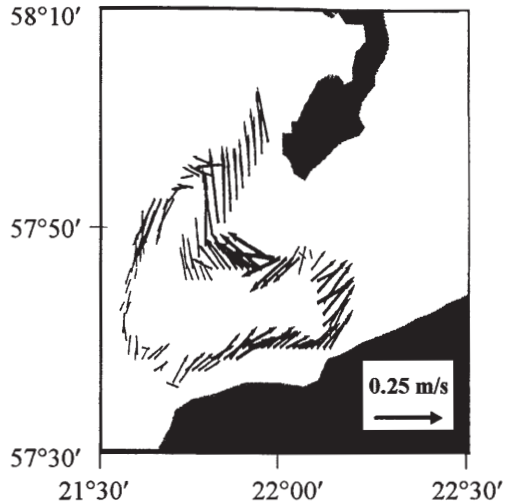


Figure 3. Map of current velocity in the layer between 7 and 9 m depth during an ADCP survey in the Irbe Strait area on June 12, 1995

repeated ADCP cross-section in the Irbe Strait in July 18, 1994 (Fig. 4, measurements are repeated with a time interval of 18 h which is close to a 1.5 quasi-inertial wave period, local inertial period ≈ 14.2 h). The presence of inertial oscillations here was proven by data of simultaneous current measurements at a mooring station situated near the cross-transect. The progressive vector diagram revealed the classical pattern of the inertial oscillations superimposed on the mean flow (Talpsepp, pers. comm.). Still, a relatively stable character of the detected current jet near the southern slope on the background of the oscillations has to be pointed out.

On the basis of an extended current time series it was detected that the most energetic current oscillations have semi-diurnal, inertial and diurnal periods (Raudsepp, 1995; Lilover et al., 1995). Petrov (1979) proposed that the semi-diurnal and diurnal periods have a tidal origin (M1 and K1 tide respectively). This hypothesis was rejected by Raudsepp and Elken (1995) who simulated daily oscillations by the GFDL circulation model where the tidal forces were not included. Considering the Irbe Strait/Gulf of Riga system as a Helmholtz resonator, one can get an eigenoscillation period of about 24 h (Otsmann et al., 1997). The observed intensive currents with the diurnal period can be explained by the response of the system to the exterior forcing with periods close to the system oscillation eigenperiod. The atmospheric forcing, tidal forcing and the Baltic Sea barotropic seiches with periods 26.4 and 22.4 h for modes 2 and 3 respectively (Wübbler and Krauss, 1979) act as the exterior forcing agents.

Response of currents to the changing forcing components

The figures referred to above to confirm the theoretical speculations represent just snapshots of the hydrographic fields. Unlike the former campaigns, the IRBEX-95

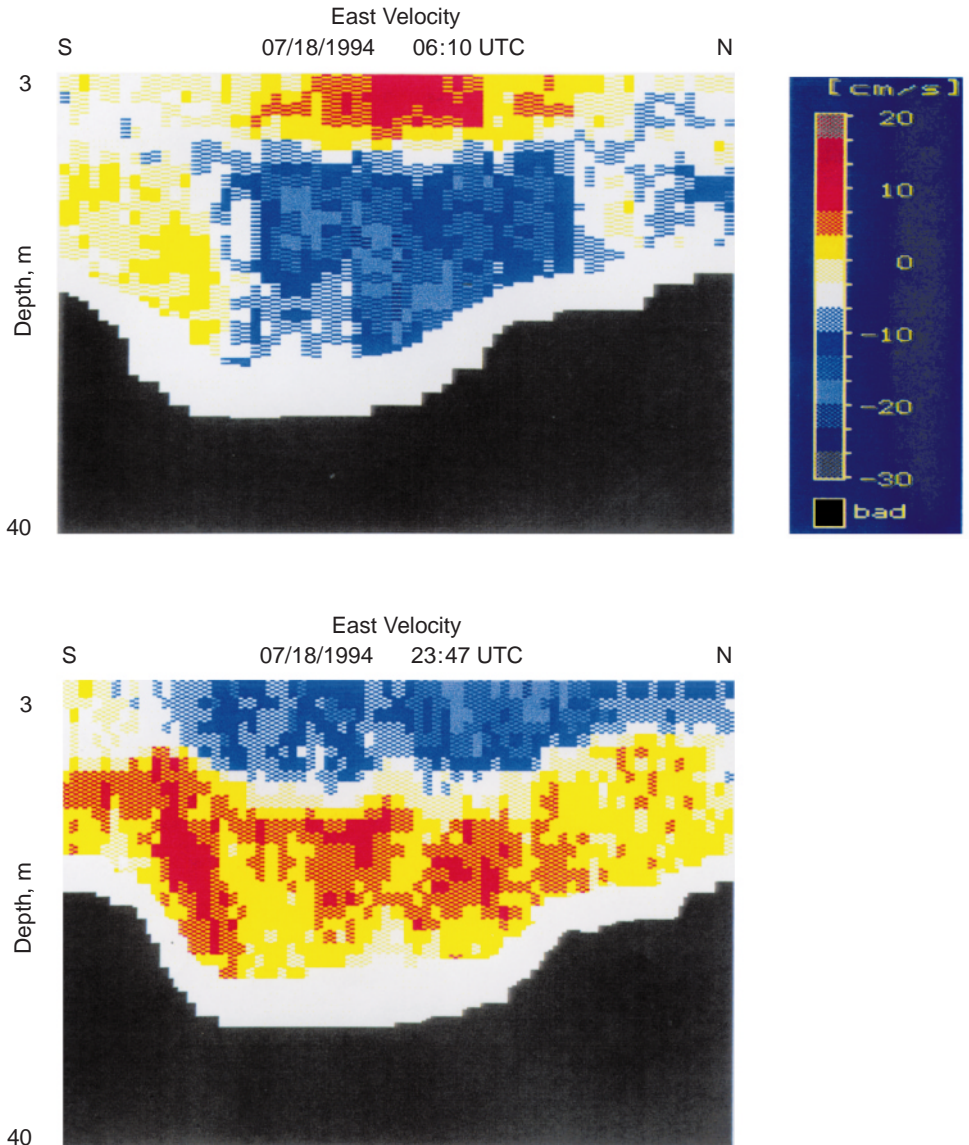


Figure 4. Vertical sections of East velocity at the transect across the Irbe Strait (repeated with time interval of 18 hours) on July 18, 1994. The thermocline locates at 12 m depth

provided us with a more complex data set for changing meteorological conditions during a 10-day period. Three low-pressure patterns passed the study area – on June 8, 10 and 12, resulting in intermittent westerly and easterly winds up to 10 m s^{-1} with an oscillation period of 2 days (see Fig. 5, upper panel). The sea level fluctuations at all off-shore tide gauge stations as well as the sea-level difference between the

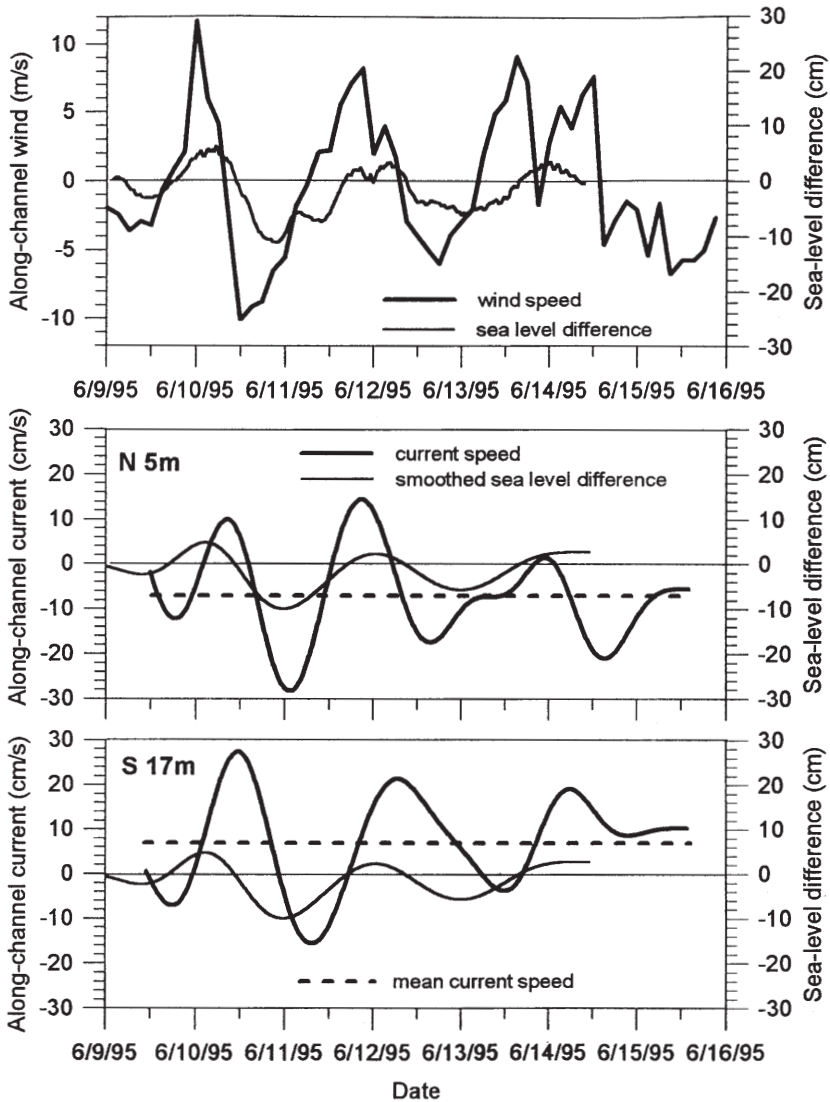


Figure 5. Sea level difference (outer-inner) and along-channel wind speed during IRBEX-95 (upper panel). Positive values refer to the wind blowing from NNE. Low-passed sea level difference, current speed at the northern (N 5 m) and southern (S 17 m) buoy stations (lower panels). Positive current is directed toward NNE, dashed lines indicate the survey mean values

outer and inner tide gauges (the along channel distance between them is about 30 km) exposed nearly the same 2-day period. The unfiltered current field revealed oscillations with about 1- and 2-day periods at both mooring stations. The current fluctuations with the diurnal period can be considered as the basin eigen-oscillations. The low-passed current field (variations with diurnal and smaller periods

Table 1. Cross-correlation coefficients r and the corresponding time-lags τ between along-channel wind stress, sea level difference and along-channel current velocities at stations N (5 m depth) and S (17 m depth). The first two extremes of the function $r(\tau)$ are given

	wind stress		sea level difference		current velocity at N (5 m)		current velocity at S (17 m)	
	τ (hours)	r	τ (hours)	r	τ (hours)	r	τ (hours)	r
wind stress	0	1.0	-6	-0.91	-6	-0.53	-15	-0.77
	24	-0.58	18	0.76	18	0.36	6	0.76
sea level difference	6	-0.91	0.0	1.0	-1.5	0.65	-9.7	0.85
	30	0.54	23.8	-0.67	21.9	-0.43	11.7	-0.73
current velocity at N (5 m)	6	-0.53	1.5	0.65	0.0	1.0	-6.8	0.67
	27	0.67	21.7	-0.69	17.3	-0.72	11.0	-0.88
current velocity at S (17 m)	15	-0.77	9.7	0.85	6.8	0.67	0.0	1.0
	39	0.48	32.7	-0.65	31.4	-0.32	20.0	-0.66

excluded) shows fluctuations with periods close to the characteristic forcing changes (Fig. 5, lower panels; locations of current meters are marked as N and S in Fig. 1 and 2). An analysis of the extent of the observed low-frequency current fluctuations, determined by the oscillating forcing components, is given below.

The cross-correlation coefficients between the time sequences of the along-channel wind stress, the water level difference between the outer and inner tide gauges and the along-channel current velocities at 5-meter depth at the northern station (N) and 17-meter depth at the southern station (S) are given in Table 1. Before correlation calculations the recorded time series were filtered by the fifth-order Butterworth filter with the cut-off frequency of 0.042 cph to exclude the oscillation with a diurnal period (Parks and Burrus, 1987). The first two extreme values of the cross-correlation coefficients (r) and the corresponding time lags (τ) for each pair of variables are indicated in the table (all presented r values are significant at the 5% level). The cross-correlation coefficients are calculated between parameters given in the top row and in the left column, therefore a positive time lag indicates that the parameter in the top row leads the parameter in the left column and negative time lag indicates that the parameter in the top row lags the parameter in the left column.

The auto-correlation functions give the following periods for the prevailing fluctuations: 48 h for wind stress and sea-level difference, 35 h at station N and 40 h at station S for current. High cross-correlation between the wind stress and the sea-level difference ($r = -0.91$) is observed at a time lag of 6 h. A negative coefficient means that westerly winds (eastward wind stress) are correlated with negative and easterly winds with positive sea-level difference between the open sea and the strait. The cross-correlation coefficient between the wind stress and the current at station N is negative for the extreme value with the lowest positive time lag of 6 h ($r = -0.53$). The first maximum of the cross-correlation function ($r = 0.67$) cor-

responds to a time lag of 27 h. It means, at least for the measurement period, the current is preferably contra-directional to the wind stress (with some lag in time). The time lag of the current at station N versus the sea level difference is -1.5 h for the positive correlation value $r = 0.65$. Thus, the current and the sea level fluctuate in phase – an eastward current corresponds to a higher sea level in the open sea and a westward current to a higher sea level in the strait.

The described negative correlation between the wind stress and the sea-level difference can be explained by the restricted water exchange through the strait with smaller cross-section. Thus the wind stress and the horizontal pressure gradient work against each other with a time lag of about 6 h. The correspondence of the low-frequency currents to the sea-level fluctuations as well as the oscillating nature and high velocities point to a wave-like origin of currents. Because of the barotropic Rossby radius ($R_0 = (gH)^{1/2}/f$, $R_0 \approx 100$ km) being much larger than the width of the strait, the entire water column in the strait should expose oscillations in coinciding phases. However, the time lag of the current at the southern station versus the current at the northern station was found to be -6.8 h ($r = 0.67$). Thus, on the basis of our measurements, the observed fluctuations of currents and sea level in the Irbe Strait area cannot be explained by entering a barotropic Kelvin wave into the channel.

Despite of the large 2-day fluctuations, the mean current velocities (mean outflow -7 cm/s in the northern part and inflow $+7$ cm/s along the southern slope during the survey) agreed well with the regular structure of the hydrographic fields in the Irbe Strait. The estimated distance which a water parcel can cover during one half of the 2-day oscillation period is less than 10 km. Because of the 30 km length of the strait these movements are too short to produce large inflows into the gulf. Therefore, the relative movements of the water masses – the inflow of the Baltic Sea water in the lower layer of the southern part and the outflow of the gulf water in the northern part of the strait – seem to give the largest contribution to the water, salt and nutrient exchange through the Irbe Strait.

Conclusions

A frontal circulation scheme of currents (outflow in the northern part and inflow along the southern slope) associated with a quasi-permanent “S”-shaped salinity front prevails in the Irbe Strait. These currents are driven by the horizontal pressure gradients between the basins (depending on the density and the sea-level differences) and could be described in accordance with the quasi-geostrophic assumption. The volume flux calculations using the current and CTD measurement data and the method introduced by Petren and Walin (1979) gave an average value for the quasi-steady inflow of 5200 m³ s⁻¹ (mean inflowing water salinity 6.53 psu) for the 10-day period under investigation (Laanearu, 1996). This result yields an annual inflow of 164 km³, which is essentially consistent with the smaller flow (105 km³ per year) with higher salinity (7.2 psu) estimated from the budget calculations.

A relatively quick response of the hydrographic fields to changes in the local wind and the sea level variations in the Irbe Strait was stated. Westerly winds are correlated with negative and easterly winds with positive sea-level difference

between the open sea and the strait. The current is preferably contra-directional to the wind stress, but well correlated with the sea level elevations – an eastward current corresponds to a higher sea level in the open sea and a westward current to a higher sea level in the strait. The dynamics allowing coexistence of the forcing-dependent 2-day current oscillations and the quite stable regular flow scheme in the Irbe Strait needs to be studied in more detail in the future.

In general, a better understanding of the physics governing the regular flow scheme and the different scale current fluctuations in the Irbe Strait area is achieved. The finding that the quasi-permanent currents could contribute the most to the water, salt and nutrient exchange through the Irbe Strait is important for the future management of the Gulf of Riga.

ACKNOWLEDGEMENTS

This work was financially supported by the Nordic Council of Ministers (The Gulf of Riga Project). The authors acknowledge the valuable help of Tarmo Kõuts, Bertil Håkansson, Lembit Talpsepp and Aleksander Toompuu. We also appreciate the assistance of the crews of the research vessels Kiir, Skagerak, A. v. Humboldt and Muikku. Special thanks to Anders Stigebrandt arranging cooperation between Estonian Marine Institute and Gothenburg University.

REFERENCES

- Armi, L. and D. Farmer, 1988. The flow of Mediterranean water through the Strait of Gibraltar. *Prog. Oceanogr.* 21:1–105.
- Baranov, A., 1970. Currents in the Gulf of Riga and Irbe Strait. *Proceedings of the Riga Meteorological Observatory*, 13, pp. 30–82 (in Russian).
- Csanady, G. T., 1978. Wind effects on surface to bottom fronts. *J. Geophys. Res.* C9:4633–4640.
- Farmer, D. and L. Armi, 1986. Maximal two-layer exchange over a sill and through the combination of a sill and contraction with barotropic flow. *J. Fluid Mech.* 164:53–76.
- Gill, A. E., 1976. Adjustment under gravity in a rotating channel. *J. Fluid Mech.* 77:603–621.
- Gill, A. E., 1977. The hydraulics of rotating-channel flow. *J. Fluid Mech.* 80:641–671.
- Laanearu, J., 1996. Sill flow observations between sub-basins and analytical description of frictionless strait flow (the Gulf of Riga and the Baltic Proper). MS Thesis, University of Tartu. 62 pp.
- Lilover, M.-J., U. Raudsepp and T. Kõuts, 1995. Variability of the velocity field and its relation to the external forcing in the Gulf of Riga. In: A. Toompuu and J. Elken (eds.), *EMI Report Series*, 1, Tallinn, pp. 35–83.
- Lips, U. and M.-J. Lilover, eds., 1995. *IRBEX-95 Data Report*, EMI Report Series, 2, Tallinn, 112 pp.
- Lips, U., M.-J. Lilover, U. Raudsepp and L. Talpsepp, 1995. Water renewal processes and related hydrographic structures in the Gulf of Riga. In: A. Toompuu and J. Elken (eds.), *EMI Report Series*, 1, Tallinn, pp. 1–34.
- Maas, L. R. M., 1997. On the nonlinear Helmholtz response of almost-enclosed tidal basins with sloping bottoms. *J. Fluid Mech.*, 349:361–381.
- Mardiste, H., 1975. Volume transports in Muhu Straits – Väinameri. In: *Dynamics of water in the Baltic Sea. Proceedings of the Estonian Academy of Sciences*, pp. 88–94 (in Russian).
- Otsmann, M., V. Astok and Ü. Suursaar, 1997. A model for water exchange between the Baltic Sea and the Gulf of Riga. *Nordic Hydrology*, 28:351–364.
- Parks, T. W. and C. S. Burrus, 1987. *Digital filter design*, J. Wiley and Sons, N. Y., 342 pp.
- Pastors, A., 1967. Water and heat balance in the Gulf of Riga. In: *Morskije zalivy kak priyomniki stochnyh vod*, Riga, pp. 8–20 (in Russian).
- Petren, O. and G. Walin, 1979. Some observations of the deep flow in the Bornholm strait during the period June 1973–December 1974. *Tellus*, 27:74–87.

- Petrov, B.S., 1979. Water balance and water exchange between the Gulf of Riga and the Baltic Proper. In: *Sbornik rabot rzhskoj gidrometeorologicheskoy observatorii*, 18, Riga, pp. 20–40 (in Russian).
- Pratt, L.J. and P.A. Lundberg, 1991. Hydraulics of rotating strait and sill flow. *Annu. Rev. Fluid Mech.*, 23:81–106.
- Raudsepp, U., 1995. Description of Eulerian current velocity measurements and the role of processes of different time scale of the velocity field in the Irbe Strait. In: T. Kõuts and B. Håkansson (eds.), *SMHI RO*, 23, Norrköping, pp. 37–59.
- Raudsepp, U. and J. Elken, 1995. Application of the GFDL circulation model for the Gulf of Riga. In: A. Toompuu and J. Elken (eds.), *EMI Report Series*, 1, Tallinn, pp. 143–176.
- Terziev, F.C., Rozhkov V.A. and A.I. Smirnova (editors), 1992. *The Baltic Sea, Vol. 1: Hydro-meteorological conditions* (in Russian), *Gidrometeoizdat*, S.-Petersburg, 450 pp.
- Valle-Levinson, A., J.M. Klinck and G.H. Wheless, 1996. Inflows/outflows at the transition between a coastal plain estuary and the coastal ocean. *Continental Shelf Research*, 16: 1819–1847.
- Wang, D.P., 1979. Subtidal sea level variations in Chesapeake Bay and relations to atmospheric forcing. *J. Phys. Oceanogr.* 9:413–421.
- Whitehead, J.A., A. Leetmaa and R.A. Knox, 1974. Rotating hydraulics of strait and sill flows. *Geophys. Fluid Dyn.*, 6:101–125.
- Wong, K.-C. and A. Münchow, 1995. Buoyancy forced interaction between estuary and inner shelf: observation. *Continental Shelf Research*, 15:59–88.
- Wübber, Ch. and W. Krauss, 1979. The two-dimensional seiches of the Baltic Sea. *Oceanolog. Acta*, 2:435–446.
- Yurkovskis, A., F. Wulff, L. Rahm, A. Anduzaitis and M. Rodriguez-Medina, 1993. A nutrient budget of the Gulf of Riga; Baltic Sea. *Estuarine, Coastal and Shelf Science*, 37:113–127.

Received 16 December 1996;

revised manuscript accepted 19 January 1998.

Modeling wind-induced circulation in the homogeneous Lake Constance using k - ε closure

Peter M. Güting and Kolumban Hutter

Technische Universität Darmstadt, Institut für Mechanik, Hochschulstr. 1, D-64289 Darmstadt, Germany.

Key words: Turbulence, k - ε model, wind-driven currents, eddy viscosity, vertical mixing, inertial oscillations.

ABSTRACT

Barotropic models of wind-driven circulation commonly use vertical eddy-viscosities which are prescribed functions of depth and applied wind speed rather than a parameterization that is dictated by the turbulence intensity. We use a first order k - ε -closure to do this and demonstrate important qualitative differences with this classical turbulence closure in the pattern of wind induced barotropic currents in ideal basins, as well as in Lake Constance: penetration and Ekman layer depths respond with some delay time to the applied wind history as does the attenuation of inertial oscillations established by the wind. This also affects the topographically-induced current pattern. We demonstrate these features by subjecting the homogeneous Lake Constance to impulsive and spatially uniform external wind forcing of different strengths in the long direction. Specifically, the shallow-water equations are coupled via the vertical eddy-viscosity with the correspondingly approximated balance laws of turbulent kinetic energy and its dissipation, which are then solved numerically.

1 Introduction

Common hydrodynamic models, with the aid of which barotropic wind-induced circulation can be computed, employ zeroth-order turbulent closure, i. e., the vertical turbulent viscosity is set equal to a constant, or sometimes related to the wind speed, or is dependent on the vertical direction (for a review see Heaps (1984)). As such, it is explicitly prescribed rather than allowed to evolve together with the turbulence intensity that is established together with the flow. Higher-order turbulent closure models are free of this deficiency as the computation of the Reynolds stresses by means of transport equations is part of the determination of the circulation pattern that is established by the wind. In this work, we use a first order k - ε -closure model, which computes the turbulent viscosity by means of transport equations for the turbulent kinetic energy and its dissipation. As a consequence, the vertical turbulent viscosities depend both on position and time and thus assume values that are prop-

erly adjusted to the local turbulence intensity. For instance, turbulence activity can then diffuse in space and time, giving rise to a fading memory property of the induced turbulence and so to the wind. This greatly objectifies the prediction of turbulent diffusion mechanisms induced by applied winds.

We shall illustrate that, owing to this induced variability, detailed features in the barotropic current are discernible, which are not seen when prescribed viscosities are used instead. We use the shallow-water equations and couple them through a parameterization of the turbulent vertical viscosity in terms of the turbulent kinetic energy and its dissipation with balance laws for the latter two quantities. These equations are numerically solved by finite difference techniques for the homogeneous Lake Constance subject to wind forcings in the long direction of the lake.

2 Field equations and boundary conditions

The standard governing equations in physical limnology or oceanography are the Boussinesq approximated Navier-Stokes equations on the rotating Earth subjected to the shallow-water approximation; apart from restricting the motions to isochoric deformation fields and eliminating the second Coriolis parameter, these lead to a hydrostatic pressure balance (see e.g. Hutter, 1991; 1993). During the winter season Lake Constance does not show significant stratification, so that the density can be assumed to be constant and the constant gravity term absorbed into the pressure (see e.g. Hutter, 1991). The Reynolds stresses \mathbf{R} are, in these equations, represented by an eddy viscosity parameterization in which horizontal and vertical diffusivity properties account for an anisotropic response; this is incorporated in the horizontal balance relations by distinguishing between horizontal, ν_H , and vertical, ν_t , diffusivities (see equations (2) and (3) below). For barotropic processes, the shallow-water equations then take the following form:

mass-balance

$$\frac{\partial u}{\partial x} + \frac{\partial v}{\partial y} + \frac{\partial w}{\partial z} = 0, \quad (1)$$

momentum-balance

$$\frac{\partial u}{\partial t} + \mathbf{v} \cdot \frac{\partial u}{\partial \mathbf{x}} - f v = -\frac{1}{\rho} \frac{\partial P}{\partial x} + \nu_H \left(\frac{\partial^2 u}{\partial x^2} + \frac{\partial^2 u}{\partial y^2} \right) + \frac{\partial}{\partial z} \nu_t \frac{\partial u}{\partial z}, \quad (2)$$

$$\frac{\partial v}{\partial t} + \mathbf{v} \cdot \frac{\partial v}{\partial \mathbf{x}} - f u = -\frac{1}{\rho} \frac{\partial P}{\partial y} + \nu_H \left(\frac{\partial^2 v}{\partial x^2} + \frac{\partial^2 v}{\partial y^2} \right) + \frac{\partial}{\partial z} \nu_t \frac{\partial v}{\partial z}, \quad (3)$$

in which the horizontal diffusion coefficient is assumed to be constant, whilst its vertical counterpart may be a function of the vertical coordinate z ; (u, v, w) denote the velocity components in the x, y, z directions respectively, \mathbf{v} is the velocity vector

and \mathbf{x} the position vector; f is the Coriolis parameter and P the pressure. Furthermore,

$$\mathbf{v} \cdot \frac{\partial u}{\partial \mathbf{x}} = u \frac{\partial u}{\partial x} + v \frac{\partial u}{\partial y} + w \frac{\partial u}{\partial z}, \quad \text{etc.} \quad (4)$$

Usual zeroth order closure schemes assign values to ν_H and ν_t , the latter possibly as a function of z , but we shall now deviate from this by incorporating the k - ε -closure.

To do so adequately, the transport equations for the turbulent kinetic energy k , and the turbulent dissipation ε , have been derived to obtain an expression for the turbulent viscosity, ν_t in the expression for the Reynolds stress \mathbf{R} , viz.,

$$\frac{1}{\rho} \mathbf{R} = \nu_t (\text{grad } \mathbf{v} + \text{grad}^T \mathbf{v}), \quad \text{with} \quad \nu_t = c_\mu \frac{k^2}{\varepsilon}, \quad (5)$$

where $\text{grad } \mathbf{v}$ is the velocity gradient and $\text{grad}^T \mathbf{v}$ its transpose; k and ε , defined as usual, satisfy classical transport equations (see Rodi, 1993, eqs. (6) and (7); an exact definition of k and ε can be found in Rodi, 1993). These equations contain time-rate of changes and flux terms of k and ε accounting, respectively, for a time dependence and for diffusion of k and ε in all space directions, but by imposing the shallow-water approximation, the horizontal diffusive terms drop out. This means that, to lowest order (i.e., the shallow-water approximation), only the vertical flux components contribute to the diffusion of turbulent kinetic energy and its dissipation. In light of the balances (2) and (3), the thus simplified k - ε equations determine only the vertical turbulent viscosity ν_t . The application of the shallow-water approximation has thus led to a splitting of the horizontal and vertical turbulent processes. We shall, however, still account for the horizontal fluxes of k and ε by assuming a constant diffusivity equal to ν_H ; according to Wang (1996) this is justified as the value of ν_H has no significant influence on the current distribution. Thus the k - and ε -equations take the forms (compare Rodi, 1993):

k and ε -balances

$$\frac{\partial k}{\partial t} + \mathbf{v} \cdot \frac{\partial k}{\partial \mathbf{x}} = \nu_H \left(\frac{\partial^2 k}{\partial x^2} + \frac{\partial^2 k}{\partial y^2} \right) + \frac{\partial}{\partial z} \frac{\nu_t}{\sigma_k} \left(\frac{\partial k}{\partial z} \right) + \nu_t \left(\left(\frac{\partial u}{\partial z} \right)^2 + \left(\frac{\partial v}{\partial z} \right)^2 \right) - \varepsilon, \quad (6)$$

$$\begin{aligned} \frac{\partial \varepsilon}{\partial t} + \mathbf{v} \cdot \frac{\partial \varepsilon}{\partial \mathbf{x}} &= \nu_H \left(\frac{\partial^2 \varepsilon}{\partial x^2} + \frac{\partial^2 \varepsilon}{\partial y^2} \right) + \frac{\partial}{\partial z} \frac{\nu_t}{\sigma_\varepsilon} \left(\frac{\partial \varepsilon}{\partial z} \right) \\ &+ C_{1\varepsilon} \nu_t \frac{\varepsilon}{k} \left(\left(\frac{\partial u}{\partial z} \right)^2 + \left(\frac{\partial v}{\partial z} \right)^2 \right) - C_{2\varepsilon} \frac{\varepsilon^2}{k}. \end{aligned} \quad (7)$$

The above equations (1)–(7) contain six empirical constants, the horizontal diffusivity ν_H , plus five constants for the k - ε model, which were determined by optimization of typical turbulent flow experiments (see Rodi, 1993) and are given in Table 1.

Table 1. Standard k - ε -constants

c_μ	σ_k	σ_ε	$C_{1\varepsilon}$	$C_{2\varepsilon}$
0.09	1.	1.3	1.44	1.92

To solve the above field equations for \mathbf{v} , P , k and ε , boundary conditions must be prescribed along the free surface $z = \xi(x, y, t)$, later replaced by $z = 0$ through the rigid lid assumption, and at the bottom $z = -H(x, y)$. At the former, the two horizontal wind stress components $\underline{\tau}_{\text{WIND}}$ are set equal to the Reynolds stresses R_{xz} and R_{yz} with the usual drag-coefficient parameterization given below in (8). Furthermore, the rigid lid assumption will be imposed, implying vanishing surface elevation $\xi = 0$, and vertical velocity $w = 0$. Also the pressure no longer acts as an independent variable and reduces to the hydrostatic pressure. As for the prescription of k and ε , the lake surface with the superposed wind stress is treated as a moving wall. In the absence of heat fluxes, the boundary conditions take the form (9), where $k = 0.4$ is Kármán's constant, τ_{WIND} the wind stress, and Δz is the distance to the surface (see Svensson, 1978). In Summary, the boundary conditions at the rigid surface read

$$\tau_{\text{WIND}} = \rho \nu_i \left[\left(\frac{\partial u}{\partial z}, \frac{\partial v}{\partial z} \right) \right]_{\text{water}} = C_D \rho_L [\sqrt{u^2 + v^2} (u, v)]_{\text{wind}} \quad (8)$$

$$w = 0, \quad k = \frac{|\tau_{\text{WIND}}|}{\rho \sqrt{c_\mu}}, \quad \varepsilon = \left(\frac{|\tau_{\text{WIND}}|}{\rho} \right)^{(3/2)} \frac{1}{k \Delta z}. \quad (9)$$

in which $\rho_L = 1.225 \text{ kg m}^{-3}$ and $C_D = 1.8 \cdot 10^{-3}$ (following Lehmann, 1992) are the density of air and the dimensionless drag coefficient, respectively. In the computations, the wind stress is fed into the model by prescribing the wind speed, and C_D is assumed to be constant, since measurements have indicated this to be sufficiently accurate for wind speeds smaller than 10 m s^{-1} (see Lehmann, 1992).

At the bottom, $z = -H(x, y)$ the ideal-slip condition is applied. Furthermore, motions if existent at all are small, and the turbulent kinetic energy as well as the dissipation vanishes at the ground, implying $k = \varepsilon = 0$. In order to keep CPU-times in the actual computations reasonable, the viscous laminar sub-layer has not been resolved. Thus, k and ε are only defined at grid points inside the water body and not on its boundaries. Computationally, this is implemented by using an adequately configured staggered grid.

3 Numerics and definition of model computations

It is beyond the scope of this paper to give a full description of the complex numerical techniques that have been used to solve the equations, however a short overview shall be given. Finite differences on a staggered grid are applied in all three space directions. The horizontal plane is parameterized with curvi-linear orthogonal shore-following coordinates obtained by conformal mappings while the vertical

direction is described by a general topography-following s -coordinate as proposed by Song and Haidvogel (1994). In our application, $s \in [0, -1]$ is chosen so as to achieve a linear mapping of the Cartesian coordinate $z \in [0, -H(x, y)]$ between surface and bottom. For all terms of the equations except the vertical mixing an explicit leapfrog time scheme with an occasional trapezoidal correction step is applied. For the vertical mixing, the implicit Crank-Nicholson time scheme is implemented, achieving numerical stability for larger time steps (see e.g. Press (1994) for the mentioned numerical techniques). The vertically integrated currents are calculated by solving the vorticity equation with a multi-grid solver. The numerical code for calculating the currents was developed by Haidvogel et al. (1991) as described in Hedström (1994), while the k - ϵ -equations have been implemented by Gütting (1998).

Lake Constance is a 65 km long, 17 km wide Alpine lake; here, attention is focused on the larger two basins Obersee and Überlinger See having a maximal depth of 250 m (for a description, see e.g. Hollan and Simons, 1978). The lake geometry was discretized by a curvilinear net with 65×17 grid points in the horizontal and 40 nodes in the vertical direction. A description of this discretization is given in Hutter et al. (1998) or Wang (1996). Computations were performed with this discretization, a Coriolis parameter $f = 1.07 \cdot 10^{-4} \text{ s}^{-1}$ and a horizontal mixing coefficient $\nu_H = 10 \text{ m}^2 \text{ s}^{-1}$. (This is a bit large, the computational results, however, are rather insensitive to its exact value.)

The wind was applied to a water mass initially at rest. It abruptly sets in at $t = 0$ constant in time and uniform in space, directed 125° North, which is approximately in the long direction of the lake. Here we report on results obtained for such a scenario for two wind speeds of 3 m s^{-1} and 4.7 m s^{-1} , respectively. Computations span a two day period.

4 Results

Figure 1a and 1b show a transect of the lake geometry from Überlingen at the western end of Lake Überlingen (left) to the eastern end at Bregenz (right) following more or less the talweg of the bathymetry and extending over 65 km. The Figures display the along-talweg horizontal velocity in the approximate range (-2 cm s^{-1} , 7 cm s^{-1}) for the second day after the wind sets in. Panel a) is for a wind strength of 4.7 m s^{-1} , panel b) for 3 m s^{-1} . Velocity isolines are shown; positive values denote flow with the wind, negative values are indicative of a current against the wind. In Lake Überlingen, the flow decreases with increasing depth and essentially vanishes beneath a certain depth, showing an Ekman-type layer with some local deviations. In the Obersee, such an Ekman-type layer also exists, though not so clearly visible due to the developing barotropic current pattern, which here is much stronger than in Lake Überlingen. The barotropic current leads to a counter-wind flow throughout the depth in the vicinity of the deepest part of the Obersee though decreasing towards the surface due to the wind force. Further, there is a flow with the wind throughout the depth at the eastern most part of the Obersee, again due to the barotropic current pattern, which itself establishes its form through Coriolis force and topography effects.

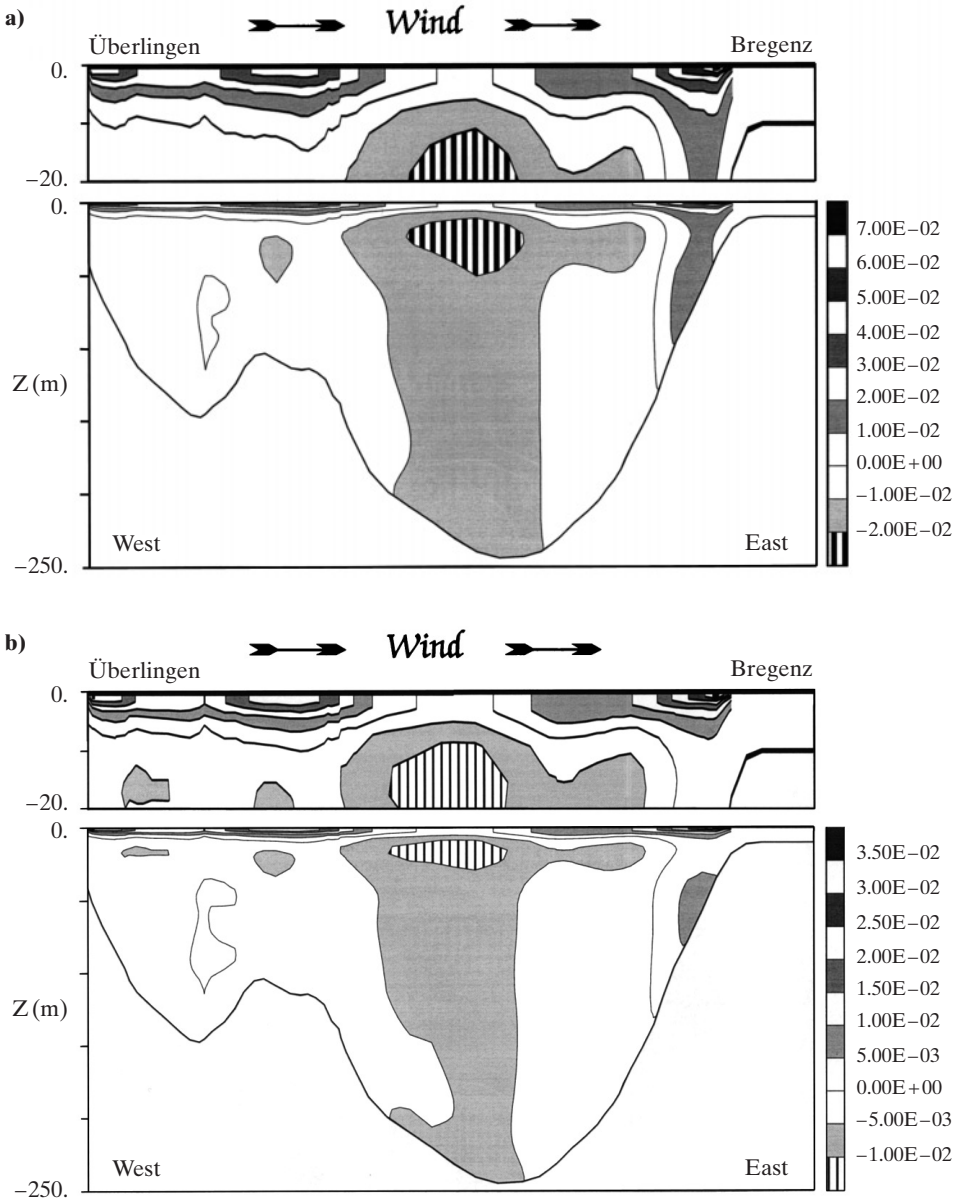


Figure 1. Vertical cut through Lake Constance approximately along the talweg of the bathymetry from the western end at Überlingen (left) to the eastern end at Bregenz (right). Plotted is the along-talweg horizontal velocity field (in m s^{-1}) as isolines with shading as indicated. The current directions with and against the wind are separated by a isoline of zero velocity of which the levels above and below are not shaded in order to better isolate the latter. Wind is uniform in time and space in the direction of the long direction of the lake and the plots are drawn for an instant 2 days after the wind sets in. a) wind speed = 4.7 m s^{-1} , b) wind speed = 3 m s^{-1}

Recalculating the same problem without Coriolis force shows different currents, thus corroborating dependence of the latter on the former; calculating the same problem for a rectangular basin with constant depth, a vanishing depth-averaged flow is obtained. In this case, the fluid transport to the right of the wind in the wind-driven layer is equally compensated by a corresponding cross flow to the left of the wind throughout the depth, which is especially visible beneath the wind-driven layer. No counter-wind flow is established in the basin with constant depth. That a small counter-wind current is present at mid lake positions in Lake Constance demonstrates the influence of the effects of the complex topography. Note also that the main up- and down-welling events (not shown here) result from the fluid-transport of the wind-driven layer in the cross direction of the lake. Qualitatively, the flow patterns in Figures 1 a and 1 b are the same as could be expected if the external wind forcing varies only in amplitude. They would even be similar in calculations using a constant eddy-viscosity. The significant difference manifests itself in the depth of the wind-driven layers, which here may be identified with the isoline for $u = 0$ (except at the eastern most part of the Obersee); this isoline is deeper when the wind is stronger (See Fig. 1 a, b).

Figures 2 a, b show for two wind speeds the vertical profiles of the horizontal velocity components at the mid lake position indicated in the inset. The plotted curves are the Ekman spirals, tracing the horizontal velocity (u, v) 48 hours after the wind sets in. The arrow marks the horizontal velocity at the surface point, and consecutive circles indicate the velocities at 5 m depth intervals from top to bottom. The two Ekman spirals for the higher (panel a) and lower (panel b) wind speed are surprisingly similar, i. e., their projections into the horizontal plane are nearly identical; the orientation of the currents at the five meter depth intervals close to the free surface however is considerably different; for the weaker wind, as one moves downward, the current vector turns faster than for the stronger wind. If we identify the

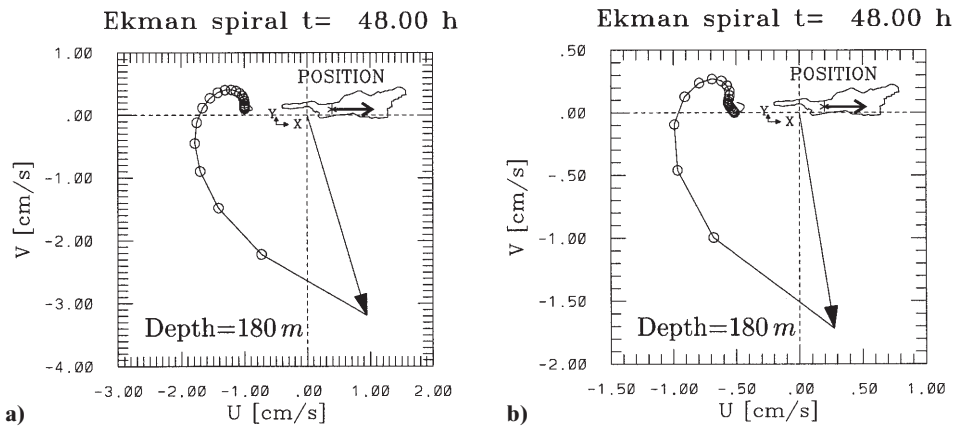


Figure 2. Ekman spirals at the mid-lake position shown in the inset, the wind direction being indicated by an arrow in the inset. The arrows of the figures show the horizontal currents at the surface, circles mark the corresponding currents at 5 m depth intervals down to the bottom. The surface current is to the right of the wind, that at the bottom approximately against the wind. a) wind speed = 4,7 m s⁻¹, b) wind speed = 3 m s⁻¹. The local water depth is 180 m

depth of the wind-driven layer as the location on the spiral beyond which the water current nearly stops turning to the right as one moves downward (in the Figures this is the point on the Ekman spiral where the tangent to it is vertical), then the layer thickness for the weak and strong current is approximately 30 m and 45 m, respectively. In the Ekman spiral of an infinite ocean, the bottom current vanishes; here the bottom current is substantial (about a quarter to a third of the surface current). As described above, it is the barotropic current pattern that drives this current.

Of course, the reason for the difference between the thicknesses of the Ekman depths in the two cases can be traced back to a corresponding variability with position of the vertical turbulent viscosity, as calculated with the k - ϵ equations and shown in Figures 3a,b for the same vertical section as in Figure 1. The weaker wind produces smaller maximum values of vertical turbulent diffusivities and less extended regions with increased values of the eddy viscosity. Since in the k - ϵ model these values are computed, the topography, the wind and the Coriolis effects will all influence them, and the effect of the wind is probably dominant. The depth of the wind-driven layer here is correlated with the turbulent intensities, and is, of course, dependent on the wind.

Prescribing a constant vertical eddy viscosity means neglecting all interactions between currents and turbulent intensities; effectively this amounts to an implicit prescription of the qualitative behaviour and fixes for instance the depth of the wind-driven layer. In the Ekman theory, the depth of the Ekman-layer depends only on the Coriolis parameter and the (constant) vertical eddy viscosity, and is not a function of the wind speed. Thus the Ekman layer has the same depth for all winds, as long as the values of the Coriolis parameter and the eddy viscosity remain constant. Of course, the magnitude of the current changes with the wind, but the current structure does not. Calculations in a rectangular basin or in Lake Constance, using a constant eddy viscosity, also show just this behaviour even though the exact Ekman theory is not applicable as the horizontal gradients are not assumed to vanish.

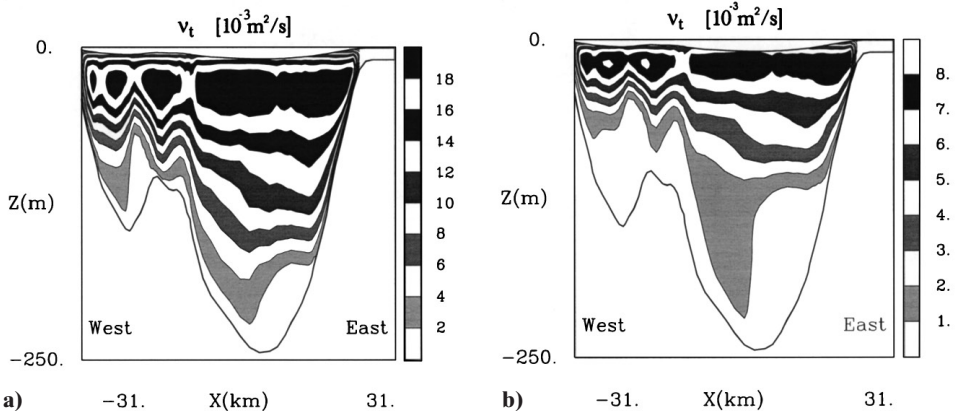


Figure 3. Vertical cut along the talweg of Lake Constance from west to east. Displayed are iso-line ranges of the vertical turbulent viscosity as computed with the k - ϵ model 48 hours after the onset of a spatially and temporally constant wind in the long direction of the lake. a) wind speed = 4.7 m s^{-1} , b) wind speed = 3 m s^{-1} . Note the different scales of the shading

In employing a prescribed vertical eddy viscosity, it might seem tempting to assume the value of the vertical eddy viscosity to be a function of the wind speed. Surely wind-driven layers with different depths can be achieved by such an approach, but instantaneous changes of the wind speed would result in instantaneous changes in the vertical eddy viscosity, obviously an odd feature of this approach. Consider for instance a certain depth within the Ekman layer when a stronger wind is applied, and let this depth be below the Ekman layer caused by a weaker wind. Then, after cessation of the stronger wind, a water particle at this depth will be subject to the pressure gradient and the Coriolis force, but no longer to surface stress (which is transported to larger depths only through the Ekman layer). This must yield abrupt changes in the direction of the velocity field at the time of wind cessation. It thus seems necessary to include some history dependence of the eddy viscosity to accommodate for a continuous transition of the flow from the strong to the weak wind scenario. Such hereditary effects can e.g. be accounted for by postulating a differential equation that describes the evolution of the eddy viscosity. This is exactly what is essentially done with the k - ε closure model.

Another interesting feature of the k - ε closure model is the fact that the maximum values of v_i do not arise at the surface but below it. In models where v_i -values are prescribed, this is accounted for by assuming v_i to grow linearly with depth down to 20% of the depth and then continuing it with a constant value below that depth, see Heaps (1984). All this is not very rational; instead, the depth profile is computed here.

Finally, we give a limited global overall account of how the flow develops in time during the initial 48 hours of the motion. The two graphs (Fig. 4) display the mean velocity \bar{v} calculated according to

$$\bar{v} = \frac{1}{V} \int_V \sqrt{\mathbf{v} \cdot \mathbf{v}} dV, \quad (10)$$

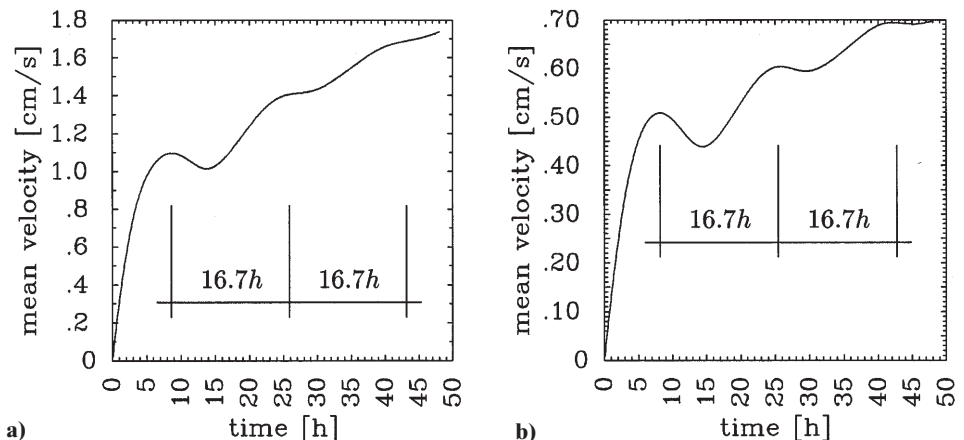


Figure 4. Mean velocity of the lake currents as a function of time plotted for the first 48 hours for the case of a) a strong wind speed = 4.7 m s⁻¹ and b) a weak wind speed = 3 m s⁻¹. The oscillations have a period of approximately 16.7 hours

where V is the lake volume. This variable is proportional to the square root of the total kinetic energy contained at any one time in the lake basin. Naturally, this content is larger for the stronger wind than for the weaker wind, and in neither of the two cases are steady state conditions reached after 48 hours. The transient growth of the current from the state of rest at the beginning to steady state conditions is, however, achieved with superimposed, but attenuated, oscillations which are more pronounced for the weaker wind than for the stronger wind, again a manifestation of the different values of the eddy viscosities. The periodicity of these oscillations, which can also be seen in the time series of the mid lake horizontal velocity components at virtually all depths in Fig. 5, can be read off from the graphs to be approximately 16.7 hours. This compares well with the theoretical period $2\pi/f = 16.3$ hours of the inertial period. The damping can also be estimated from the attenuation of consecutive amplitude peaks; it is about 70% for the strong wind and 62% for the weak wind, if the first two amplitudes are chosen for this estimate. Extrapolation to times when the amplitude of this oscillation is reduced to 1% of its initial value yields 2.6 (3.2) days for the strong (weak) wind, corresponding to roughly 3–4 (4–5) inertial periods. Calculation of the attenuation of the second and third amplitude peak leads to 60% (50%) for the strong (weak) wind, so, as the attenuation decreases in time, even greater differences can be expected.

It is thus a feature of the k - ϵ closure that the duration of inertial oscillations depends on the turbulent intensities that are created with the flow; they are thus sensitive to the applied wind forcing.

Results obtained with a vertical eddy viscosity constant in space but depending on the wind speed (neglecting history-dependent effects) discloses obvious drawbacks of its use. At sudden cessation of an applied wind the eddy viscosity would correspondingly also suddenly drop, implying an equally sudden reduction of dissipation. As a result, the oscillations in the current field that are present at the time of wind cessation would be less attenuated and the stored kinetic energy in the water

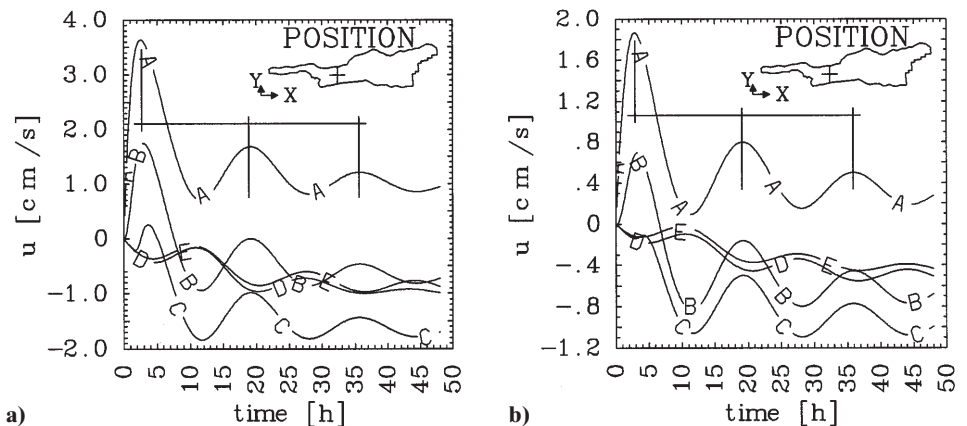


Figure 5. Time series of the along-talweg component of the velocity at different depths. The labels of the curves correspond to depths as follows, A = 2 m, B = 7 m, C = 16 m, D = 98 m and E = 148 m. a) wind speed = 4.7 m s^{-1} and b) wind speed = 3 m s^{-1}

mass would correspondingly persist for times longer than the true turbulence activity would allow.

Obviously, the history effects can rectify these odd features and must therefore be of considerable influence on the flow, sometimes changing its behaviour substantially; they should not be ignored.

5 Conclusions

Computations that determine the wind induced circulation in Lake Constance were performed by using the turbulent shallow-water equations paired with a first order k - ε closure scheme. Its use enabled us to adjust the vertical turbulent diffusivity to the turbulence intensity that is generated by the applied wind field. This was achieved by expressing the vertical viscosity ν_t in terms of the turbulent kinetic energy and its rate of dissipation, $\nu_t = c_\mu k^2/\varepsilon$, and by evaluating k and ε together with the motion through the application of transport equations for these quantities. It led to wind-driven surface layers in Lake Constance which adjust their depth to the turbulent intensity; qualitatively, wind-driven layer depths increase with wind speed, because the latter generates larger turbulent kinetic energies; however, because the latter continue to exist at least for some time after wind cessation, an automatic memory to turbulence is incorporated that avoids unnatural discontinuities in the turbulent viscosities.

Similarly, because of the larger eddy viscosities arising in the stronger wind case than in the weaker counterpart, inertial waves that accompany the transient flow features are more attenuated for stronger winds than for weaker ones. Using only zeroth-order closure models, these features cannot be described, or only in a rough fashion if ν_t is made directly dependent on the strength of the wind. However, such a parameterization has its drawbacks when the wind changes; it may lead to local discontinuities in the current and to odd physical behaviour, especially with regard to the depth of the wind-driven layer and the duration of inertial motions.

Higher-order turbulence closure is especially appropriate in numerical flows of time-dependent baroclinic processes that are generated by time-dependent external wind-forcing and solar irradiation. The reason is that, even more so than for barotropic processes, the baroclinic density structure and vertical gradients in the horizontal flow define its stability and affect the values of the turbulent viscosities ν_t . Parameterization of ν_t at the zeroth-order closure level is for this reason implemented by making ν_t Richardson-number-dependent. An automatic determination of ν_t via that of k and ε along with the motion is physically more appropriate, especially since the k - ε -model is physically well-founded.

ACKNOWLEDGEMENTS

This work was performed by using a program developed by Haidvogel et al. (see Haidvogel, D.B., Wilkin, J.L. and Young, R. (1991); Song Y. and Haidvogel D. (1994)) and extending it to include the k - ε closure. We thank Bob Svendsen, Ph.D. for checking our english.

REFERENCES

- Gütting, P.-M., 1998. Dreidimensionale Berechnung windgetriebener Strömungen mit einem k - ϵ -Modell in idealisierten Becken und dem Bodensee, Thesis at the Darmstadt University of Technology, to appear.
- Haidvogel, D.B., J.L. Wilkin and R. Young, 1991. A Semi-Spectral Primitive Equation Ocean Circulation Model Using Vertical Sigma and Orthogonal Curvilinear Horizontal Coordinates, *Journal of Computational Physics*, Vol. 94, Academic Press, New York and London: 151–185.
- Heaps, N.S., 1984. Vertical structure of current in homogeneous and stratified waters. In: K. Hutter (ed.), *CISM-Lectures*, Springer-Verlag, Vienna-New York: Hydrodynamics of Lakes, 153–207 pp.
- Hedström, K.S., 1994. Users Manual for a Semi-Spectral Primitive Equation Ocean Circulation Model, Institute for Naval Oceanography, Stennis Space Center, MS, 35 pp.
- Hollan, E. and T.J. Simons, 1978. Wind-induced changes of temperature and currents in Lake Constance, *Arch. Met. Geophys. Bioklim.*, Ser. A27:333–373.
- Hutter, K., 1991. Grossskalige Wasserbewegung in Seen: Grundlage der physikalischen Limnologie. In: K. Hutter (ed.), Springer-Verlag, Berlin Heidelberg New York: Dynamik umwelt-relevanter Systeme, 187–248 pp.
- Hutter, K., 1993. Waves and Oscillations in the ocean and in lakes. In: K. Hutter (ed.), *CISM courses and lectures No. 337*, Springer Verlag, Wien: Continuum mechanics in Environmental Sciences and Geophysics, 79–240 pp.
- Hutter, K., G. Bauer, Y. Wang and P.-M. Gütting, 1998. Forced motion response in enclosed lakes, IUTAM Symposium on Physical Limnology in Broome Aug. –Sept. 1995, Australia, to appear.
- Lehmann, A., 1992. Ein eindimensionales baroklines wirbelauflösendes Modell der Ostsee, Ber. Nr. 231 Institut f. Meereskunde, 104 pp.
- Press, W.H., S.A. Teukolsky, W.T. Vetterling, and B.P. Flannery, 1994. *Numerical Recipes in C*, Cambridge University Press, 842 pp.
- Rodi, W., 1993. Turbulence models and their applications in hydraulics; A state of the art review, IAHR/AIRH Monograph Series A.A. Balkema, Rotterdam, 10 pp, 27 pp.
- Song, Y. and D.B. Haidvogel, 1994. A Semi-implicit Ocean Circulation Model Using a Generalized Topography-Following Coordinate System, *Journal of Computational Physics*, Vol. 115, Academic Press, New York and London, 228–244 pp.
- Svensson, U., 1978. A Mathematical Model of the Seasonal Thermocline, University of Lund, Dept. of Water Resources Engg., Sweden, Rept. No. 1002, 147 pp.
- Wang, Y., 1996. Windgetriebene Strömungen in einem Rechteckbecken und im Bodensee, Shaker Verlag, Aachen, ISBN 3-8265-1381-9, 137 pp.

Received 3 December 1996;

revised manuscript accepted 20 January 1998.